Experimental Study of $^{9}_{\Lambda}$Be Hypernucleus

$^{9}_{\Lambda}$Be ハイパー核の実験的研究

Yukio Shimizu

清水 幸夫

学位論文

Experimental Study of ${}^{9}_{\Sigma}$Be Hypernucleus

${}^{9}_{\Sigma}$Be ハイパー核の実験的研究

平成８年２月博士（理学）申請

東京大学大学院理学系研究科
物理学専攻
清水 幸夫

Experimental Study of ${}^{9}_{\Sigma}$Be Hypernucleus

Yukio Shimizu

Department of Physics
School of Science
Graduate school
University of Tokyo
7-3-1, Hongo, Bunkyo-ku, Tokyo 113, Japan

February 15, 1996

Doctor Thesis

Abstract

This thesis gives a full description of a recent measurement of ^{9}Be(K^{-},$\pi^{\pm}$) spectra at P_K = 600 MeV/c. The experiment was done at the Low Energy Separated Beamline 2 (LESB2) of AGS accelerator at Brookhaven National Laboratory (BNL), using a magnetic spectrometer called MOBY DICK. The purpose of this experiment is to obtain high-statistics and unbiased data, and to prove (or disprove) the existence of narrow Σ hypernuclear states reported in 1980 by an experiment done at CERN. The nature of such narrow Σ hypernuclear states has remained one of the unsolved puzzles of nuclear physics for nearly 15 years, and high-quality data have been waited for.

In the present experiment, more than 5×10^{9} kaons were incident on the target for the (K^{-},π^{-}) reaction and 4×10^{9} kaons for the (K^{-},π^{+}) reaction. We used a good particle identification methods to suppress backgrounds and did not employ any out-of beam scintillator trigger which the previous CERN experiment did. As a result, we were able to accumulate more than 10 times higher statistics as compared with the previous CERN experiment.

Although the overall shape of the present ^{9}Be(K^{-},π^{-}) spectrum agrees fairly well with that of the CERN data, the two spectra disagree in the region of the 'double peak'. The present data do not exhibit the two narrow peaks; instead, there is a broad enhancement. Since the present data have much higher statistics, we conclude that there are no narrow Σ hypernuclear states of $^{9}_{\Sigma}$Be. No narrow structure was identified in the case of ^{9}Be(K^{-},π^{+}) either.

Attempts were made to reproduce the observed (K^{-},$\pi^{\pm}$) spectra based on a simple quasi-free picture, which takes account of neutron (proton) pickup from $p-$ and $s-$orbits, but the spectra could not be reproduced with such a model. Clearly, more theoretical studies are needed in order to fully understand the ^{9}Be(K^{-},$\pi^{\pm}$) spectra, and the present high-statistics data should provide a basis for such studies.

Contents

1 Introduction 1

1.1 Motivation of the experiment . . . 1

1.2 BNL-AGS E887 collaboration . . . 3

1.3 Outline of thesis . . . 4

2 Details of experiment 5

2.1 Kaon Beamline (LESB 2) and Kaon spectrometer . . . 6

2.2 Pion spectrometer(Moby Dick spectrometer) . . . 10

2.3 Detectors . . . 15

2.3.1 Drift Chambers . . . 15

2.3.2 Trigger counters . . . 15

2.3.3 Muon filter . . . 16

2.4 Targets . . . 18

2.5 Triggers . . . 19

2.6 Stability of the spectrometer magnets . . . 21

2.7 Other apparatus . . . 22

2.8 Data acquisition and on-line monitor . . . 22

3 Analysis 24

3.1 Overview of the analysis procedure . . . 24

3.1.1 Σ hypernuclear runs . . . 24

3.1.2 Calibration runs . . . 24

3.2 The first pass . . . 25

3.2.1 Trigger selection . . . 25

3.2.2 Hodoscopes analysis . . . 25

3.2.3 Hit position of the drift chamber . . . 25

3.2.4 Tracking of a particle . . . 27

3.2.5 The tracking throughout the spectrometer and momentum determination . . . 31

3.2.6 Event summary of the first pass . . . 33

3.3 The second pass . . . 33

3.3.1 Accurate pion momentum determination . . . 33

3.3.2 Target vertex cut . . . 36

3.3.3 Incoming K^- identification . . . 37

3.3.4 Outgoing π^- identification . . . 37

3.3.5 Possible background passing through the second pass . . . 44

3.3.6 Event summary of the second pass . . . 46
3.4 Overall Efficiencies . . . 46
3.4.1 Kaon beam related efficiency . . . 46
3.4.2 Computer data-taking efficiency . . . 53
3.4.3 Drift chamber and tracking efficiencies . . . 53
3.4.4 Kaon's and pion's decay correction . . . 55
3.4.5 Summary of efficiencies . . . 59

4 Results **60**
4.1 Definition of the excitation energy . . . 60
4.2 Cross section . . . 61
4.3 ^{9}Be(K^-,π^-) data in the Λ region . . . 61
4.3.1 Background rejection . . . 61
4.3.2 Systematic errors for the $^{9}_{\Lambda}$Be cross section . . . 64
4.3.3 Excitation energy spectrum . . . 64
4.4 ^{9}Be(K^-,π^+) data in the Σ region . . . 69
4.4.1 Excitation energy spectra . . . 69
4.4.2 Background rejection . . . 70
4.4.3 Systematic error for the cross section . . . 72
4.4.4 Cross sections as function of excitation energy . . . 73
4.5 ^{9}Be(K^-,π^-) data in the Σ region . . . 74
4.5.1 Excitation energy spectra . . . 74
4.5.2 Background rejection . . . 74
4.5.3 Systematic error of the cross section . . . 76
4.5.4 Cross section as function of excitation energy . . . 77

5 Discussion **81**
5.1 Comparison with the previous data at CERN . . . 81
5.2 ^{9}Be(K^-,π^+) data . . . 89
5.3 Comparison with a quasi-free picture . . . 91
5.3.1 (K^-,π^+) reaction on ^{9}Be . . . 91
5.3.2 (K^-,π^-) reaction on ^{9}Be . . . 95
5.3.3 Conclusion from quasi-free picture . . . 95

6 Summary **98**

Acknowledgements **99**

Appendices

A Transport Matrices **100**

B CH_2 data analysis and spectrometer energy resolution **103**

C Angular and momentum acceptance of the Pion spectrometer **105**
C.1 Angular acceptance . . . 105
C.2 Momentum acceptance . . . 105

D Momentum loss correction **108**

E Collaborators of BNL AGS E887 **114**

Bibliography **115**

List of Figures

1.1 Σ hypernucleus on ^{9}Be reported at CERN. The top figure shows the $^9_\Lambda$Be spectrum and the bottom figure shows the $^9_{\Sigma^0}$Be spectrum as functions of $\Delta B_{nHyperon}$, the excitation energy from production thresholds of hyperons. The lines are given to guide the eyes. Taken from Ref.[1] 2

2.1 Decay corrected kaon yields at the experimental target position, produced with 24 GeV/c protons in AGS. Calculation was made using a empirical formula of Sanford and Wang[21] with kinematic reflection[22]. 7

2.2 Fermi averaged $K^-+N \rightarrow \Sigma+\pi$ elementary cross sections. Taken from C. Dover et al.[23]. 8

2.3 Momentum transfer to hyperons in the ^{9}Be(K^-,π) reaction. $K\pi$ reaction angle is 4° for the setting of our experiment. 9

2.4 Schematic drawing of LESB2(Low Energy Separated Beamline 2). 11

2.5 Schematic figure of Moby Dick spectrometer. 12

2.6 Kaon beam profile at the target position 13

2.7 Kaon momentum bite in the Kaon spectrometer. Relative momentum (%) to the central (600 MeV/c) 14

2.8 CP threshold curve; Upper figure shows the kaon detection efficiency with the threshold value for the summed signal of CPA and CPB. Lower shows the pion detection efficiency. Our operating value is also indicated in the figure. 16

2.9 Decay in-flight of 586 MeV/c kaon. Accepted region for P_π=460 MeV/c is also indicated. Momenta of particles from 3-body decay are represented by the maximum momenta available. 18

2.10 Stopping probabilities of 460 MeV/c electron, muon and pion in iron (GEANT simulation) 19

2.11 Trigger logic diagram for experimental 887 20

3.1 TDC spectra of all hodoscope segments 26

3.2 Timing signal of drift chamber wires (DX1∼DX12). Chamber number 1∼12 corresponds to DX1∼DX12 ,respectively 27

3.3 Timing signal of drift chamber wires (DX13∼DX15). Chamber number 13 and 14 is D13X and D13Y, 15 and 16 is D14X and D14Y, 17 and 18 is D15X and D15Y. 28

3.4 Time sum of drift chamber layers (DX1∼DX12). Chamber number 1∼12 corresponds to DX1∼DX12 ,respectively 28

3.5 Time sum of drift chamber layers (DX13∼DX15). Chamber number 13 and 14 is D13X and D13Y, 15 and 16 is D14X and D14Y, 17 and 18 is D15X and D15Y. 29

3.6 Position deviations (measured − predicted) on 3rd chambers on each area. In the case of no hit on 3rd chamber, events were accumulated at +0.5 cm 32

3.7 dX/dZ, Y and dY/dZ deviations for the (K^-,π^-) run. Fitting was done with 2 gaussians. Cut applied: non beam track, redundancy cut and target vertex cut. 34

3.8 Reduced χ^2 for the (K^-,π^-) run. Cut applied: non beam track, redundancy cut and target vertex cut 36

3.9 Reduced χ^2 distribution of the (K^-,π^-) run after adjusting the pion momenta with RAYTRACE program 37

3.10 Selected region for good track events in χ^2 distributions of both (K^-,$\pi^\pm$) run 38

3.11 ^{9}Be target vertex image in the (K^-,π^-) reaction. Cut applied:K beam TOF (described in the next section), χ^2 and the other 2 vertices cut. 39

3.12 ^{9}Be target vertex image in the (K^-,π^-) reaction. Cut applied:K beam TOF, χ^2, other 2 vertices cut and muon electron cut (cut conditions of K beam TOF and μ/e selection will be described in next section). 40

3.13 ^{9}Be target vertex image in the (K^-,π^+) reaction. Cut applied:K beam TOF (described in the next section), χ^2 and other 2 vertices cut. 41

3.14 Z vertex distribution of the (K^-,π^-) reaction in Figure 3.12 was fitted with 2 gaussians and linear background. Function used to fit is P1×exp(−0.5($\frac{Z-P2}{P3}$)^2) + P4×exp(−0.5($\frac{Z-P5}{P6}$)^2) + P7 + P8×Z. 42

3.15 Z vertex distribution of the (K^-,π^+) reaction in Figure 3.13 was fitted with 2 gaussians and linear background. Function used to fit is P1×exp(−0.5($\frac{Z-P2}{P3}$)^2) + P4×exp(−0.5($\frac{Z-P5}{P6}$)^2) + P7 + P8×Z. 43

3.16 TOF spectrum between S1 and ST of KB trigger without any event selection 43

3.17 Simulated momentum distribution of the decay products from 586 MeV/c K^-, which enter the effective area of the drift chamber DX12. Upper figure shows the momentum distribution of negative charge particles(e^-, μ^- and π^-) which cause background in the (K^-,π^-) reaction and lower figure represents that of positive charge particle(π^+) which cause background in the (K^-,π^+) reaction. Generated numbers of kaon is 10^8. The decay vertexes are required to be inside the target region. 45

3.18 Pathlength-corrected time of flight from ST to SR with the target vertex and χ^2 selection 46

3.19 TDC distribution of the MU counter [^{9}Be(K^-,π^-) run]. Selected region as muon is indicated in the bottom figure 47

3.20 Pathlength corrected time of flight from ST to SR with the target vertex and χ^2 selection, and muon elimination. Solid line: 2-Gaussian fit (P1×exp(−0.5($\frac{X-P2}{P3}$)^2) + P4×exp(−0.5($\frac{X-P5}{P6}$)^2)) of electrons and pions. 48

3.21 Target Z vertex in the (K^-,π^-) reaction. Empty target data (dashed) is overlayed on the ^{9}Be data (solid). Upper figure is the same one in Figure 3.11, and lower is in Figure 3.12. In both figures, empty data are selected with the completely same criteria as ^{9}Be data. Empty target data are multiplied by 10.1 times so as to compare with ^{9}Be data with the same number of incident kaons. 49

3.22 Target Z vertex in the (K^-,π^+) reaction. Empty target data (dashed) is overlayed on the ^{9}Be data (solid). Figure is the same one in Figure 3.13. In this figure, empty data are selected with the completely same criteria as ^{9}Be data. Empty target data are multiplied by 10.8 times so as to compare with ^{9}Be data with the same number of incident kaons. . . 50

3.23 Monte carlo simulation of momentum distribution of π^-'s from K^0 decay at the DX12 position. K^0 is produced via the p(K^-,K^0)n reaction. Arrows indicate the momentum region acceptable to our experimental setting of P_π = 460 MeV/c and 438 MeV/c. 51
3.24 Kaon horizontal profiles in KPI events on both ^{9}Be and CH_2 target. Event selection is the same as the final results. 54
3.25 χ^2 distribution of degree of freedom = 3 (solid line) with our experimental reduced χ^2 data (histogram) 55
3.26 Survival probability of incoming kaons between ST and the target estimated using the experimental data. 56
3.27 Survival probabilities of emitted pions estimated using the experimental data for each run conditions. 57

4.1 Excitation energy vs $K\pi$ scattering angle of the ^{9}Be(K^-,π^-) reaction in the Λ region. . . 62
4.2 Missing π^0 mass spectrum assuming $K^-\rightarrow\pi^-\pi^0$ decay kinematics 63
4.3 Spectrum of of ^{9}Be(K^-,π^-)$^9_\Lambda$Be reaction as a function of excitation energy(EE). The vertical axis is number of counts per 2 MeV. EE = 0 MeV is Λ production threshold. EE > 0 MeV represents the Λ unbound region. 65
4.4 Acceptance-corrected spectrum of of ^{9}Be(K^-,π^-)$^9_\Lambda$Be reaction as a function of excitation energy(EE). The vertical axis is number of counts per 2 MeV. Acceptance curve used is indicated in solid line. EE = 0 MeV is Λ production threshold. EE > 0 MeV represents the Λ unbound region. 66
4.5 Cross section plot of ^{9}Be(K^-,π^-)$^9_\Lambda$Be reaction as a function of excitation energy(EE). Correction of the spectrometer momentum acceptance was applied. EE = 0 MeV is Λ production threshold. EE > 0 MeV represents the Λ unbound region. 67
4.6 $^9_\Lambda$Be data obtained at CERN[1]. Horizontal axis is the excitation energy with the same scale as our data. Vertical axis is number of counts per 2 MeV. These data were taken at P_K = 720 MeV/c and Pion detection angle at 0 degree. 68
4.7 Excitation energy (EE) spectra of the ^{9}Be(K^-,π^+) reactions at P_π = 438 MeV/c (upper spectrum) and P_π = 460 MeV/c (lower spectrum). The vertical axis is number of counts per 2 MeV. EE = 0 MeV is the Σ^- production threshold. EE > 0 MeV is the Σ^- unbound region. 70
4.8 Acceptance-corrected spectra of the ^{9}Be(K^-,π^+) reaction as function of excitation energy(EE) at P_π = 438 MeV/c (upper spectrum) and P_π = 460 MeV/c (lower spectrum). The vertical axis is number of counts per 2 MeV. Acceptance curve used is indicated in solid line. EE = 0 MeV is the Σ^- production threshold. EE > 0 MeV is the Σ^- unbound region. 71
4.9 ^{9}Be(K^-,π^+) excitation energy (EE) spectrum (solid) overlayed on the empty target spectrum (dotted). EE = 0 MeV is the Σ^- production threshold. P_π = 438 MeV/c 72
4.10 Cross section of the ^{9}Be(K^-,π^+) reaction as a function of excitation energy(EE). Upper data was taken at P_π = 438 MeV/c and lower data at P_π = 460 MeV/c. EE = 0 MeV is the Σ^- production threshold. EE > 0 MeV is the Σ^- unbound region. 73
4.11 Excitation energy (EE) spectrum of the ^{9}Be(K^-,π^-) reaction in the Σ region. The vertical axis is number of counts per 2 MeV. EE = 0 MeV is the Σ^0 production threshold 74

4.12 Acceptance-corrected spectrum of the ^{9}Be(K^-,π^-) reaction as function of excitation energies(EE). The vertical axis is number of counts per 2 MeV. Acceptance curve used is indicated in solid line. EE = 0 MeV is the Σ^0 production threshold 75
4.13 ^{9}Be(K^-,π^-) excitation energy (EE) spectrum (solid) overlayed on the empty target spectrum (dotted). EE = 0 MeV is the Σ^0 production threshold 76
4.14 Cross section of the ^{9}Be(K^-,π^-) reaction as a function of excitation energy(EE). Data was taken at P_π = 460 MeV/c. EE = 0 MeV is the Σ^0 production threshold. EE >0 MeV is the Σ^0 unbound region. Production threshold of Σ^+ is at EE = 13.3 MeV. 77
4.15 ^{9}Be(K^-,π^-) excitation energy (EE) spectrum in the Σ region. Λ continuum tail is assumed to be described as a Gaussian tail. EE = $-$35 MeV to $-$9 MeV data was used for fitting. The solid line is the extrapolated line of Λ continuum in the Σ region 78
4.16 ^{9}Be(K^-,π^-) excitation energy (EE) spectrum derived by subtracting the Λ continuum. Λ tail was assumed to be a tail of Gaussian (see Figure 4.15). Vertical and horizontal axis definitions are the same as before. 79
4.17 ^{9}Be(K^-,π^-) excitation energy (EE) spectrum in the Σ region. Λ continuum tail is assumed to be described as a linear function. EE = $-$30 MeV to $-$5 MeV data was used for fitting (solid line). The dashed line is the extrapolated line of Λ continuum in the Σ region . . . 80

5.1 $K\pi$ scattering angle distribution of ^{9}Be(K^-,π^-) reaction in the Σ region. Event selections applied are the same as those to derive the spectrum in Figure 4.11. 82
5.2 Momentum transfer vs. excitation energy of the ^{9}Be(K^-,π^-) reaction (Experimental data). EE = 0 MeV is the Σ^0 production threshold. Spectrometer momentum acceptance is not corrected for. 83
5.3 Simulated momentum transfer vs. excitation energy of the ^{9}Be(K^-,π^-) reaction for our experiment. EE = 0 MeV is the Σ^0 production threshold. Gaussian distributions for incident K^- momentum (mean = 586 MeV/c, σ = 3%) and $K\pi$ scattering angle (mean = 6.5°, σ = 2.6°) were used. Momentum acceptance of Pion spectrometer was not assumed 84
5.4 Simulated momentum transfer vs. excitation energy of the ^{9}Be(K^-,π^-) reaction for CERN experiment. EE = 0 MeV is the Σ^0 production threshold. Gaussian distributions for incident K^- momentum (mean = 720 MeV/c, σ = 3%) and $K\pi$ scattering angle (mean = 3.0°, σ = 1.5°) were used. Momentum acceptance of Pion spectrometer was not assumed 85
5.5 Momentum transfer vs. excitation energy plot. Simulated results for our experiment (contour plot) is superimposed on the experimental data (dot). EE = 0 MeV is the Σ^0 production threshold. 86
5.6 Comparison of the simulated momentum transfer vs. excitation energy between ours and CERN's. EE = 0 MeV is the Σ^0 production threshold. Boxed plot is for our experiment and dotted plot for CERN. 87
5.7 Comparison of our (K^-,π^-) data (closed circle) with the CERN data (histogram). Vertical axis is arbitrarily normalized. Horizontal axis is the excitation energy. EE = 0 MeV is the Σ^0 production threshold. 88
5.8 2 Gaussians and linear background fit of CERN narrow peaks in the region of EE = 0 MeV to 10 MeV. 89
5.9 Convoluted CERN two peaks with our energy resolution (4.2 MeV) [dotted line] superimposed on our ^{9}Be(K^-,π^-) data. Our data has no indication of narrow peaks. 90

5.10 Quasi-free calculation (solid line) described in the text, on (i) ^{6}Li(K^-,π^+) and (ii) ^{16}O(K^-,π^+) data obtained at BNL(Ref.[11]). Experimental energy resolution is not included. EE = 0 MeV represents Σ^- production thresholds. Vertical scale is arbitrarily normalized 92
5.11 Quasi-free calculation (solid line) described in the text, on (i) ^{12}C(K^-,π^+) and (ii) ^{16}O(K^-,π^+) data obtained at CERN(Refs.[9] and [10]). Experimental energy resolution is not included. EE = 0 MeV represents Σ^- production thresholds. Vertical scale is arbitrarily normalized 92
5.12 Calculated excitation energy spectrum (solid line) of the ^{9}Be(K^-,π^+) reaction with quasi-free assumption (on details, see text) superimposed on our data. $b = 1/105$ (MeV/c)$^{-1}$ and the spectroscopic factor ratio of s- to p-state proton is taken to be 1:2. Vertical normalization is arbitrary. 93
5.13 Calculated excitation energy spectrum (solid line) of the ^{9}Be(K^-,π^+) reaction with quasi-free assumption (on details, see text) superimposed on our data. $b = 1/120$ (MeV/c)$^{-1}$ and the spectroscopic factor ratio of s- to p-state proton is taken to be 1:2. Vertical normalization is arbitrary. 94
5.14 Calculated excitation energy spectrum (solid line) of the ^{9}Be(K^-,π^-) reaction with quasi-free assumption (on details, see text) superimposed on our data. $b = 1/105$ (MeV/c)$^{-1}$ and the spectroscopic factor ratio s:p(18 MeV excitation):p(loosely bound)=1:2:1. Vertical normalization is arbitrary. 96

B.1 Energy resolution of the whole spectrometer system derived by monochromatic peak from the p(K^-,π^+)Σ^- reaction. EE = 0 MeV corresponds to the Σ^- production. Target is CH_2 104

C.1 Angular distributions of emitted particles accepted by the Pion spectrometer. θ = dX/dZ (mrad). ϕ = dY/dZ (mrad) 106
C.2 Momentum acceptance($\delta P/P(\%)$) of the Pion spectrometer. Determined by the accepted K_{e3} decay events (histogram). Solid line is the parameterized acceptance by the normal frequency functions. 107

D.1 Momentum loss distributions of pions(left) and kaons(right) in the target area for Empty target run. P_{kaon}(MeV/c) is momentum determined at the Kaon spectrometer. P_{pion}(MeV/c) is at the Pion spectrometer. Result of 2 Gaussians fit is shown in solid line 111
D.2 Momentum loss distributions of pions(left) and kaons(right) in the target area with ^{9}Be target. P_{kaon}(MeV/c) is momentum determined at the Kaon spectrometer. P_{pion}(MeV/c) is at the Pion spectrometer. Result of 2 Gaussians fit is shown in solid line 112
D.3 Momentum loss distributions of pions(left) and kaons(right) in the target area with CH_2 target. P_{kaon}(MeV/c) is momentum determined at the Kaon spectrometer. P_{pion}(MeV/c) is at the Pion spectrometer. Result of 2 Gaussians fit is shown in solid line 113

List of Tables

2.1 E887 experimental conditions 5
2.2 Pion momenta at hyperon production threshold. P_K=586MeV/c. Pion detection angle is 4^o. 6
2.3 Characteristics of LESB2 beam line 7
2.4 Performances of the Pion spectrometer 11
2.5 Drift chamber configurations 15
2.6 Trigger counter specifications and the typical counting rates in this experiment 17
2.7 Time difference of K, π, μ and e for S1−ST and ST−S2 21
2.8 Prescale factors and numbers of triggers (K^-,π^-) run 21
2.9 Prescale factors and numbers of triggers (K^-,π^+) run 22
2.10 Typical data-taking rate of the (K^-,π^-) run. Number of events accepted in RUN 41 is tabulated 23
2.11 Typical data-taking rate of the (K^-,π^+) run. Number of events accepted in RUN 58 is tabulated 23

3.1 Drift chamber efficiencies in KPI trigger (RUN42) gated by "non beam track" condition . 29
3.2 Drift chamber configuration and positions relative to the focus point of the spectrometer. 30
3.3 Event summary of the first pass for each run condition as for KB and KPI trigger. This presents how many events were survived through each event selection. 35
3.4 Event summary of the second pass for each run condition as for KPI trigger. Number of events indicates how many events were survived through the event selection. 52
3.5 The run by run basis event efficiencies. Actual numbers of kaons in the kaon scaler counts (Section 3.4.1.2), the live time of KPI events (Section 3.4.2) and the tracking efficiency (Section 3.4.3.1) are presented. 58

A.1 2nd order transport matrices for kaon and pion spectrometer. X', Y', θ' and ϕ' are measured values at front focus. X, Y, θ and ϕ are at rear focus. L is path length. X, Y, Z, L are measured in cm, θ=dX/dZ and ϕ=dY/dZ in mrad and δP/P in % 101
A.2 2nd order transport matrices for kaon and pion spectrometer. (continues) 102

D.1 Momentum losses of kaons and pions in the ^{9}Be and CH_2 target derived by subtracting the empty target data. 108

Chapter 1

Introduction

This thesis presents a full account of the experimental study of the ${}^{9}_{\Sigma}$Be hypernucleus, produced by the ^{9}Be(K^-,$\pi^{\pm}$) reaction at P_K = 600 MeV/c. The experiment was performed at Brookhaven National Laboratory as experiment 887 (E887).

1.1 Motivation of the experiment

The purpose of E887 is to obtain high statistics ^{9}Be(K^-,$\pi^{\pm}$) data, and to prove (or disprove) the existence of narrow Σ hypernuclear states reported in 1980 by an experiment done at CERN (Bertini et al.[1]). The nature of such narrow Σ hypernuclear states has remained one of the unsolved puzzles of nuclear physics for nearly 15 years, and high-quality data have long been waited for.

The reaction used in the CERN experiment was ^{9}Be(K^-,π^-) at P_K = 720 MeV/c, the pion detection angle was 0°, and their spectra are shown in Figure 1.1. The top half of the figure shows the region of ${}^{9}_{\Lambda}$Be hypernucleus. By the time this experiment was done, Λ hypernuclear production by the "recoilless" in-flight reaction (described in detail in the next chapter) had been well established. The recoilless reaction is known to strongly populate the 'substitutional' states, in which a p-shell neutron is 'substituted' by a Λ occupying the p-shell orbit without angular momentum transfer, and the dominant peaks in the ${}^{9}_{\Lambda}$Be region are due mostly to the population of such states*.

What was surprising was the discovery of two narrow ($\Gamma < 8$ MeV) peaks about 80 MeV above the Λ hypernuclear region (see bottom half of Figure 1.1). Since 80 MeV is roughly equal to the $\Sigma - \Lambda$ mass difference, it was natural to attribute those peaks to the formation of Σ hypernuclear states †.

This discovery was totally unexpected. Since a Σ in a nucleus can convert via the strong interaction to a Λ ($\Sigma N \rightarrow \Lambda N$), the existence of narrow (long-lived) Σ hypernuclear states had been considered impossible. For example, based on the analysis of the energy shifts and widths of sigmonic X-rays, Batty[2] and Gal[3] estimated the widths of Σ hypernuclear states to be $20 \sim 30$ MeV.

As shown in Figure 1.1, the similarity of the two spectra are rather striking, and the curves drawn to 'guide the eyes' make the similarity even more impressive. Based on this observation, it was generally

*Note, however, that the shell-model picture does not adequately describe the ${}^{9}_{\Lambda}$Be structure. Detailed discussion will be given in Chapter 5.

†Although the ^{9}Be(K^-,π^-) reaction can produce two different types of Σ hypernuclei, ${}^{9}_{\Sigma^0}$Be and ${}^{9}_{\Sigma^+}$Be, Bertini et al. assigned the peaks to the formation of ${}^{9}_{\Sigma^0}$Be. This is because the elementary Σ^+ production cross section at P_K = 720 MeV/c is known to be negligibly small. Hence, the abscissa of the bottom half of Figure 1.1 is the excitation energy measured from the Σ^0 production threshold.

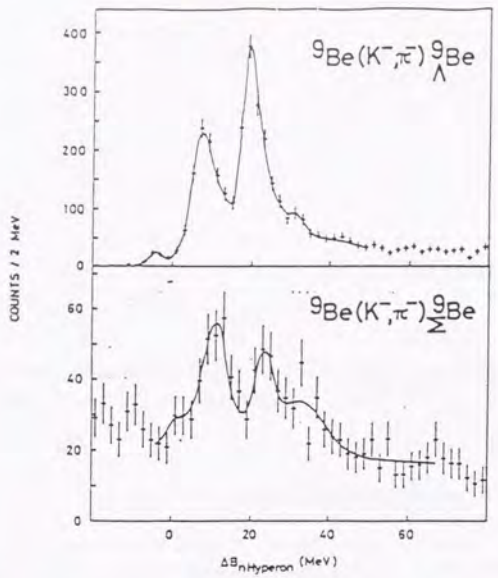

Figure 1.1: Σ hypernucleus on ^{9}Be reported at CERN. The top figure shows the $^{9}_{\Lambda}$Be spectrum and the bottom figure shows the $^{9}_{\Sigma^0}$Be spectrum as functions of $\Delta B_{nHyperon}$, the excitation energy from production thresholds of hyperons. The lines are given to guide the eyes. Taken from Ref.[1]

believed that the depth of the $\Sigma-$nuclear central potential should be similar to that of the $\Lambda-$nuclear potential ($\sim$ 30 MeV).

The CERN discovery prompted intensive theoretical and experimental studies of Σ hypernuclei. Theoretically, possible mechanisms to quench the ΣN conversion widths were proposed to explain the existence of narrow Σ hypernuclear states[23]. Predictions for the spin-orbit splitting of Σ in nuclei were also given. Though there were much effort to describe the $^{9}_{\Sigma}$Be hypernuclear spectrum from the viewpoints of the nuclear shell model or α cluster model[4][5][6][7][8], none of them succeeded to reproduce it.

On the experimental side, the CERN group constructed a new low-momentum kaon beam line dedicated for the Σ hypernuclear spectroscopy, and they reported narrow $p-$shell substitutional states of $^{12}_{\Sigma^-}$Be and $^{16}_{\Sigma^-}$C, populated respectively by the ^{12}C(K^-,π^+) and ^{16}O(K^-,π^+) reactions. These data were used to deduce the Σ spin-orbit splitting, and the claim was that it was twice stronger than that of nucleon in nuclei[9][10].

Subsequently, narrow $p-$shell substitutional Σ hypernuclear states were reported in experiments at BNL[11] and at KEK[12]. However, all the candidate peaks have low statistics, and some of the results are mutually inconsistent. In addition, all peaks are in the Σ quasi-free region, and no ground (or bound) state peak was reported. This last fact contradicts the assumptions that i) Σ potential is as deep as the Λ potential, and ii) the Σ conversion width is somehow suppressed; if both of these assumptions were

true, we would have observed a distinct peak of Σ hypernuclear bound state(s).

To ensure the existence of Σ hypernuclei, high statistics data were taken at BNL[13] on ^{7}Li(K^-,π^+), ^{12}C(K^-,π^+) and at KEK[14] on ^{12}C(stopped K^-,π^+). Both of these experiments gave negative results on the existence of narrow Σ hypernuclear states. In particular, the analysis of the spectral shape of the ^{12}C(stopped K^-,π^+) quasi-free continuum, with a the results of DWIA calculations performed within the framework of Green's function method developed by Morimatsu and Yazaki [15], revealed that the Σ-nucleus potential depth should be shallower than several MeV. With these negative results, interests in Σ hypernuclei gradually diminished.

A new insight in the Σ hypernuclear physics was obtained, however, when a candidate for the ground state of $^{4}_{\Sigma}$He hypernucleus was reported in the ^{4}He(stopped K^-,π^-) reaction performed at KEK[18]. In the ^{4}He(stopped K^-,π^+) spectrum, there was no structure. The difference between the two spectra is a clear indication of the importance of isospin dependence of the $\Sigma-$nucleus potential (Lane term). In fact, prior to the experimental discovery, Harada et al.[17] had already predicted that there should exist a relatively narrow $T = 1/2$ bound state of $^{4}_{\Sigma}$He, while the $T = 3/2$ partner should be unbound. The experimental results were consistent with such predictions.

Although there still remain some uncertainties in determining the exact binding energy and width of the $^{4}_{\Sigma}$He state[‡], the $^{4}_{\Sigma}$He and the $^{9}_{\Sigma}$Be reported at CERN are the only two Σ hypernuclear candidates which are considered 'solid'. A question remains, however, why narrow Σ states are observed only for ^{9}Be, when all other $p-$shell nuclei do not seem to produce Σ hypernuclei.

Experimentally, it is imperative to accumulate high-statistics data of $^{9}_{\Sigma}$Be, and provide independent test of the claim made by the CERN experiment. Surprisingly, no such data have been taken so far, due mostly to the difficulty in obtaining a high-flux kaon beam. In 1992, a new booster synchrotron for AGS was completed at BNL, which boosted up the primary proton beam intensity of AGS by nearly an order of magnitude. We took advantage of this opportunity and collected high statistics data of ^{9}Be(K^-,$\pi^\pm$) in the summer of 1994.

1.2 BNL-AGS E887 collaboration

E887 is a collaboration of Brookhaven National Laboratory (BNL), University of Tokyo, Institute of Nuclear Study (INS), Ohio University, Houston University and Hampton University. Members of collaborators are listed in Appendix E.

E887 was designed to verify the existence of the narrow Σ hypernuclear structures on various nucleus with high-statistics and unbiased data. Approved beam time was 800 hours (100 hours for setup and 700 hours for experiment). We have run for 2.5 months from the beginning of May to the middle of July in 1994 and collected Σ hypernuclear data on ^{9}Be and ^{6}Li with (K^-,$\pi^\pm$) reactions.

The main features of E887 are not only to obtain a high-statistics data (10 times more than the previous CERN experiment) but also unbiased data. The previous data taken at CERN[1][9][10] tagged the Σ hypernuclear events with scintillation counters surrounding the target to reduce the background from in-flight K^- decay (out-of beam scintillator trigger) and were not pion inclusive data. Thus we intended to get pure pion inclusive spectra from (K^-,π) reactions without tagging. We renewed the particle-identification system for this experiment and succeed to reduce in-flight K^- decay background

[‡]The peak position is close to the binding threshold and it is on the shoulder of the quasi-free continuum. Thus it is inappropriate to simply fit a Breit-Wigner curve to the peak to deduce the binding energy and width. For details, see Ref.[16].

completely.

The author will present the experimental results of ^{9}Be(K^-,$\pi^\pm$) data and ^{6}Li data is presented in Ref.[20].

1.3 Outline of thesis

This thesis is organized as follows. Chapter 2 describes details on experimental conditions and setups. Data analysis procedures are presented in Chapter 3, which is followed by the presentation of the final spectra in Chapter 4. Discussion of the results, including the comparison of our data with those of the CERN experiments, is in Chapter 5. Chapter 6 gives thesis summary.

Chapter 2

Details of experiment

In this chapter, we describe details of the experiment. Our experiment (BNL AGS E887) was carried out at Low Energy Separated Beamline 2 (LESB2) on the C line of the Alternating Gradient Synchrotron (AGS), located at Brookhaven National Laboratory (BNL).

The reactions used to study Σ hypernuclei are strangeness-exchange (K^-,$\pi^\pm$) reactions on a ^{9}Be target. Data were taken using two magnetic spectrometers (Kaon spectrometer and Pion spectrometer); incoming kaon were identified and momentum-analyzed with the Kaon spectrometer and outgoing pions were identified and momentum-analyzed with the Pion spectrometer.

Target	^{9}Be
K^- momentum	600MeV/c
π momentum	460MeV/c for ^{9}Be(K^-,π^-) in the Σ region 438MeV/c and 460 MeV/c for ^{9}Be(K^-,π^+) 550MeV/c for ^{9}Be(K^-,π^-) in the Λ region
π detection angle	4 degrees

Table 2.1: E887 experimental conditions

The run conditions as summarized in Table 2.1 were chosen based on the following considerations;

1. Reaction angle (π detection angle)
   At 0 degrees (forward angle) the elementary cross section N(K^-,π)Σ is largest, and the momentum transfer to sigma particles is smallest. Since these are the best situation for our purpose to produce ^{9}Be Σ hypernucleus, measurements at small angle are favored.

   However, in-flight kaon decays cause large background at forward angles. We can suppress the kaon decay background by reconstructing reaction vertex and by requiring that vertex position is in the target volume. The reaction angle of 4 degrees was chosen as an optimum to achieve good vertex resolution while maintaining large yield.

2. Kaon momentum
   For the N(K^-,π)Σ reaction, there exists a so called "magic momentum", where the momentum transfer to the Σ's becomes to zero in the case of 0^o $K\pi$ reaction angle, hence the probability for forming (substitutional) Σ hypernuclei is maximum (recoilless reaction). Also at non-zero reaction

Reactions to produce hyperons	Hyperon production threshold pion momentum(MeV/c) at 4°
^{9}Be(K^-,π^-)^{8}Be+Λ	572
^{9}Be(K^-,π^-)^{8}Be+Σ^0	492
^{9}Be(K^-,π^-)^{8}Li+Σ^+	477
^{9}Be(K^-,π^+)^{8}Li+Σ^-	469

Table 2.2: Pion momenta at hyperon production threshold. P_K=586MeV/c. Pion detection angle is 4°.

angle, the momentum transfer is minimized (not zero) at a certain K^- momentum. This occurs for ^{9}Be at 4 degrees at $\sim$ 250 MeV/c as shown in Figure 2.3. As shown in Figure 2.1, however, kaon beam flux at this low momentum is small. In order to collect high statistics while minimizing the momentum transfer, we chose 600 MeV/c as the kaon momentum (on the target, the kaon momentum was 586 MeV/c due to the kaon momentum loss in several materials on the beamline. See Appendix D). Recall that the CERN beryllium experiment was done at 720 MeV/c, and that all subsequent Σ hypernuclei experiment at BNL were done above 700 MeV/c. Thus, the kaon momentum of the present experiment is lower (hence closer to the magic momentum). Nevertheless, we could collect nearly 10 times higher statistics, thanks to a good particle identification methods we employ without using an out-of-beam scintillator tagging which the CERN experiment did.

Also note that at 600 MeV/c the elementary cross section of n(K^-,π^-)Σ^0 is larger than p(K^-,π^-)Σ^+ (see Figure 2.2) so that the product of ^{9}Be(K^-,π^-) would be dominantly Σ^0.

3. Pion momentum
The threshold momenta of sigma particle productions for ^{9}Be(K^-,π^-)Σ^0 +^{8}Be, Σ^++^{8}Li, Λ+^{8}Be and ^{9}Be(K^-,π^+)Σ^-+^{8}Li reactions are tabulated in Table 2.2. Previously-reported two ^{9}Be Σ hypernuclear states are about 10 MeV and 20 MeV above the threshold of Σ^0 production on top of the Σ continuum. In order to cover the both structures, we set the central momentum of the Pion spectrometer at 460 MeV/c which corresponds to 15 MeV above the Σ^0 threshold for (K^-,π^-) reaction. As for the (K^-,π^+) reaction, we ran at two central momentum settings of the Pion spectrometer. One was 438 MeV/c which corresponds to 15 MeV above the Σ^- production threshold. The π^+ spectrum obtained with this setting can be directly compared with the (K^-,π^-) spectrum without the momentum acceptance correction of the spectrometer. The other was the same central momentum as (K^-,π^-) reaction (460MeV/c), which was used to check the relative consistency of the momentum acceptance shape.

2.1 Kaon Beamline (LESB 2) and Kaon spectrometer

A characteristics of LESB2 is tabulated in Table 2.3 and a schematic drawing of the LESB 2 beamline is shown in Figure 2.4.

Particles produced by the 24 GeV/c protons on the 6.7 cm thick platinum target were bent by a septum magnet D1 and focused by the quadrupoles Q1 and Q2, and were steered to go through the center of the double-stage electro-static separators BS1 and BS2. BS1 has a 5 inch gap and was operated with ± 300 kV. BS2 has a 4 inch gap and was operated with ± 250 kV.

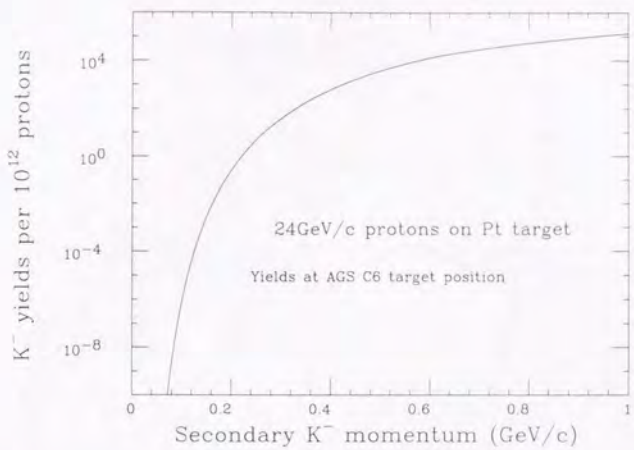

Figure 2.1: Decay corrected kaon yields at the experimental target position, produced with 24 GeV/c protons in AGS. Calculation was made using a empirical formula of Sanford and Wang[21] with kinematic reflection[22].

Maximum momentum	750 MeV/c
Length	15 m
$\delta p \delta \Omega$	50 msr%
Beam optics	Corrected to second order
Electro-static separators	Double-stage 5 inch gap, 300kV, 2 m (upstream) 4 inch gap, 250kV, 2 m (downstream)
Production target	6.7 cm platinum, air cooled
Production angle	5°
Kaon yields at 600 MeV/c	10×10^3 per 1×10^{12} protons
π/K ratio at 600 MeV/c	15:1
Kaon momentum bite	± 3 %
Kaon profile	10 cm in X and 2 cm in Y (FWHM)

Table 2.3: Characteristics of LESB2 beam line

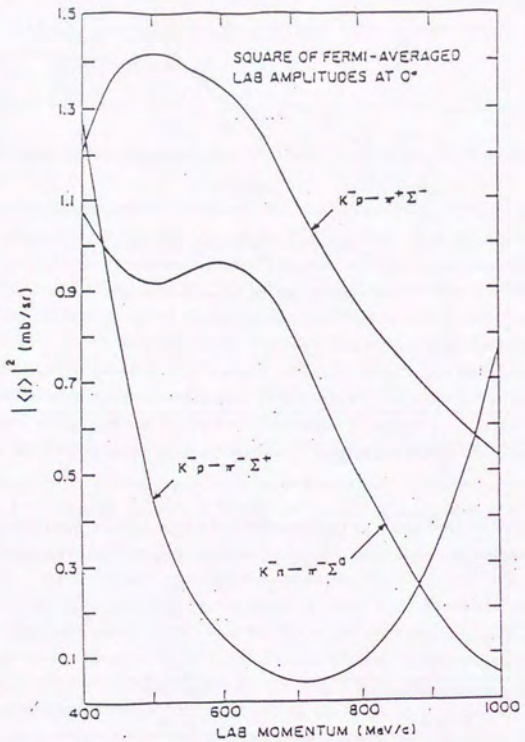

Figure 2.2: Fermi averaged $K^-+N \to \Sigma+\pi$ elementary cross sections. Taken from C. Dover et al.[23].

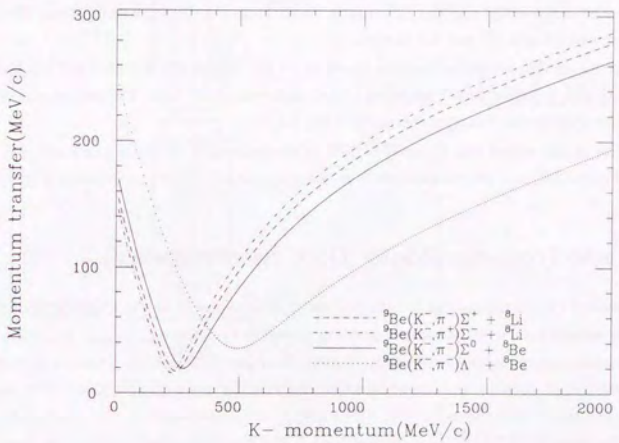

Figure 2.3: Momentum transfer to hyperons in the ^{9}Be(K^-,π) reaction. $K\pi$ reaction angle is 4° for the setting of our experiment.

With Q3 and Q4, particles were focused on the mass slit, where kaons were selected from contaminant pions by a spatial separation. The well-separated kaon beam entered the Kaon spectrometer.

The Kaon spectrometer had 2 sets of vertically and horizontally focusing quadrupoles and a momentum selecting dipole magnet. Configuration was Q6, D2, Q7, Q8 from upstream (see Figure 2.5). Kaons were focused on a target placed downstream of Q8; the total length of LESB2 and the kaon spectrometer (from the platinum production target to the experimental target area) was approximately 15 m. A hodoscope consisting of 8 small scintillation counters and a drift chamber (DX1), located between Q5 and Q6, and 6 drift chambers (DX2, DU3, DX4, DV5, DX6, DU7) placed between Q8 and the target, were used to reconstruct kaon momenta(Z direction is defined along the beam axis, and Y is the vertical(up) and X is the horizontal axis in right-handed coordinate. U axis is $+45^\circ$ and V axis is -45° rotated from the Y direction, respectively).

Kaons were identified by combining the information from a lucite Čerenkov counter (CP), located just upstream of the target, and time of flight measured between 2 scintillation counters S1 and ST. The S1 counter was at the entrance of Q6 and the ST counter was attached to the upstream of the CP counter; the flight path between S1 and ST was 4.3 meters.

With a typical proton flux on the production target of 5×10^{12}/pulse, the 600 MeV/c kaon flux at the experimental target was typically 5×10^{4}/pulse and π/K ratio was about 15:1. The accelerator cycle was 3.8 sec and effective spill length was approximately 2 sec.

The kaon profile on the target was 10 cm (FWHM) in the horizontal direction and 2 cm (FWHM) in the vertical (see Figure 2.6) and the momentum bite of kaons was $\pm$ 3 % (σ) as shown in Figure 2.7.

2.2 Pion spectrometer(Moby Dick spectrometer)

The Pion spectrometer (we sometime call it "Moby Dick" spectrometer) had the QQDQQ configuration and was rotatable around a pivot at the target position shown in Figure 2.5.

The pion momenta were reconstructed by using 8 drift chambers (DX8~D15). The first five chambers (DX8~DY11) were placed between the target and Q9, and three of them (DX8,DX10,DX12) measured horizontal (X) coordinates and the other two (DY9,DY11) measured vertical (Y) coordinates. The remaining three chambers (D13,D14,D15) measured both X and Y coordinates, placed at the downstream of Q12.

Pions were identified by the time of flight between the ST counter and a scintillation counter S2 placed on the focal plane between D14 and D15. The flight path between ST and S2 was 6.8 meters. Additionally, two horizontally-segmented scintillation counters S3U and S3D were placed behind the D15 chamber, which were used in coincidence with S2.

Pions were further identified with a so-called "muon filter", consisting of an iron block and a scintillation counter (MU), placed at the back end of the Pion spectrometer. The muon filter was used to eliminate muon background from in-flight kaon decays.

Angular acceptance of the spectrometer was about 18 msr and momentum acceptance was $\pm$10%. Actual shapes of these acceptances, obtained from our data, are shown in Appendix C. The energy resolution of the overall spectrometer, measured by using the monochromatic peak of the p(K^-,π^+)Σ^- reaction on a CH_2 target, was 4.2 MeV FWHM (see Appendix B. This value is mainly limited by precision of spectrometer magnet maps).

The Pion spectrometer performances are summarized in Table 2.4.

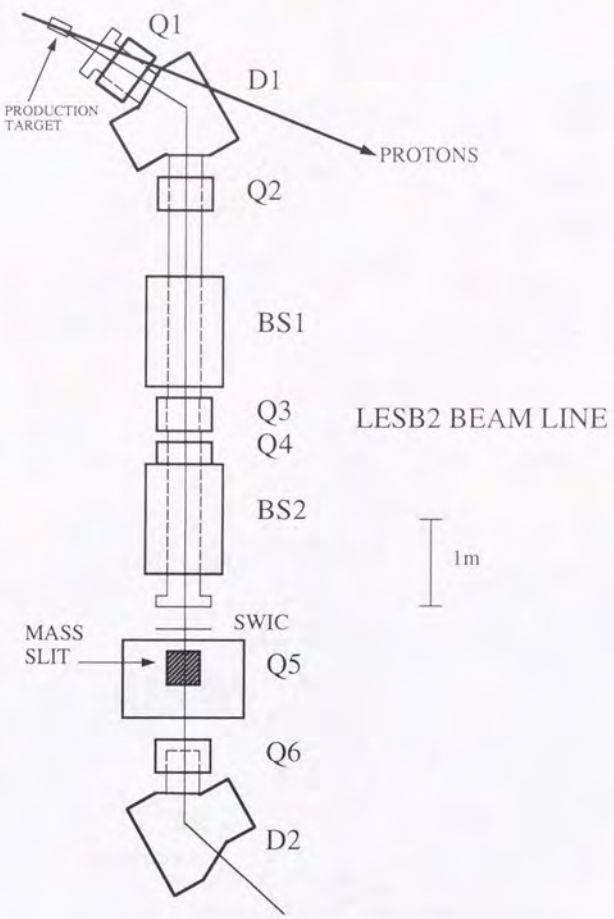

Figure 2.4: Schematic drawing of LESB2(Low Energy Separated Beamline 2).

Pion angular acceptance	18 msr
Pion momentum acceptance	see Figure C.2 in Appendix C
Energy resolution	4.2 MeV FWHM

Table 2.4: Performances of the Pion spectrometer

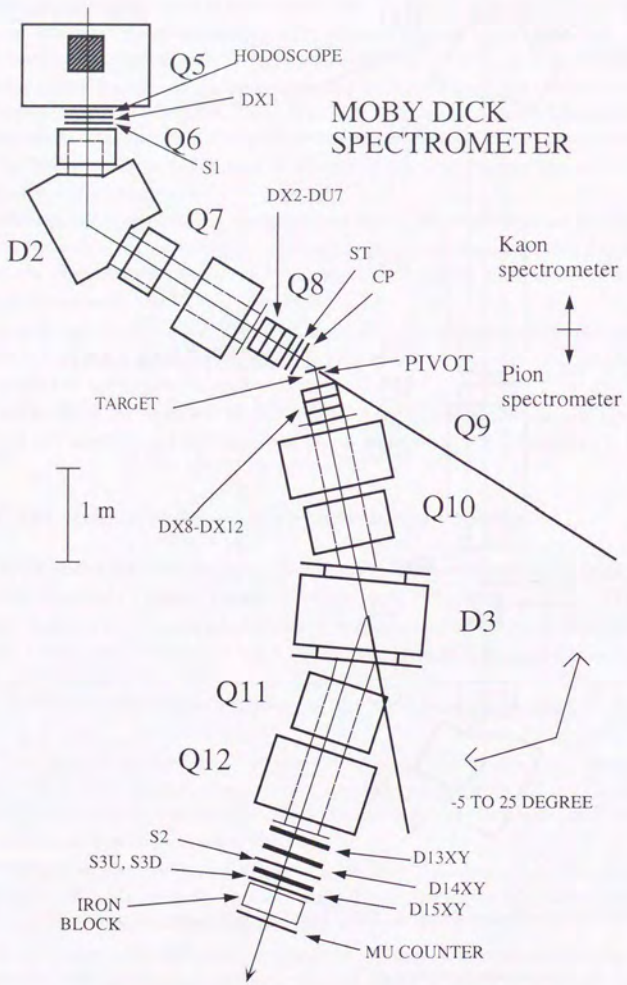

Figure 2.5: Schematic figure of Moby Dick spectrometer.

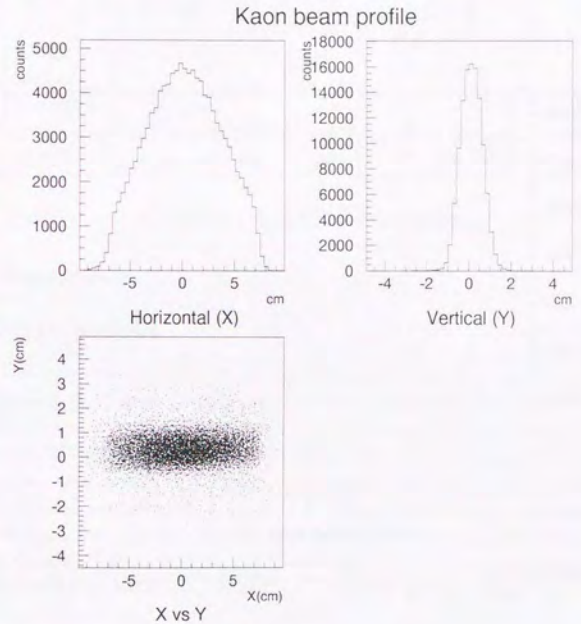

Figure 2.6: Kaon beam profile at the target position

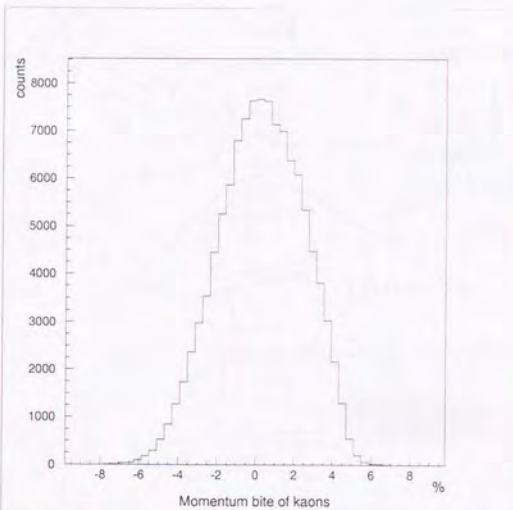

Figure 2.7: Kaon momentum bite in the Kaon spectrometer. Relative momentum (%) to the central (600 MeV/c)

	Name	Operating voltage	Drift distance	Effective area	Gas mixture	Resolution
TYPE1	DX1 DX2 DX4 DX6	-1.1kV(cathode foil) -1.3kV(potential wire)	0.1 inch	5"horizontal 2"vertical	Ar:76% Isobuthane:20% Methylal:4%	250μm(σ)
TYPE2	DU3 DV5 DU7 DX8 DY9 DX10 DY11 DX12	-1.1kV(cathode foil) -1.3kV(potential wire)	0.1 inch	5"horizontal 7"vertical	Ar:76% Isobuthane:20% Methylal:4%	250μm(σ)
TYPE3	D13XY D14XY D15XY	-1.5kV(cathode foil) -2.15kV(potential wire)	0.375 inch	24"horizontal 12"vertical	Ar:76% Isobuthane:20% Methylal:4%	250μm(σ)

Table 2.5: Drift chamber configurations

2.3 Detectors

2.3.1 Drift Chambers

We used 15 chambers whose parameters are summarized in Table 2.5.

Each plane (X or Y) of the chamber had 2 layers of wires shifted by a half cell with each other to resolve left-right ambiguity. X and Y chambers (D1X~D12X) had 24 signal wires in each layer, and XY chambers (D13XY~D15XY) had 32 signal wires in each X layer and 8 signal wires in each Y layer.

Positions were derived from the drift time to the nearest wire. Details of the analysis procedure of the drift chamber will be described later in the analysis chapter. The drift time was measured with common stop TDC's. Signal from each wire was amplified and discriminated at a certain threshold, and was fed into the TDC start. Time clocks of the TDC's were distributed from external clock-generating modules. The TDC which was started by a wire signal was stopped by the main trigger.

2.3.2 Trigger counters

Locations of trigger counters were described in sections 2.1 and 2.2, and were indicated in Figure 2.5. Here we present the detailed information of each counter.

1. Hodoscopes
   Hodoscopes were 8 horizontally segmented 1.95 cm wide scintillators designed to stand high beam intensity and multiplicity, and were located just behind the mass slit. These determined the horizontal positions of incoming kaons and, cooperating with the drift chamber DX1, the direction of projectiles. Each signal from the scintillator was read by a photomultiplier tube and was discriminated for the inputs of TDC, scaler and the multiplicity logic.

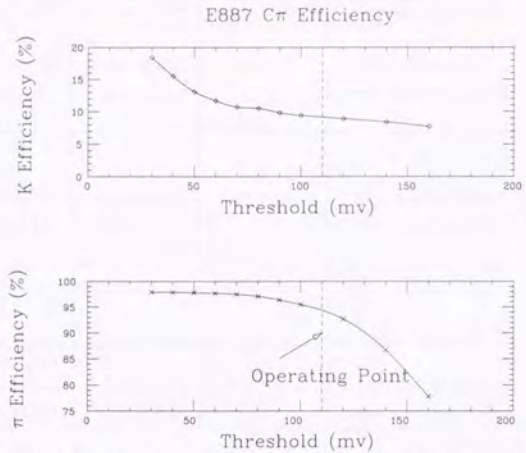

Figure 2.8: CP threshold curve; Upper figure shows the kaon detection efficiency with the threshold value for the summed signal of CPA and CPB. Lower shows the pion detection efficiency. Our operating value is also indicated in the figure.

2. Čerenkov counter(CP)
   CP was a half inch thick threshold type lucite Čerenkov counter and was used for eliminating pion backgrounds in projectiles in the triggers. Signals were read by photomultiplier tubes on both ends (up(CPA) and down(CPB); hereafter, when a counter is viewed by two tubes, we denote them 'A' and 'B'). Analog signals from CPA and CPB were summed up linearly and the resultant signal was discriminated at a certain threshold (see Figure 2.8 for our selection of the threshold) to separate pions and kaons. As seen from Figure 2.8, the pion detection efficiency was about 95 percent.

3. Scintillation counters
   We used 5 scintillation counters for this experiment, S1, ST, S2, S3U and S3D. Each counter has 2 photomultiplier tubes on both ends. Basically every signal from the photomultiplier tube was split into four for the trigger logic, TDC, ADC and scaler. TDC signals were used for the further analysis of particle identification.

Table 2.6 summarizes the physical dimensions and operating conditions of the counters.

2.3.3 Muon filter

In our experimental conditions, muons and electrons from in-flight K^- decays, K_{e3} and $K_{\mu 3}$, cause backgrounds for the (K^-,π^-) reaction (Figure 2.9 shows the decay kinematics of 586 MeV/c kaons with our spectrometer acceptance).

As we mentioned previously, time of flight between ST and S2 provided the primary means of particle identification. However, it is difficult to distinguish muons from pions by TOF alone, because of the small

	Physical dimensions	Counting rates per trigger 4.8×10^4 kaons
Hodoscopes 1	1/8"thick 1.95cm wide	1.8×10^5
2	6cm high	4.1×10^5
3		1.1×10^6
4		1.4×10^6
5		1.4×10^6
6		1.0×10^6
7		3.2×10^5
8		1.7×10^5
S1A	1/4"thick 5.5"wide	4.6×10^6
B	2.5"high	4.6×10^6
STA	1/4"thick 5"wide	1.1×10^6
B	1.25"high	1.2×10^6
CPA	1/2"thick 5"wide	1.1×10^6
B	1.5"high	1.1×10^6
S2A	1/4"thick 24"wide	$1.8\times10^4(\pi^-)$
	3"high	$3.1\times10^3(\pi^+)$
B		$2.4\times10^4(\pi^-)$
		$4.3\times10^3(\pi^+)$
S3UA	1.75"thick 26"wide	$7.6\times10^3(\pi^-)$
	3"high	$6.3\times10^2(\pi^+)$
UB		$1.0\times10^4(\pi^-)$
		$1.1\times10^3(\pi^+)$
S3DA	same as S3UA or B	$1.1\times10^4(\pi^-)$
		$1.3\times10^3(\pi^+)$
DB		$1.4\times10^4(\pi^-)$
		$2.6\times10^3(\pi^+)$
MUA	1/4"thick 30"wide	$2.9\times10^4(\pi^-)$
	12"high	$3.7\times10^4(\pi^+)$
B		$3.0\times10^4(\pi^-)$
		$2.1\times10^3(\pi^+)$

Table 2.6: Trigger counter specifications and the typical counting rates in this experiment

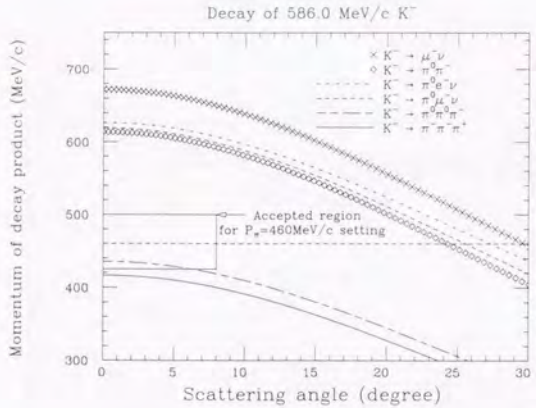

Figure 2.9: Decay in-flight of 586 MeV/c kaon. Accepted region for P_π=460 MeV/c is also indicated. Momenta of particles from 3-body decay are represented by the maximum momenta available.

mass difference (hence small TOF difference) of the two particle species. Additional particle identification power was provided by the muon filter.

The muon filter consisted of an iron block and a scintillation counter (MU) and it literally filtered muon contamination in reaction particles using range differences of pion, electron and muon in iron. MU counter had 2 photomultiplier tubes on both ends (MUA and MUB).

Simulation with CERN program library GEANT[25] was done to optimize the iron thickness, so as to achieve the best muon rejection while minimizing the pion loss. The resultant stopping probabilities (here stopping means that the MU counter did not have any hits) of each particle is shown in Figure 2.10. We decided to use 10 inch-thick iron. The height and width of the iron block were 16 and 32 inches respectively.

2.4 Targets

We used 2 targets, Beryllium (^{9}Be) and Polyethylene (CH_2). Experiment with ^{9}Be is our main purpose of investigating Σ hypernucleus. CH_2 was used to calibrate the spectrometer. Energy resolution and momentum accuracy were checked with the monochromatic peak of Σ^- production reaction K^-+p $\rightarrow$ Σ^-+π^+.

The physical dimensions and weights of both targets were measured precisely as tabulated below.

Target	Thickness	Area	weight
CH_2	2.284g/cm^2 (2.48cm)	9.98cm horizontal × 9.97cm vertical	227.252g
^{9}Be	3.048g/cm^2 (1.65cm)	13.05cm horizontal× 4.92cm vertical	195.818g

Target support was made by a styrofoam. Reactions in the support were completely rejected by a target fiducial volume selection.

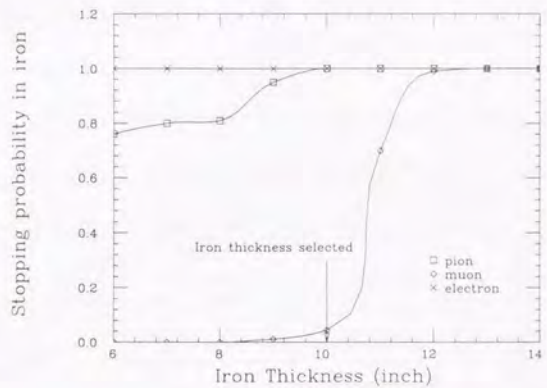

Figure 2.10: Stopping probabilities of 460 MeV/c electron, muon and pion in iron (GEANT simulation)

2.5 Triggers

A schematic diagram of the trigger logic is shown in Figure 2.11.

We used 5 kinds of triggers for this experiment, KB, PIB, KK, PIPI and KPI. All of these triggers were the combinations of simpler triggers KB, PIB, KSCAT and PISCAT, meaning respectively kaon beam, pion beam, kaon scattering and pion scattering. We explain each trigger in detail below.

1. KB trigger
   The kaon beam (KB) trigger flagged a projectile on the target as kaon. Kaons were selected by the time of flight between S1 counter and ST counter and vetoed by the Čerenkov counter signal. An appropriate amount of delay was inserted to the S1 signal, so that S1-ST coincidence (whose timing was determined by the ST signal) selected mostly kaons. The time of flight in nanoseconds between S1 and ST of various particles are tabulated in Table 2.7.

2. PIB trigger
   The pion beam (PIB) trigger flagged a projectile on the target was a pion. Pions were selected with the S1-ST time of flight and using the Čerenkov counter signal in coincidence. The trigger timing was determined by the ST signal.

3. KSCAT trigger
   The kaon scattering (KSCAT) trigger, indicated that an outgoing particle from the target was kaon. Kaons were selected by the time difference between the ST signal and the logical signal SR (see below) and the timing was determined by the ST signal. SR was a coincidence signal of S2 and S3, used to prevent misidentification of an accidental coincidence between ST and S2. S3 signal was a logical OR of S3U and S3D. The timing of SR was determined by the S2 signal. Note that the distance between ST and S2 was 6.8 meters. The time of flight in nanoseconds between ST and S2

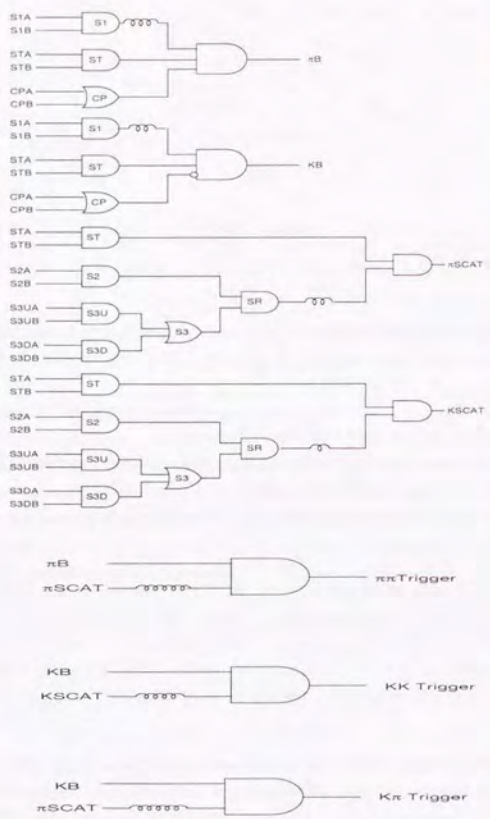

Figure 2.11: Trigger logic diagram for experimental 887

Momentum(MeV/c)	Time of flight	Kaons (nsec.)	Pions (nsec.)	Muons (nsec.)	Electrons (nsec.)
600.	S1−ST(4.1m)	17.6	14.0	13.8	13.6
460.	ST−S2(6.8m)	33.6	23.9	23.5	22.9
550.	ST−S2(6.8m)	30.8	23.6	23.3	22.9

Table 2.7: Time difference of K, π, μ and e for S1−ST and ST−S2

Trigger	Prescale factor	Number of triggers per spill (Without prescale)	Number of triggers per spill (With prescale)
KB	4000	5.8×10^4	14
PIB	100000	1.0×10^6	9.2
KK	1	15	15
PIPI	800	7.7×10^3	9.6
KPI	1	16	16
Total			64

Table 2.8: Prescale factors and numbers of triggers (K^-,π^-) run

of various particles for 460 MeV/c and 550 MeV/c are tabulated in Table 2.7.

4. PISCAT trigger
   The pion scattering (PISCAT) trigger, indicated that the reaction particle was a pion. Pions were selected using the time of flight between the ST and the SR.

The KK, PIPI and KPI triggers were made by the coincidence of KB and KSCAT, PIB and PISCAT, KB and PISCAT respectively. The trigger timing was determined by the beam trigger, PIB or KB. Consequently all of these trigger timing is determined by the ST signal.

All of the PIB, KB, KK, PIPI and KPI triggers were used for the ^{9}Be run and the relative timing of each trigger was adjusted within 1 channel (50 ps) by looking at the TDC spectrum of the ST signal. The KPI trigger was our main trigger, and other triggers were used for calibration purposes. Hence the PIB, KB, KK and PIPI triggers were prescaled so as not to increase the computer dead time of the KPI trigger. Tables 2.8 and 2.9 show the prescale factors and the typical number of triggers per spill.

The KB trigger was used to look at the kaon beam profile. The KK and PIPI triggers were used for the momentum loss correction of each target with the beam through run. The momentum loss correction is described in detail in the Appendix D.

2.6 Stability of the spectrometer magnets

The quadrupole magnets (Q6~Q12) and the dipole magnets (D2 and D3) have hall probes. We periodically (at least once in every 8 hours) checked these hall voltages to maintain constant magnet fields. Consequently the momentum deviations throughout the experiment were less than ±0.5 MeV/c for both the Kaon and Pion spectrometers.

Trigger	Prescale factor	Number of events per spill (Without prescale)	Number of events per spill (With prescale)
KB	2000	5.0×10^{4}	2.5
PIB	400000	8.2×10^{5}	2.0
KK	1	9.7×10^{-2}	9.7×10^{-2}
PIPI	1	3.8	3.8
KPI	1	0.39	0.39
Total			8.8

Table 2.9: Prescale factors and numbers of triggers (K^-,π^+) run

2.7 Other apparatus

Other apparatus supplied at AGS are described below. They were used throughout the experiment to monitor the beam conditions.

1. Secondary emission chamber(SEC)
   SEC is a gas chamber whose output was calibrated to correspond to the number of protons in the C' primary beam line.

2. 90-degree monitor
   90-degree monitor is a small scintillation counter located near the production target in the direction of 90 degrees from LESB2 line and was used to monitor the stability of the beam on the production target.

3. Segmented wire ion chamber (SWIC)
   SWIC was located in front of mass slit of LESB2 beam line and monitored the beam profile.

4. DIBBUK
   DIBBUK is a magnet operating and monitoring system developed in BNL, and was used to remotely set magnet currents and polarities, and also to monitor the magnet status.

5. HP monitor
   HP monitor (Health Physics monitor) is a thin (1/16") scintillation counter for the purpose of radiation safety, located between DX1 and S1 to monitor a number of particles coming to our area.

2.8 Data acquisition and on-line monitor

For each trigger, we read out the drift chamber TDC's, hodoscope TDC's, Čerenkov ADC's and ADC's and TDC's of all other counters. At every interval of the beam spill, we read out the trigger counts and all counters' scalers with the CAMAC standard modules. The prescaled KB, PIB, KK, PIPI and KPI triggers were put into the CAMAC input register in the main crate. We used four CAMAC crates, two near the spectrometer for the drift chamber TDC, and two in the electronics trailer for the counter ADC, TDC and scalers, one of which was the main data-acquisition crate. The three slave crates were connected with a branch highway cable to the main crate.

The data from CAMAC modules are read out by microprocessor-based auxiliary crate controllers into a dual port memory resident in a VME crate. The readout was controlled by a VME-based CES J-11 microcomputer, and the data were subsequently transferred to a DEC microVAX II computer, and then to 8 mm tape cassettes. The on-line displays and controls were controlled by the microVAX II.

Subsequent data reduction and analysis were performed on DEC Vax and Alpha computers.

A typical data taking rate in one of the run, together with computer dead time are tabulated in Tables 2.10 and 2.11.

Trigger	All events after prescale	Accepted events	dead time (%)
K beam	5.28×10^{3}	4.85×10^{3}	8.1
PI beam	3.40×10^{3}	3.10×10^{3}	9.1
KK	5.37×10^{3}	4.85×10^{3}	9.7
PIPI	3.53×10^{3}	3.23×10^{3}	8.5
KPI	6.03×10^{3}	5.41×10^{3}	10

Table 2.10: Typical data-taking rate of the (K^-,π^-) run. Number of events accepted in RUN 41 is tabulated

Trigger	All events after prescale	Accepted events	dead time (%)
K beam	9.42×10^{3}	9.305×10^{3}	1.2
PI beam	7.73×10^{3}	7.64×10^{3}	1.1
KK	368	363	1.4
PIPI	1.42×10^{4}	1.40×10^{4}	1.5
KPI	1.49×10^{3}	1.46×10^{3}	1.7

Table 2.11: Typical data-taking rate of the (K^-,π^+) run. Number of events accepted in RUN 58 is tabulated

The data stored in PDP 11 were accessible from a DEC microVAX, where a more complete on-line analysis, including track reconstruction and particle identification could be done.

Chapter 3

Analysis

In this chapter, we describe analysis procedure to derive final results.

3.1 Overview of the analysis procedure

A running period and total number of accumulated kaons for each run is tabulated below.

Reaction	Running period	Effective running time (hours)	Number of kaons
(K^-,π^-) in Σ region	94/5/22 ~ 95/5/29	133	5.11×10^9
(K^-,π^+) at P_π=438MeV/c	94/5/30 ~ 94/6/4	101	3.29×10^9
(K^-,π^+) at P_π=460MeV/c	94/6/5 ~ 94/6/7	34	9.62×10^8
(K^-,π^-) in Λ region	94/6/27 ~ 94/6/30	16	4.27×10^8

3.1.1 Σ hypernuclear runs

We reconstructed momenta and identified particles of $(K^-,\pi^\pm)$ events in two steps.

In the first pass, the drift chamber data were converted to coordinates, tracks through chambers were reconstructed, and particle momenta were determined with 2nd-order transport matrix. The events which did not have valid hits on chambers were discarded in the first pass.

In the second pass, pion momenta were re-calculated by using a RAYTRACE program[24], which uses the magnetic-field information of the spectrometer magnets. This reconstruction procedure was more time consuming compared with the method used in the first pass, but could achieve better momentum resolution. Energy-loss corrections were then applied to the reconstructed momenta. Also in the second pass, we performed incoming kaon identification by using the S1-ST time of flight, and outgoing pion identification by combining the ST-SR time of flight with the muon filter information.

After the momentum acceptance correction and the efficiency calculation, the cross section of the missing-mass spectrum was derived.

3.1.2 Calibration runs

1. Straight through runs
   Straight-through runs were done to derive the momentum losses of kaon and pion in the target and other materials in the beam line. The basic idea is that the momentum loss in the target

should be the momentum difference of a particle passing straight through in the Kaon and the Pion spectrometer. For this purpose we set the both spectrometers' momenta at the same value (600 MeV/c) and set the Pion spectrometer angle to 0 degree. Selecting KK or PIPI trigger, we could get the momentum loss of kaons or pions, as described in detail in Appendix D.

2. CH_2 run
   Protons in CH_2 were used to observe the peak of the $K^-+p \rightarrow \Sigma^-+\pi^+$ reaction. The data analysis procedure was the same as Σ hypernuclear events and the resultant monochromatic peak in the excitation energy spectrum was used for checking the spectrometer energy resolution and momentum accuracy.

3.2 The first pass

In the first pass, the data were reduced from raw 8 mm data tapes; hodoscope and drift chamber data were converted to the position information, particle trajectories were calculated, momenta were reconstructed, and bad events were rejected.

3.2.1 Trigger selection

First of all, we selected the event trigger type depending on the purpose of the analysis. For the analysis of Σ hypernuclear events, KPI trigger was selected. KB trigger was used to know the kaon beam efficiency, and KK and PIPI trigger were for momentum loss analysis.

3.2.2 Hodoscopes analysis

Figure 3.1 shows the TDC spectra of each hodoscope segment. The TDC spectra were fitted with a single Gaussian on a run by run basis and the data in $\pm$ 2.5 σ were treated as a hit of real particle on that segment of the hodoscope. Thus, the hit position of the particle in the horizontal direction could be determined with the resolution of the segment width (1.95 cm).

3.2.3 Hit position of the drift chamber

As described before, each chamber had 2 staggered wire layers for resolving the left-right ambiguity. Naturally, the time summation of 2 wires should give a constant value for any real particle hits, as indicated by the peak in the time-sum spectra shown in Figs.3.4 and 3.5. Non-constant value in the time sum is supposed to be the fake signal or a particle coming at large angle. These are considered as background and rejected.

Having discarded spurious hits, and solved left-right ambiguity, we converted the drift chamber wire number and TDC information to the physical hit position. This conversion required knowledge of the drift velocity, which was determined by the width of the TDC spectra of the wire signals, assuming that the drift velocity is constant within the drift chamber cells (see Figs.3.2 and 3.3 for the TDC spectra). Considering a wire spacing of the drift chambers (see Table 2.5), we obtained 0.195 mm/(TDC time clock) for the small chambers (DX1 ~ DX12) and 0.167 mm/(TDC time clock) for the big chambers (D13, D14 and D15). With this analysis, we got 250μm(σ) position resolution in each chamber.

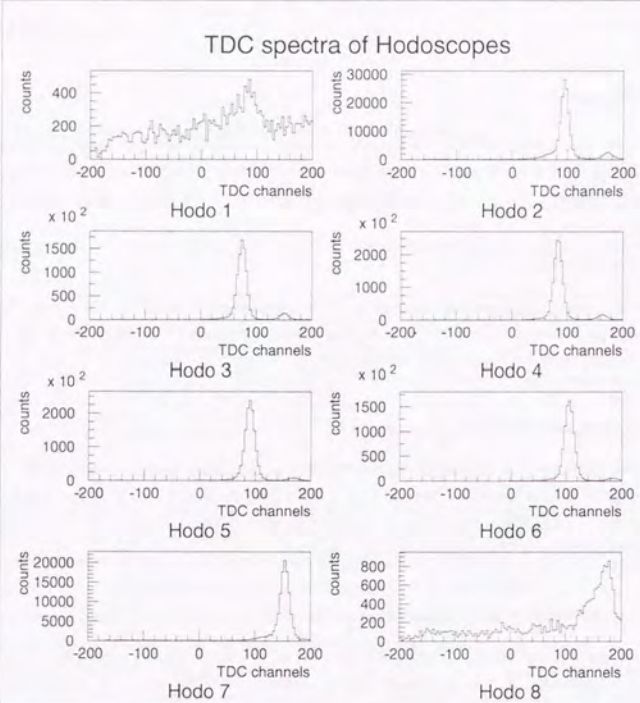

Figure 3.1: TDC spectra of all hodoscope segments

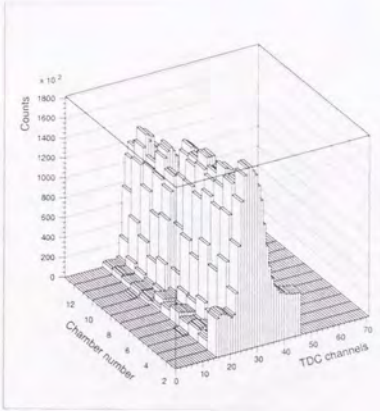

Figure 3.2: Timing signal of drift chamber wires (DX1∼DX12). Chamber number 1∼12 corresponds to DX1∼DX12 ,respectively

Efficiencies of individual chambers were calculated from the number of hits in each chamber under the condition of "non beam track" (explained later in Section 3.2.6) and the results are summarized in Table 3.1.

3.2.4 Tracking of a particle

The tracking was done separately in 4 regions. We name these regions as the mass slit area, the upstream target area, the downstream target area and the downstream pi area.

For each region (except for the mass slit area where we had no Y chamber), we fit straight lines through chamber hit points, treating horizontal and vertical track segments independently. These track segments were used to obtain X, Y, dX/dZ, dY/dZ on the spectrometer focal planes, which were then used to reconstruct particle momenta. The track segments were also used to reconstruct reaction vertex in the second pass of the analysis.

Each area has several chambers as tabulated in Table 3.2

The track selection criteria in each area are described below.

1. Mass slit area

   Since the redundancy in tracking is limited (we only have a hodoscope and a X chamber) while rate is high in the mass-slit area, we rejected the event when the hodoscope multiplicity is ≥ 2 ($\sim$1 % of all events). The X position of the incoming particle was determined as follows:

   Case 1

   When both hodoscope and DX1 have hits, we used the position obtained by DX1. If there are multiple hits on DX1, we selected the hit position closest to the hodoscope hit position.

   Case 2

   When hodoscope has no hit, and DX1 multiplicity is one, we used the position obtained by DX1.

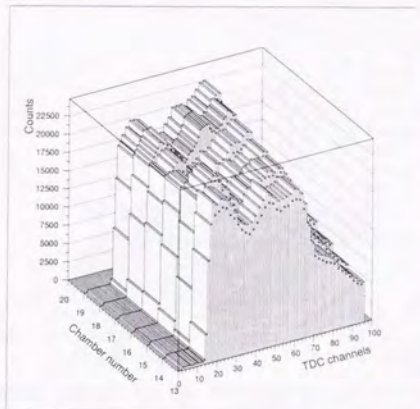

Figure 3.3: Timing signal of drift chamber wires (DX13~DX15). Chamber number 13 and 14 is D13X and D13Y, 15 and 16 is D14X and D14Y, 17 and 18 is D15X and D15Y.

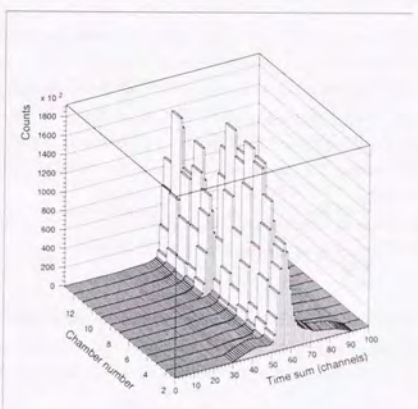

Figure 3.4: Time sum of drift chamber layers (DX1~DX12). Chamber number 1~12 corresponds to DX1~DX12 ,respectively

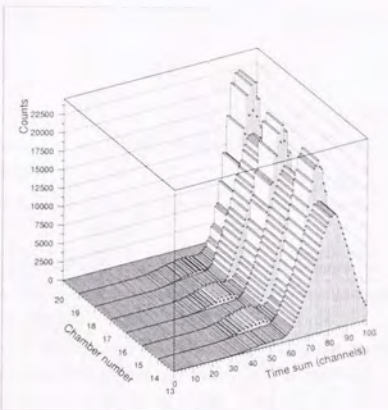

Figure 3.5: Time sum of drift chamber layers (DX13~DX15). Chamber number 13 and 14 is D13X and D13Y, 15 and 16 is D14X and D14Y, 17 and 18 is D15X and D15Y.

Detector name	Total events	hits=0 (%)	hits=1 (%)	hits=2 (%)	hits≥3 (%)	Average hits/events
HODO	32661	9.2	90.8	0.0	0.0	0.908
DX1	32661	6.1	72.8	15.0	6.1	1.211
DX2	32661	4.0	84.9	9.4	1.7	1.088
DU3	32661	1.3	86.2	10.3	2.2	1.134
DX4	32661	0.5	87.9	10.0	1.6	1.127
DV5	32661	1.5	86.2	10.2	2.1	1.129
DX6	32661	0.8	87.8	9.9	1.5	1.120
DU7	32661	1.6	86.5	9.8	2.1	1.125
DX8	32661	5.5	86.1	7.0	1.5	1.044
DY9	32661	2.9	84.6	10.1	2.3	1.118
DX10	32661	3.5	88.5	6.5	1.4	1.059
DY11	32661	2.9	84.9	9.8	2.4	1.117
DX12	32661	1.3	89.3	7.7	1.6	1.096
DX13	32661	6.8	87.2	5.3	0.7	0.999
DY13	32661	6.0	89.2	3.0	1.8	1.006
DX14	32661	3.7	91.3	4.4	0.5	1.017
DY14	32661	3.9	92.1	2.7	1.2	1.012
DX15	32661	6.5	83.6	8.4	1.5	1.048
DY15	32661	3.3	89.9	5.2	1.6	1.052

Table 3.1: Drift chamber efficiencies in KPI trigger (RUN42) gated by "non beam track" condition

Area names	Chambers	Position(cm)
Mass slit	Hodoscopes	-451.6
	DX1	-447.8
Upstream target	DX2	-71.9
	DU3	-67.9
	DX4	-54.7
	DV5	-50.6
	DX6	-39.3
	DU7	-35.2
	PIVOT(FOCUS)	0.0
Downstream target	DX8	20.6
	DY9	28.1
	DX10	32.4
	DY11	36.9
	DX12	41.3
Downstream pi	D13X	621.9
	D13Y	624.4
	D14X	644.6
	D14Y	647.1
	FOCUS	659.5
	D15X	667.2
	D15Y	669.7

Table 3.2: Drift chamber configuration and positions relative to the focus point of the spectrometer.

Case 3
When DX1 has no hit and hodoscope multiplicity is one, we assumed that the particle hit the center of the hodoscope.

In all other cases, we rejected the events.

2. Other three areas
These areas have 3 horizontal and 3 vertical chambers except for the downstream target area which has only 2 vertical chambers.

Tracking was done separately in the horizontal and vertical direction, and the strategy to get the tracks is the same for both X and Y.

We took a hit position on the 1st chamber, and drew a straight line to one of the hit positions on the 2nd chamber, and then computed the residue between the one of the hit points and the calculated position on the 3rd chamber. If there are multiple hits on the 2nd and 3rd chamber, this process was repeated for all possible combinations, and the combination which minimizes the residue is chosen. The residue histograms for selected track segments are shown in Figure 3.6. Then from the selected 3 points, we obtained a straight line with least-squares fit.

This process was repeated for all the hit positions on the 1st chamber, so that there could be multiple track segment candidates for each tracking areas.

If one of the 3 chamber had no hit, we drew a straight line with all combinations of hit positions on the other two chambers. In this case the number of tracks is the same as the smallest number of hits in either chamber. Note that though we did not use these events in further analysis, this conditions is useful to know the respective chamber efficiency (as shown in Table 3.1).

If two of them had no hit, we rejected the event*.

After selecting the tracks with the criteria described above, we imposed a so-called "redundancy cut". This cut required that the residue on the 3rd chamber (i.e., the difference between the hit point and calculated position) should be within ± 0.2cm, and was found to be effective in eliminating particle decays between chambers.

3.2.5 The tracking throughout the spectrometer and momentum determination

In the first pass, particle momenta were determined by the tracking information with the second-order transport matrix of each Kaon and Pion spectrometer. Elements of the transport matrices are shown in Appendix A. Here, we describe the momentum determination of the Pion spectrometer; the momentum reconstruction of the Kaon spectrometer was done in a similar fashion.

Using the track segments reconstructed in the chambers, we deduced the X, Y, dX/dZ and dY/dZ at the front and rear focal planes of the Pion spectrometer.

*In the case of the downstream target area which had only 2 vertical chambers, the reconstruction procedure was slightly different: If both of 2 had at least one hit, we drew a straight line and proceeded normally. However, if there was no hit on either chamber, we needed a special treatment. In this case, we prepared a transport matrix at the chamber position, and fed the Y coordinate of the hit into the matrix in order to reconstruct the momentum. Since we cannot directly obtain dY/dZ in the downstream target area (which information is needed to reconstruct the reaction vertex), we took the track segment in the downstream pi area and traced it back to the downstream target area once the momentum reconstruction was done, and used the calculated dY/dZ when reconstructing the vertex.

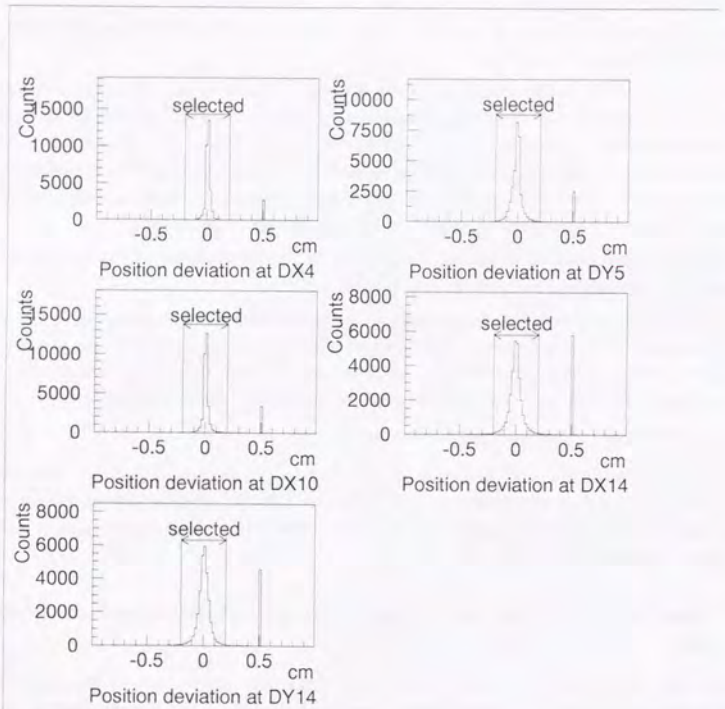

Figure 3.6: Position deviations (measured − predicted) on 3rd chambers on each area. In the case of no hit on 3rd chamber, events were accumulated at +0.5 cm

Using these values, we determined the momentum relative to the central momentum ($\delta P/P$) by solving the following 2nd-order polynomial equation with respect to $\delta P/P$ with the Newton methods,

$$\begin{aligned} X' &= C(X'/X)\times X + C(X'/\theta)\times\theta + C(X'/(\delta P/P))\times\delta P/P \\ &\quad + C(X'/X^2)\times X^2 + C(X'/(X\theta))\times X\times\theta + C(X'/\theta^2)\times\theta^2 \\ &\quad + C(X'/Y^2)\times Y^2 + C(X'/(Y\phi))\times Y\times\phi + C(X'/\phi^2)\times\phi^2 \\ &\quad + C(X'/(X\delta P/P))\times X\times\delta P/P + C(X'/(\theta\delta P/P))\times\theta\times\delta P/P + C(X'/(\delta P/P)^2)\times\delta P^2, \end{aligned}$$

where $C()$ are the transport matrix coefficients for each element, X' is the horizontal position at the front focal plane, X, Y, θ=dX/dZ, ϕ=dY/dZ are the horizontal position, vertical position, horizontal angle and vertical angle respectively at the rear focal plane.

Using the momentum derived as above and dX/dZ, Y, dY/dZ at the rear focal plane, we predicted the dX/dZ, Y, dY/dZ at the front focal plane with the transport matrix. From the difference between the predicted and the measured values, reduced χ^2 was calculated as follows, which was used to check the goodness of the overall tracking in the Pion spectrometer:

$$\chi^2 = \frac{(\frac{dX/dZ_{pred}-dX/dZ_{meas}}{\sigma_{dX/dZ}})^2 + (\frac{Y_{pred}-Y_{meas}}{\sigma_Y})^2 + (\frac{dY/dZ_{pred}-dY/dZ_{meas}}{\sigma_{dY/dZ}})^2}{3}$$

where $\sigma_{dX/dZ}$, σ_Y and $\sigma_{dY/dZ}$ were determined by fitting the residue distributions(Figure 3.7) with 2 gaussians. As shown, residue distributions have narrow (good tracks) and wide (false tracks) components, and we use the standard deviations of the narrow components to calculate the χ^2. The values are $\sigma_{dX/dZ}$=3.1 mrad, σ_Y = 0.20 cm and $\sigma_{dY/dZ}$ = 11.7 mrad. For those which has no measured dY/dZ values such that only one Y chamber hit in the downstream target area, dY/dZ_{pred} - dY/dZ_{meas} was set to 0 and χ^2 was divided by 2 instead of 3. In case there are multiple track-segment candidates, we computed the χ^2 for all combinations, and selected the combination which gave the best χ^2 value. Figure 3.8 is the χ^2 distribution for a typical (K^-,π^-) run. In the first pass, χ^2 was cut at 100 for rough selection of good tracks.

3.2.6 Event summary of the first pass

Events selection summary of the first pass is tabulated in Table 3.3. In the table, the "beam track" refers to the condition where track segment candidates were found both at the entrance and exit of the Kaon spectrometer. The "non beam track" refers to the condition where track segments candidates were found in all 4 tracking areas.

3.3 The second pass

In the second pass, we recalculate pion momenta using the RAYTRACE program, reconstruct reaction vertex, and identify incoming K^- and outgoing π^-.

3.3.1 Accurate pion momentum determination

The second order transport matrix is not adequate to know momenta of particles shifted over ±5% from the central momentum. Thus, RAYTRACE program was used to solve this problem. RAYTRACE

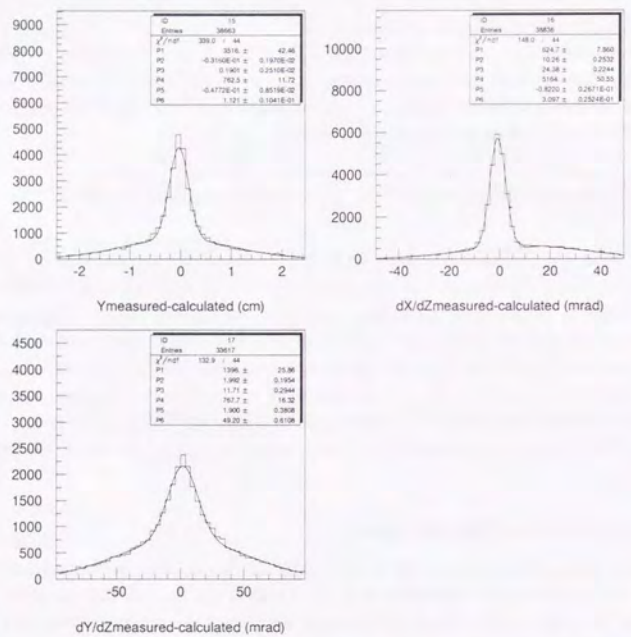

Figure 3.7: dX/dZ, Y and dY/dZ deviations for the (K^-,π^-) run. Fitting was done with 2 gaussians. Cut applied: non beam track, redundancy cut and target vertex cut.

	Trigger	Event Selection	Events
^{9}Be(K^-,π^-) run	KB trigger	All	1085337
		Beam track	925737
		Redundancy cut	821913
	KPI trigger	All	1408500
		Non beam track	278909
		Redundancy cut	137529
^{9}Be(K^-,π^+) run at 438 MeV/c	KB trigger	All	180123
		Beam track	153738
		Redundancy cut	137463
	KPI trigger	All	26608
		Non beam track	14935
		Redundancy cut	7354
^{9}Be(K^-,π^+) run at 460 MeV/c	KB trigger	All	98356
		Beam track	85441
		Redundancy cut	74405
	KPI trigger	All	4781
		Non beam track	2502
		Redundancy cut	1235
^{9}Be$(K^-,\pi^-)^9_\Lambda$Be run	KB trigger	All	37603
		Beam track	31489
		Redundancy cut	24963
	KPI trigger	All	305155
		Non beam track	92552
		Redundancy cut	34056

Table 3.3: Event summary of the first pass for each run condition as for KB and KPI trigger. This presents how many events were survived through each event selection.

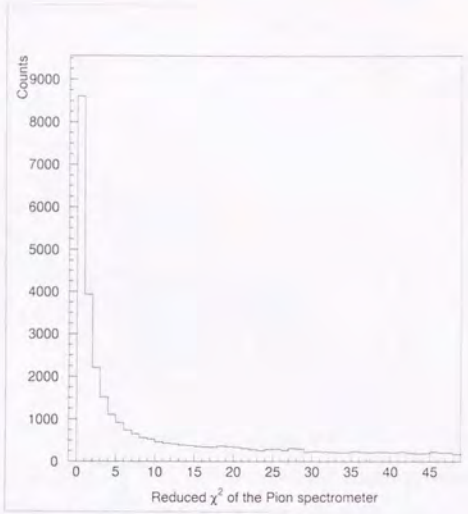

Figure 3.8: Reduced χ^2 for the (K^-,π^-) run. Cut applied: non beam track, redundancy cut and target vertex cut

program adjusts the momenta and the trajectories of particles to minimize the deviations of Y, dY/dZ and dX/dZ using the magnetic field map of the Pion spectrometer. After this correction, the reduced χ^2 distribution is improved(see Figure 3.9 compared with Figure 3.8). We selected $\chi^2 \leq 5.0$ as the good pion tracks as indicated in Figure 3.10.

3.3.2 Target vertex cut

The target is placed at the spectrometer pivot (Z=0). By extrapolating the incoming kaon and outgoing pion tracks onto the target, we reconstructed the reaction vertex for each event. The distribution of the reconstructed vertex positions for the ^{9}Be(K^-,$\pi^\pm$) runs are shown in Figs.3.11$\sim$ 3.13. Selected vertex regions are also indicated in the figures.

Note that in Figure 3.11, no particle identification was imposed on the outgoing particle while in Figure 3.12 electrons and muons were rejected. The background in the vertex distributions, Z-distribution in particular, is clearly reduced after particle identification. This is because the kaon in-flight decay backgrounds are suppressed by the electron and muon rejection.

The Z-vertex distributions in Figures 3.12, 3.13 were fitted with 2 gaussians plus a linear background to see the vertex resolution (see figures 3.14, 3.15). The resultant width of Z vertex was 1.7 cm in RMS. Deconvoluting the real thickness of the target of 1.65 cm, we obtained the vertex Z resolution to be 2 cm in FWHM.

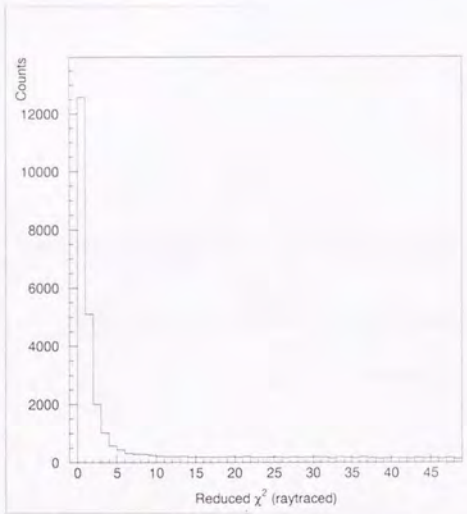

Figure 3.9: Reduced χ^2 distribution of the (K^-,π^-) run after adjusting the pion momenta with RAYTRACE program

3.3.3 Incoming K^- identification

Although kaons were selected by the flight time at trigger level, the KB trigger may have some pion contamination since there are an order of magnitude more pions than kaons coming down the beam line. Such pions could be easily rejected based on the time of flight information from S1 to ST, as shown in Figure 3.16. As shown, the pion contamination in the KB trigger is less than 1 %.

3.3.4 Outgoing π^- identification

The most severe backgrounds in our experiment are in-flight K^- decay products. For the convenience, we tabulate the branching ratios of the relevant K^- decay mode.

Decay mode	Branching ratio(%)
$\mu^-\nu_\mu$	63.51
$\pi^-\pi^0$	21.16
$\pi^-\pi^-\pi^+$	5.59
$\pi^-\pi^0\pi^0$	1.73
$\mu^-\nu_\mu\pi^0$ ($K_{\mu 3}$)	3.18
$e^-\nu_e\pi^0$ (K_{e3})	4.82

To illustrate the contribution of the K^- decays to our background, we simulated K^- decays using the GEANT program under the following conditions:
1. The number of generated kaons was 10^8

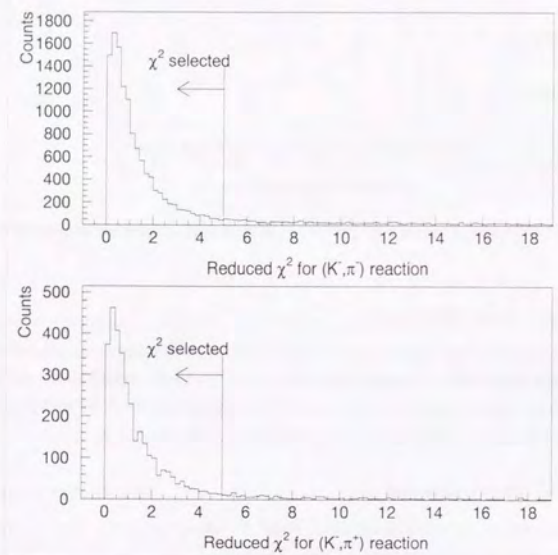

Figure 3.10: Selected region for good track events in χ^2 distributions of both (K^-,$\pi^\pm$) run

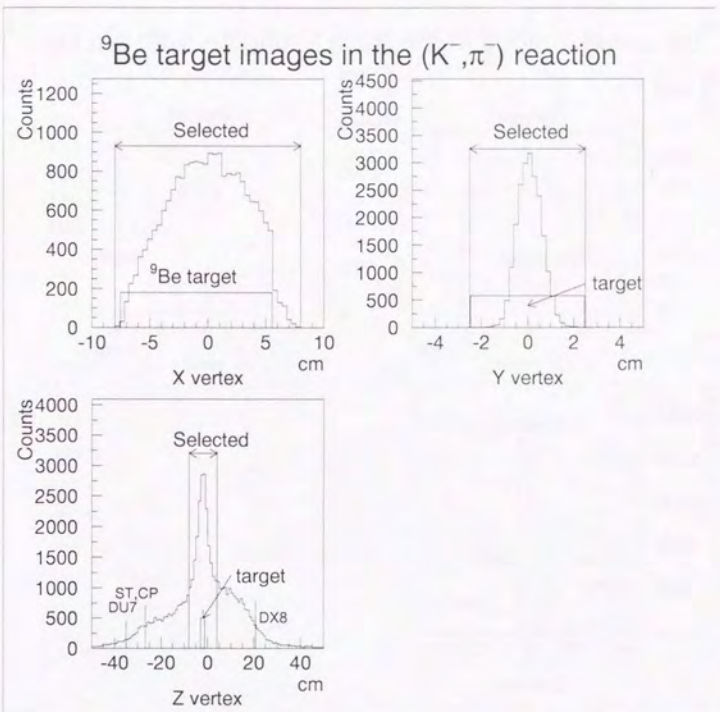

Figure 3.11: ^{9}Be target vertex image in the (K^-,π^-) reaction. Cut applied:K beam TOF (described in the next section), χ^2 and the other 2 vertices cut.

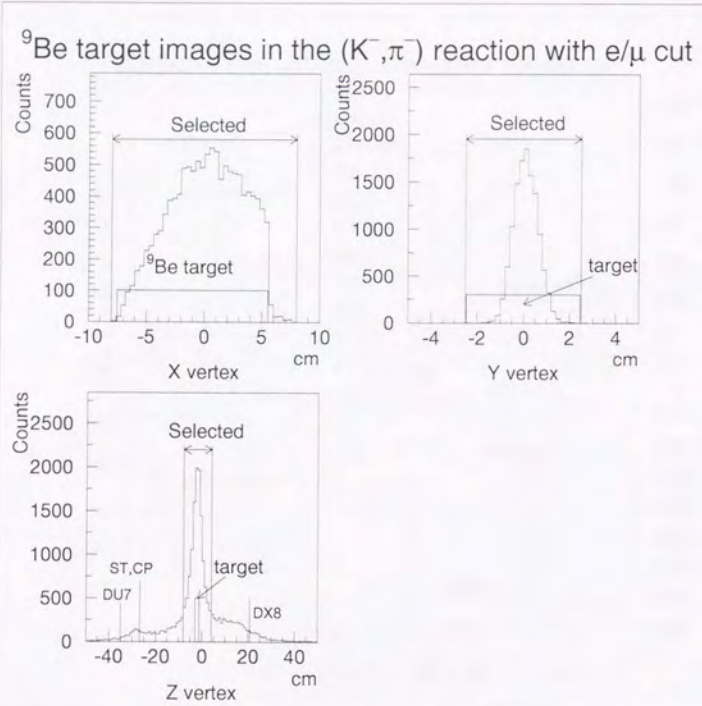

Figure 3.12: ^{9}Be target vertex image in the (K^-,π^-) reaction. Cut applied:K beam TOF, χ^2, other 2 vertices cut and muon electron cut (cut conditions of K beam TOF and μ/e selection will be described in next section).

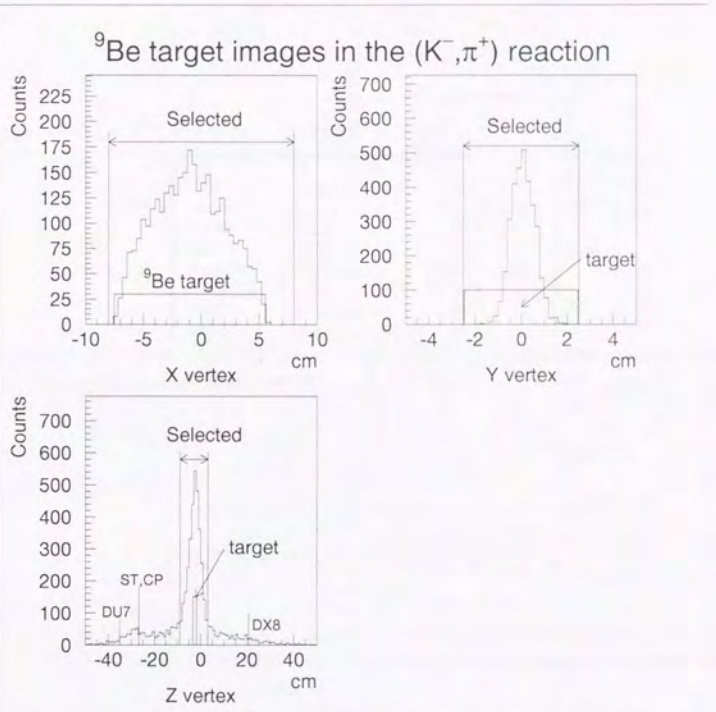

Figure 3.13: ^{9}Be target vertex image in the (K^-,π^+) reaction. Cut applied:K beam TOF (described in the next section), χ^2 and other 2 vertices cut.

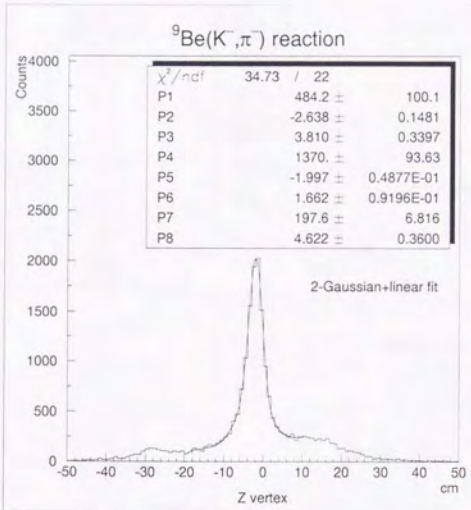

Figure 3.14: Z vertex distribution of the (K^-,π^-) reaction in Figure 3.12 was fitted with 2 gaussians and linear background. Function used to fit is P1×exp$(-0.5(\frac{Z-P2}{P3})^2)$ + P4×exp$(-0.5(\frac{Z-P5}{P6})^2)$ + P7 + P8×Z.

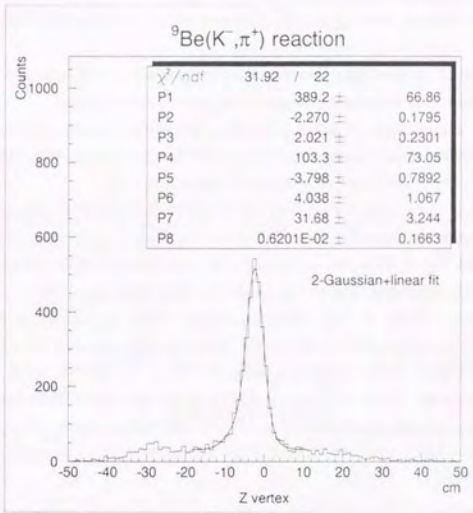

Figure 3.15: Z vertex distribution of the (K^-,π^+) reaction in Figure 3.13 was fitted with 2 gaussians and linear background. Function used to fit is P1×exp$(-0.5(\frac{Z-P2}{P3})^2)$ + P4×exp$(-0.5(\frac{Z-P5}{P6})^2)$ + P7 + P8×Z.

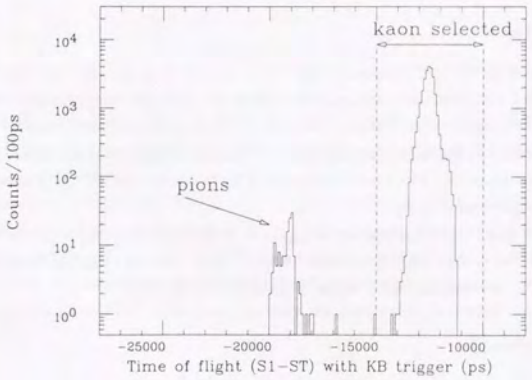

Figure 3.16: TOF spectrum between S1 and ST of KB trigger without any event selection

2. The decay vertices were required to be inside the target region.
3. Only the charged decay products entering the effective area of the drift chamber DX12 were recorded.

The momentum spectra of the positive- and negative-charged decay products are shown in Figure 3.17, together with the momentum acceptance range of the present experiments.

As shown, electrons and muons from in-flight K_{e3} and $K_{\mu 3}$ decays can cause background in ^{9}Be(K^-,π^-) reaction in Σ region. Note that there are no decay-pion contribution to our data, except for the low-momentum edge of the $P_\pi = 438$ MeV/c setting of the π^+ spectrum.

In order to reject electrons and muons, we measured TOF between ST and SR, whose time spectrum is shown in Figure 3.18; all event selections (π^- beam rejection, tracking χ^2 and vertex) have been applied. In calculating the flight time, the pathlengths of the particles were taken into account and corrected. As shown, the π-μ-e are not well separated, due to the small π-μ time difference.

With the help of the muon filter, we can eliminate muons. When a hit was recorded in the MU counter, we assumed that a muon penetrated the muon filter ion, and rejected the event (see the MU counter TDC spectrum in Figure 3.19). With the muon rejection, the ST-SR TOF spectrum clearly exhibits two peaks of electrons and pions, as shown in Figure 3.20. We accept the events from 5000ps to 7000ps as the pion. We also show in the figure the result of a 2-Gaussian deconvolution. Based on this fit, we estimate that the pion loss due to the time of flight cut is about 3%, and electron contamination in the pion sample is about 5%.

3.3.5 Possible background passing through the second pass

After all event selection described up to now, we still have background. These backgrounds are classified in 2 categories. One is the non-target related background and comes from a K^- decay at the target region. The other is the target related background and comes from the reaction of incident kaon on the target nucleus.

Non target related background

In the Z vertex figures of the (K^-,$\pi^\pm$) reaction (Figs. 3.12, 3.13, 3.14, 3.15, note that data shown in all these figures have passed the event selection by now.), there are constant background below the target images. Since we took the empty target data for both (K^-,$\pi^\pm$) runs, we overlayed them on the ^{9}Be data with the same event selection (Figure 3.21, 3.22). Empty data are multiplied so as to compare with the ^{9}Be target data with the same number of incident kaons. This factor for the (K^-,π^-) empty run is 10.1 and for the (K^-,π^+) empty run is 10.8.

As clearly seen from these figures, constant background underneath the target profile is not target-related event. It should be in-flight K^- decay background. Thus the non-target related background is completely eliminated by subtracting empty target data from the ^{9}Be data.

Target related background

Main background sources of the reaction of kaon on the target nucleus are K^0 decay of the charge exchange reaction $K^- + p \rightarrow K^0 + n$, and K^- decay of the K^- elastic scattering.

Monte carlo simulation of both of the K^- elastic scattering and K^-+p→K^0+n were done using the existing K^-N data[28][34] considering the Fermi motion of nucleus in ^{9}Be.

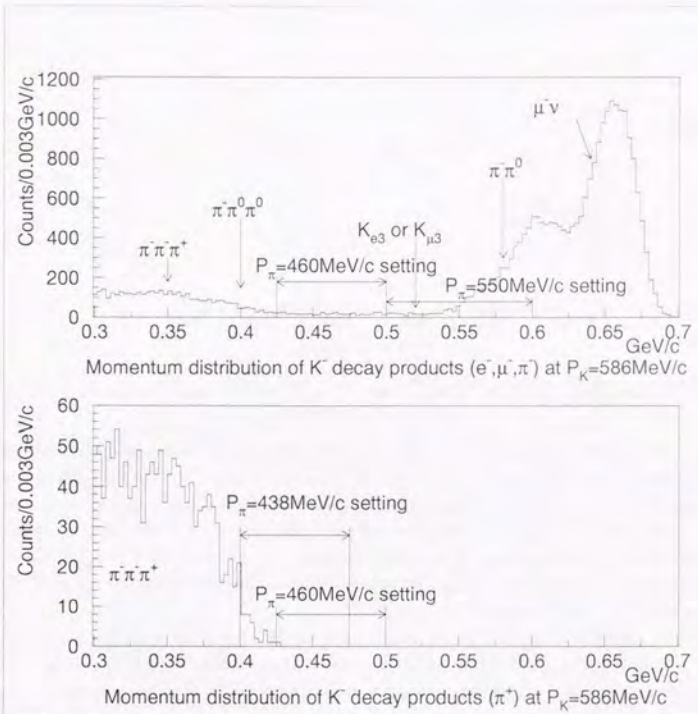

Figure 3.17: Simulated momentum distribution of the decay products from 586 MeV/c K^-, which enter the effective area of the drift chamber DX12. Upper figure shows the momentum distribution of negative charge particles(e^-, μ^- and π^-) which cause background in the (K^-,π^-) reaction and lower figure represents that of positive charge particle(π^+) which cause background in the (K^-,π^+) reaction. Generated numbers of kaon is 10^8. The decay vertexes are required to be inside the target region.

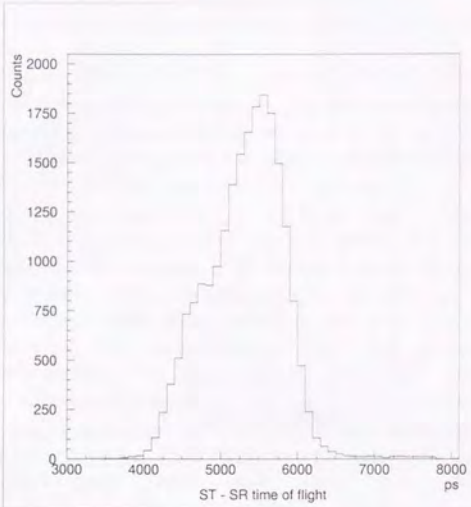

Figure 3.18: Pathlength-corrected time of flight from ST to SR with the target vertex and χ^2 selection

π^+'s or π^-'s from the decay of K^0 make flat momentum distribution over whole momentum region acceptable to our experimental setting (see Figure 3.23). These π^+'s and π^-'s cause the same amount of background in both $(K^-,\pi^\pm)$ reaction. Looking at the cross section spectrum of the (K^-,π^+) reaction (Figure 4.10 in the next Chapter), amount below EE (excitation energy) < 0 MeV should come from K^0 decay background. Thus averaging the cross section of the (K^-,π^+) reaction from EE $= -20$ MeV to EE $= 0$ MeV, we get $2.9\pm1.7\mu$barn/sr/2MeV in the excitation energy for contribution of K^0 decay background. This is also true for the (K^-,π^-) reaction.

As for the K^- elastic scattering, acceptable amount of decay products from K^- is 1/4 of π^- from K^0 decay. Mainly these particles are electrons and muons, and flatly distributed in those momentum. Thus, contribution of the K^- elastic scattering supposed to be less than 1 μbarn/sr/2MeV in the excitation energy spectrum of the (K^-,π^-) reaction.

3.3.6 Event summary of the second pass

Event selection summary of the second pass is tabulated in Table 3.4.

3.4 Overall Efficiencies

3.4.1 Kaon beam related efficiency

1. Kaon decay between ST and the target

   Kaon beam was defined at the scintillation counter ST before the target.Since ST is separated from

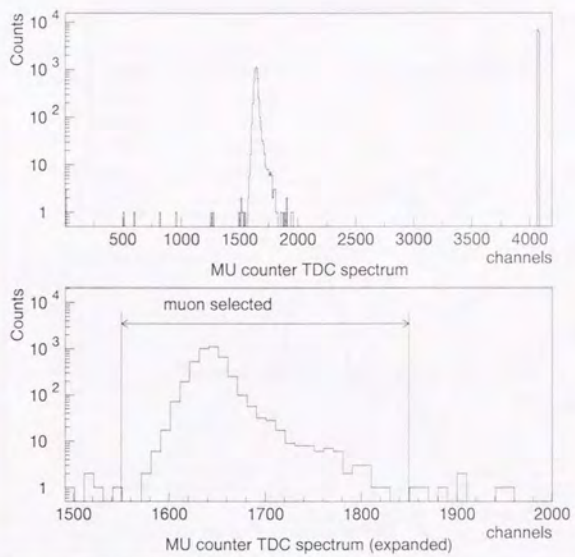

Figure 3.19: TDC distribution of the MU counter [^{9}Be(K^-,π^-) run]. Selected region as muon is indicated in the bottom figure

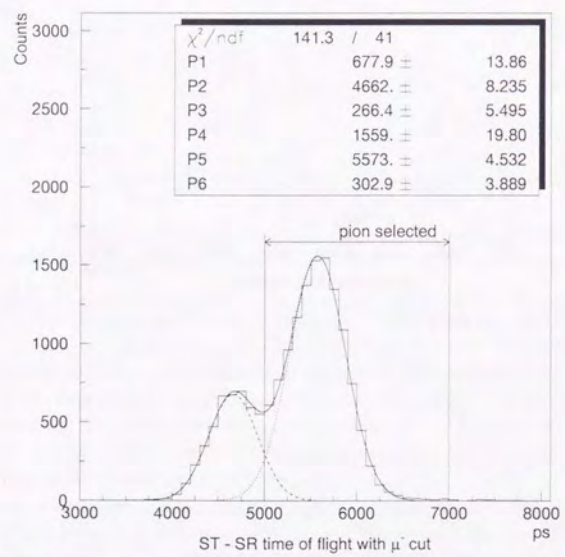

Figure 3.20: Pathlength corrected time of flight from ST to SR with the target vertex and χ^2 selection, and muon elimination. Solid line: 2-Gaussian fit (P1×exp$(-0.5(\frac{X-P2}{P3})^2)$ + P4×exp$(-0.5(\frac{X-P5}{P6})^2)$) of electrons and pions.

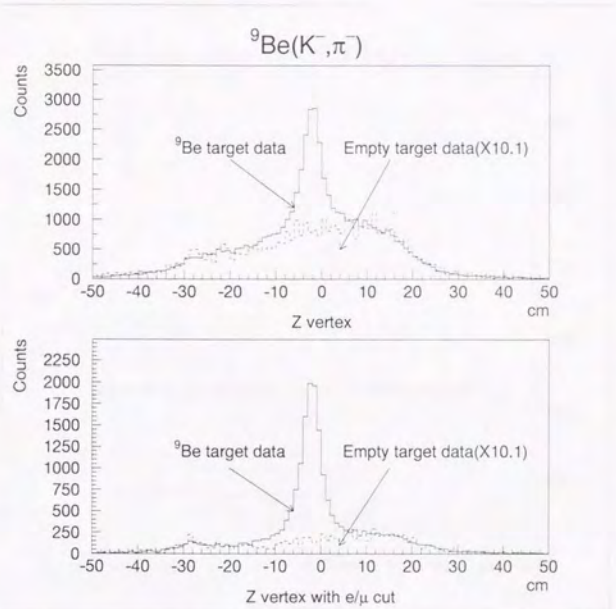

Figure 3.21: Target Z vertex in the (K^-,π^-) reaction. Empty target data (dashed) is overlayed on the ^{9}Be data (solid). Upper figure is the same one in Figure 3.11, and lower is in Figure 3.12. In both figures, empty data are selected with the completely same criteria as ^{9}Be data. Empty target data are multiplied by 10.1 times so as to compare with ^{9}Be data with the same number of incident kaons.

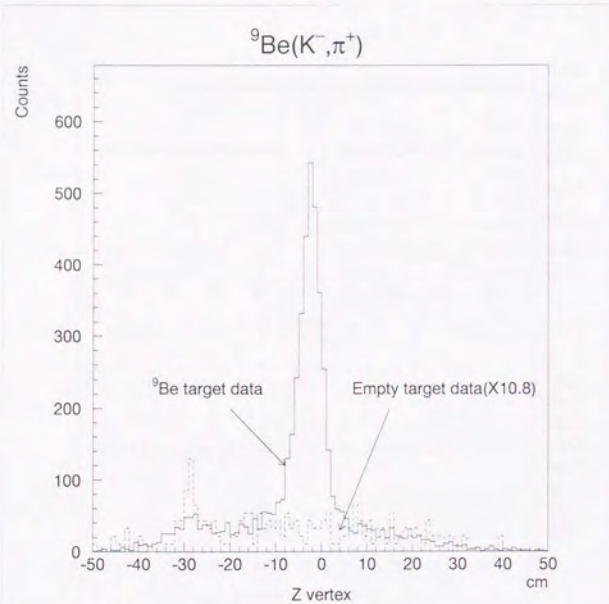

Figure 3.22: Target Z vertex in the (K^-,π^+) reaction. Empty target data (dashed) is overlayed on the ^{9}Be data (solid). Figure is the same one in Figure 3.13. In this figure, empty data are selected with the completely same criteria as ^{9}Be data. Empty target data are multiplied by 10.8 times so as to compare with ^{9}Be data with the same number of incident kaons.

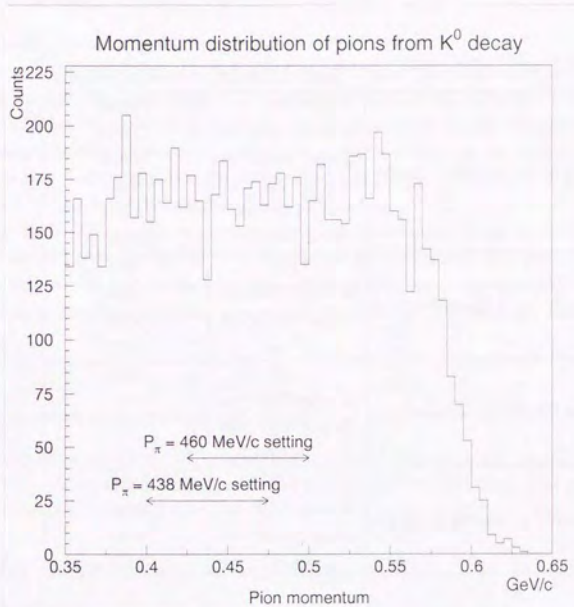

Figure 3.23: Monte carlo simulation of momentum distribution of π^-'s from K^0 decay at the DX12 position. K^0 is produced via the p(K^-,K^0)n reaction. Arrows indicate the momentum region acceptable to our experimental setting of P_π = 460 MeV/c and 438 MeV/c.

	Event Selection	Numbers of events
^{9}Be(K^-,π^-) in the Σ region	All	136290
	K beam TOF cut	135981
	Target vertex cut	38924
	χ^2 cut	21251
	Mu TDC cut	16516
	Pion TOF cut	12060
^{9}Be(K^-,π^+) P_π=438MeV/c	All	7377
	K beam TOF cut	7374
	Target vertex cut	3802
	χ^2 cut	3018
^{9}Be(K^-,π^+) P_π=460MeV/c	All	1238
	K beam TOF cut	1237
	Target vertex cut	715
	χ^2 cut	573
^{9}Be(K^-,π^-) in the Λ region	All	33245
	K beam TOF cut	33145
	Target vertex cut	9530
	χ^2 cut	5778

Table 3.4: Event summary of the second pass for each run condition as for KPI trigger. Number of events indicates how many events were survived through the event selection.

the target in 26.7 cm, a certain fraction of kaons decay before reaching the target. Detail will be described later in Section 3.4.4.

2. Pion contamination in the kaon beam
   We know how many pions are in the KB trigger from the analysis of the time of flight between the S1 and ST. Then the actual number of kaons in the kaon beam scaler counts can be estimated. Typically pion contaminations is less than 1 % in this experiment. The run by run basis kaon beam counts efficiencies are tabulated in the third column of Table 3.5. The total scaler counts of the kaon beam multiplied by these efficiencies were used for the actual number of kaons which came down on the target.

3. Effective number of kaons for $K\pi$ reactions
   Because the horizontal widths of the experimental targets (^{9}Be[13cm wide] and CH_2[10cm wide]) are smaller than the kaon profile (±7cm), some of kaons in the peripheral region may miss the target. This can be corrected by comparing the kaon profile at the KB trigger and the KPI trigger at the target position. Kaon beam profile (KB profile) was shown in the previous chapter in Figure 2.6. The kaon horizontal profiles for KPI events (KPI profile) is shown in Figure 3.24. The actual procedure to determine the effective number of kaons were;
   Looking at the KPI profiles, we defined the width of the target image as −7cm to 6cm for ^{9}Be, and -5.5cm to 5.5cm for CH_2. Then we counted the number on the KB profile histogram inside the defined regions. We took as the kaon beam efficiency the ratio of this number to the total number in the KB profile; the efficiencies were found to be 96% for the ^{9}Be target and 90% for the CH_2 target.

3.4.2 Computer data-taking efficiency

The data-taking efficiency for the KPI trigger was calculated from the scaler counts of the KPI trigger with and without the computer busy signals. The run by run basis KPI event "live time" (data-taking efficiency) is tabulated in Table 3.5.

3.4.3 Drift chamber and tracking efficiencies

1. Tracking efficiency
   The tracking efficiency was calculated from the each chamber's efficiency gated by "Non beam track" condition (already tabulated in Table 3.1) and tabulated in the fifth column of Table 3.5 on the run by run basis.

2. Redundancy cut
   Since tracks within ±2mm were accepted by the redundancy cut, while the chamber resolution was 200μm, we ignored the correction due to the redundancy cut.

3. χ^2 cut
   Figure 3.25 compares the tracking χ^2 distribution with the χ^2 distribution of degree of freedom = 3. As shown, the distribution is fairly well represented by the χ^2 function, and we assume that the tracking χ^2 distribution for true events are indeed represented by the χ^2 (d.o.f=3). Under this assumption, we estimated the event loss to be 0.02% for the χ^2 cut at 5.

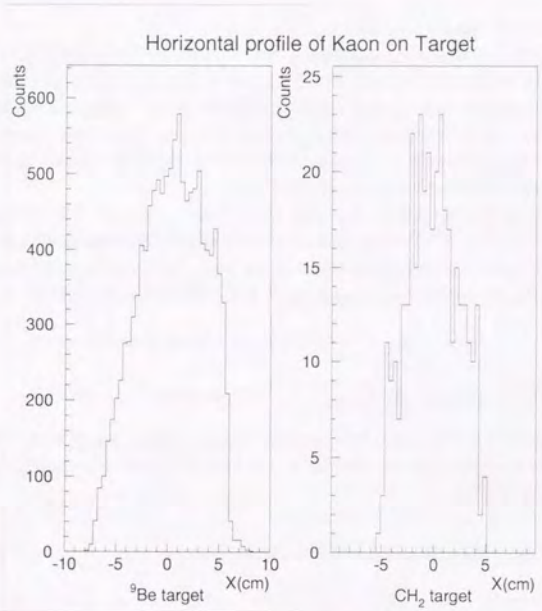

Figure 3.24: Kaon horizontal profiles in KPI events on both ^{9}Be and CH_2 target. Event selection is the same as the final results.

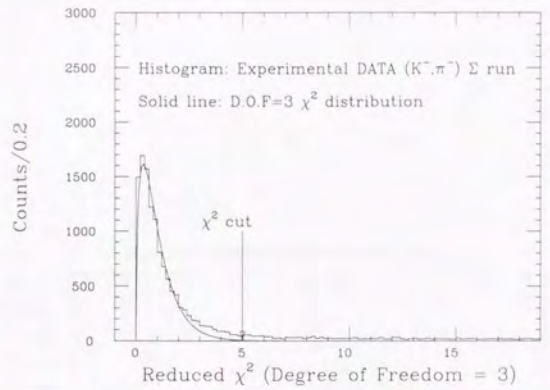

Figure 3.25: χ^2 distribution of degree of freedom = 3 (solid line) with our experimental reduced χ^2 data (histogram)

4. Vertex cut
   As can be seen from Figures 3.11 ~ 3.13, X and Y vertex cut do not lead to any event loss. We only need to consider the Z vertex cut efficiency, which was evaluated by fitting the vertex distribution with gaussians as shown in Figure 3.14. About 95 % of events were in the selected vertex region.

3.4.4 Kaon's and pion's decay correction

Kaon's and pion's survival probability is evaluated by the following equation;

$$P_{sub} = exp(-\frac{L}{\beta\gamma c\tau})$$

where L is the pathlength, β(v/c) the particle velocity, $\gamma=1/\sqrt{1-\beta^2}$, c light velocity, τ particle life time.

Using the pathlengths and the velocities of the actual events we calculated the survival probabilities (see Figures 3.26 and 3.27). For kaons, the pathlength was evaluated from the hit position at ST and the target. For pion, that was derived from the transport matrix.

Then we estimated decay correction factors taking the mean values as tabulated below. Errors due to this estimation are less then 1 % for kaon decay and about ±5 % for pion decay.

	correction factor
Kaon	0.95
^{9}Be(K^-,π^-) in the Σ region	0.78
^{9}Be(K^-,π^+) P_π=438MeV/c	0.76
^{9}Be(K^-,π^+) P_π=460MeV/c	0.77
^{9}Be(K^-,π^-)$^9_\Lambda$Be	0.81

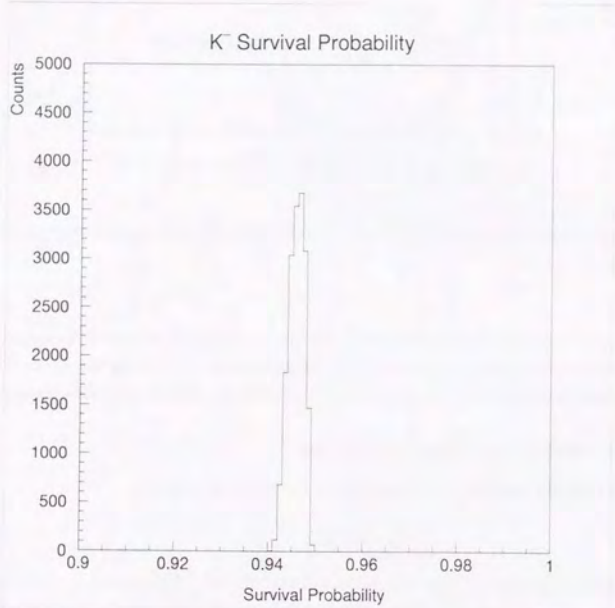

Figure 3.26: Survival probability of incoming kaons between ST and the target estimated using the experimental data.

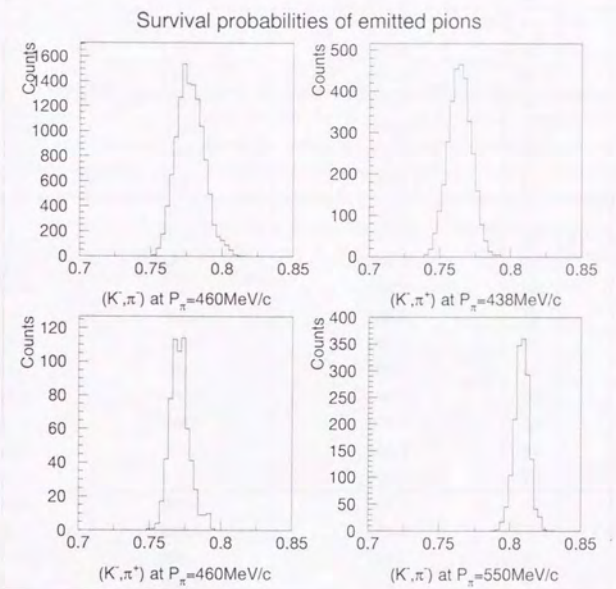

Figure 3.27: Survival probabilities of emitted pions estimated using the experimental data for each run conditions.

	Run	Actual Kaon in kaon scaler	KPI event Live time	Tracking efficiency
^{9}Be(K^-,π^-)	37	0.994	0.862	0.549
in the Σ region	38	0.994	0.910	0.580
	39	0.995	0.918	0.593
	41	0.990	0.897	0.542
	42	0.994	0.916	0.594
	43	0.992	0.913	0.592
	44	0.995	0.922	0.550
	45	0.994	0.919	0.487
	46	0.991	0.905	0.581
	47	0.992	0.910	0.575
	48	0.992	0.911	0.595
	49	0.993	0.915	0.601
	50	0.994	0.935	0.619
	51	0.994	0.930	0.616
	52	0.992	0.922	0.604
	53	0.994	0.948	0.613
^{9}Be(K^-,π^+)	57	0.992	0.979	0.595
at P_{π^+}=438 MeV/c	58	0.993	0.983	0.611
	59	0.993	0.987	0.591
	60	0.997	0.996	0.546
	61	0.994	0.989	0.669
	62	0.890	0.971	0.573
	63	0.992	0.989	0.581
	64	0.993	0.987	0.612
	65	0.973	0.989	0.589
	66	0.992	0.989	0.597
	67	0.994	0.988	0.590
^{9}Be(K^-,π^+)	76	0.990	0.989	0.610
at P_{π^+}=460MeV/c	77	0.994	0.983	0.627
	78	0.995	0.985	0.575
	79	0.992	0.986	0.400
	80	0.994	0.981	0.548
	81	0.995	0.986	0.562
	82	0.996	0.986	0.522
^{9}Be(K^-,π^-)	149	0.994	0.888	0.451
in the Λ region	150	0.994	0.888	0.461
	151	0.994	0.879	0.485
	156	0.954	0.882	0.454

Table 3.5: The run by run basis event efficiencies. Actual numbers of kaons in the kaon scaler counts (Section 3.4.1.2), the live time of KPI events (Section 3.4.2) and the tracking efficiency (Section 3.4.3.1) are presented.

3.4.5 Summary of efficiencies

Average value of each efficiency is tabulated below.

	K decay	K beam	K on target	Live time	Tracking	Vertex	π decay	Total
^{9}Be(K^-,π^-) in Σ region	0.95	0.99	0.96	0.92	0.59	0.95	0.78	0.36
^{9}Be(K^-,π^+) at P_π=438 MeV/c	0.95	0.98	0.96	0.98	0.59	0.95	0.76	0.37
^{9}Be(K^-,π^+) at P_π=460 MeV/c	0.95	0.99	0.96	0.98	0.57	0.95	0.77	0.37
^{9}Be(K^-,π^-) in Λ region	0.95	0.98	0.96	0.88	0.46	0.95	0.81	0.28

From another approach, we also derived the analysis efficiency. Monte carlo simulation of K^- decay products in the ^{9}Be(K^-,π^-) reaction at P_π = 460 MeV/c were performed to compare the empty target (K^-,π^-) data. In the simulation, accepted K^- decay products at the target region were 407 electrons from K_{e3}, 338 muons from $K_{\mu 3}$, 10 pions from $\pi^-\pi^0\pi^0$ decay and 11 pions from $\pi^-\pi^-\pi^+$ decay for 5×10^8 kaons. Total number of accepted decay products is 766. On the other hands, in the empty target data which has the same number of incident kaons as above simulation, accepted events at the target region considering the vertex resolution showed in Figure 3.14 are 333. We derive analysis efficiency for the ^{9}Be(K^-,π^-) reaction at P_π = 460 MeV/c as 0.43.

Chapter 4

Results

Here we present the excitation energy spectra of the ^{9}Be(K^-,π^-) reaction in the Λ region and the ^{9}Be(K^-,$\pi^\pm$) reactions in the Σ region. The procedure to get the final spectra are;

1. The excitation energy calculation
   From the momenta of incident kaons and outgoing pions, and the scattering angles of pions, the excitation energy of the hypernucleus is calculated for each reconstructed event.
2. The momentum acceptance correction
   The excitation energy spectra are then corrected for the momentum acceptance of the Pion spectrometer, as described in the Appendix C.
3. The cross section derivation
   Number of counts in the acceptance-corrected excitation energy spectra are then converted to the cross section using the number of kaons, the number of target nuclei, the angular acceptance of the pion spectrometer (see Appendix C) and the overall efficiencies.

4.1 Definition of the excitation energy

The definition of the excitation energy (EE) is
EE = (Mass of hypernucleus) − (Mass of system of the residual nucleus and a hyperon),
so that bound states would appear in the EE < 0 region.

Excitation energy of hypernucleus is calculated as follows:

$$E_H = E_K + M_{tgt} - E_\pi$$
$$EE = \sqrt{{E_H}^2 - {P'_K}^2 - {P'_\pi}^2 + 2P'_K P'_\pi \cos\theta_{scat}} - M_H$$
$$P'_K = P_K - Ploss_K$$
$$P'_\pi = P_\pi + Ploss_\pi$$

,where
P_K and P_π ; Momentum measured by the spectrometer
$Ploss_K$ and $Ploss_\pi$; Momentum losses of K^- and $\pi^\pm$
E_K and E_π ; Total energies of K^- and $\pi^\pm$

M_{tgt} ; Rest mass of the target nucleus
E_H ; Total energy of the hypernucleus
M_H ; Mass of the system of residual nucleus and a hyperon with the binding energy = 0
EE ; Excitation energy of the hypernucleus

Nuclear and particle masses used for analysis are tabulated below. Nuclear masses were taken from "The 1993 ATOMIC MASS EVALUATION" [26] and hyperon masses were from Review of Particle Properties[27].

	Mass (MeV/c^2)
^{9}Be	8392.8
^{8}Be	7454.9
^{8}Li	7471.4
Λ	1115.63
Σ^+	1189.37
Σ^0	1192.55
Σ^-	1197.43

4.2 Cross section

Cross section was calculated from the following equation:

$$\text{Cross-section}(\mu b/sr) = \frac{\text{N(data)}}{\text{N(kaons)} \times \text{N(tgt)} \times \epsilon \times \text{Acc}}$$

,where N(data); Number of events in the spectrum
N(kaons); Number of kaons accumulated
N(tgt); Number of target nucleus per μbarn
ϵ; Overall efficiency
Acc; Angular acceptance(sr) of Pion spectrometer

4.3 ^{9}Be(K^-,π^-) data in the Λ region

4.3.1 Background rejection

As shown in Figure 3.17, the main background to the Λ production region are pions from $K^- \to \pi^-\pi^0$ decay and muons from $K^- \to \mu^-\nu$. These events have the strong correlation between the excitation energy and the scattering angle (see Figure 4.1).

We can see from Figure 4.1 that the $\mu^-\nu$ decay does not emerge in the EE > −20MeV region. However, the $\pi^-\pi^0$ decay can cause the background around EE = 0 MeV, which we rejected by reconstructing the missing π^0 mass from momenta of kaon and pion, and the pion scattering angle assuming $K^- \to \pi^-\pi^0$ decay kinematics. The reconstructed missing mass spectrum is shown in Figure 4.2; the result of a 2-Gaussian fit to the missing mass spectrum around the π^0 mass shows that the absolute energy scale is accurate within 0.3 MeV.

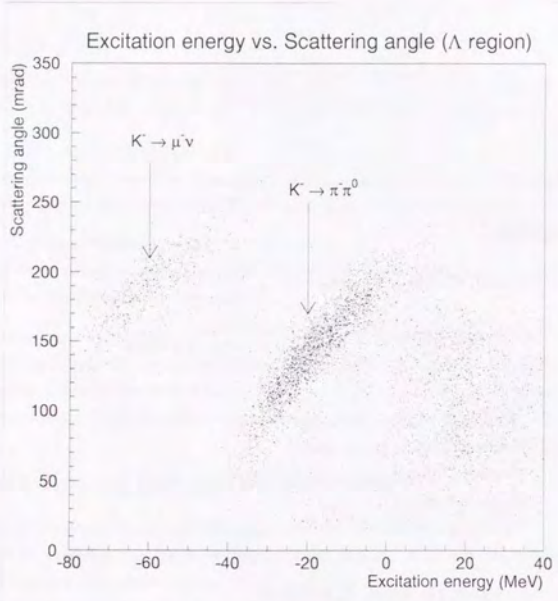

Figure 4.1: Excitation energy vs $K\pi$ scattering angle of the ^{9}Be(K^-,π^-) reaction in the Λ region.

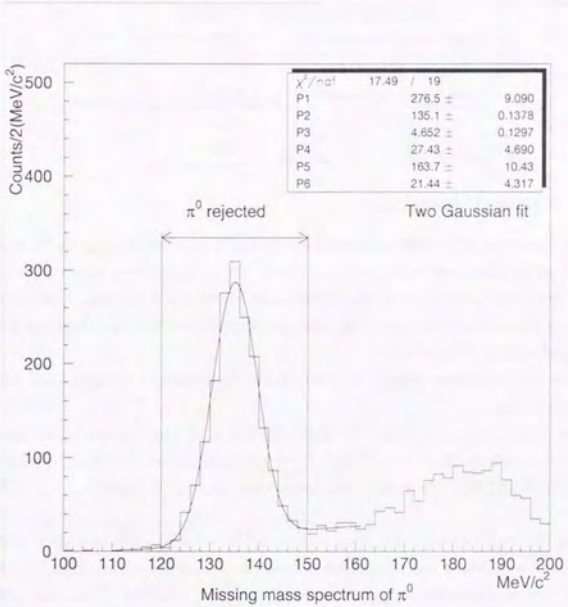

Figure 4.2: Missing π^0 mass spectrum assuming $K^-\rightarrow\pi^-\pi^0$ decay kinematics

4.3.2 Systematic errors for the $^{9}_{\Lambda}$Be cross section

We tabulate below the systematic errors for the cross section due to several corrections. The total error indicated at the bottom of the table were calculated by assuming that all error sources could be added in quadrature. Since the systematic errors change the overall scale of the cross section but individual data points in the spectra, the error bars in the spectra presented hereafter reflect statistical errors only.

Correction	systematic error
Kaon decay correction	+1%
	−0%
χ^2 cut	+10%
	−0%
Pion decay correction	±5%
Angular acceptance	±10%
Momentum acceptance	±20%
Total	+25%
	−23%

4.3.3 Excitation energy spectrum

The excitation energy spectrum of the $^{9}_{\Lambda}$Be is shown in Figures 4.3, 4.4 and 4.5. Figure 4.3 is a spectrum obtained after the all event selections were applied. Figure 4.4 is a spectrum where correction of the Pion spectrometer momentum acceptance on the spectrum in Figure 4.3 is applied. Also the acceptance curve used is plotted in the same Figure 4.4. The reaction cross section was calculated as a function of excitation energy and plotted in Figure 4.5.

In these figures, the EE (excitation energy) = 0 MeV is the Λ production threshold and EE > 0 MeV represents the Λ unbound region.

Two big peaks are clearly seen around EE = 7 MeV and EE = 19 MeV. Also a small peak is visible below the Λ production threshold (EE = ∼−7 MeV). For comparison, we show the $^{9}_{\Lambda}$Be data taken at CERN in Figure 4.6([1][29][39][40]). Note that their data were taken at 0 degrees at P_K = 720 MeV/c (shown in Figure 4.6).

In the CERN data, three peaks were also observed at EE = −7 MeV, EE = 6 MeV and EE = 17 MeV. The peak positions are almost the same as in our result. Hence we assume that the three peaks found in our spectrum are of the same configurations as those found at CERN. Then, the assignment of the three peaks are as follows,

1. EE = −7 MeV
   The ground state of $^{9}_{\Lambda}$Be of the configuration $(p^{-1}_{3/2}(n), s_{1/2}(\Lambda))$, where $p^{-1}_{3/2}(n)$ denotes that there is a neutron hole in the $p_{3/2}$ orbit and $s_{1/2}(\Lambda)$ denotes that the Λ is in the $s_{1/2}$ orbit. Similar notations will be used hereafter without further notice. From the emulsion data, the ground state energy is known to be EE = −6.71±0.04 MeV[35].

2. EE = 7 MeV
   The substitutional $(p^{-1}_{3/2}(n), p_{3/2}(\Lambda))$ state. The ^{9}Be(p,d) pickup experiment([48][49]) indicated that the $p_{3/2}$ neutron-hole state is distributed in many levels on a ^{8}Be core. The ones with large spectroscopic factors are at 2 MeV and 18 MeV excitation energies, to which a Λ can couple to

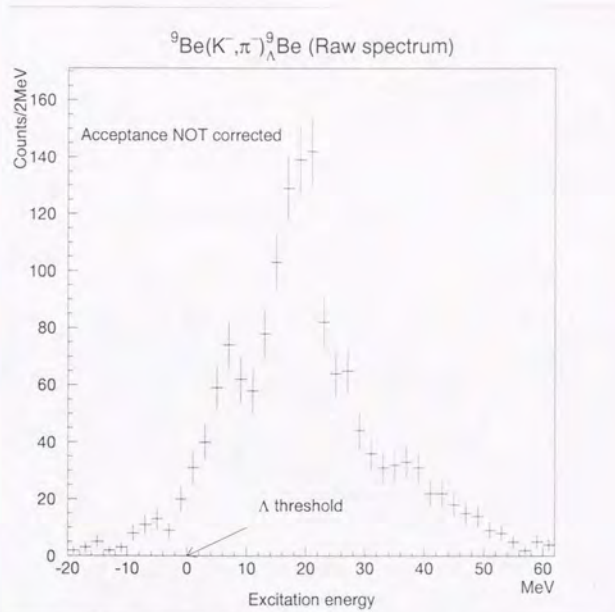

Figure 4.3: Spectrum of of ^{9}Be(K^-,π^-)$^{9}_{\Lambda}$Be reaction as a function of excitation energy(EE). The vertical axis is number of counts per 2 MeV. EE = 0 MeV is Λ production threshold. EE > 0 MeV represents the Λ unbound region.

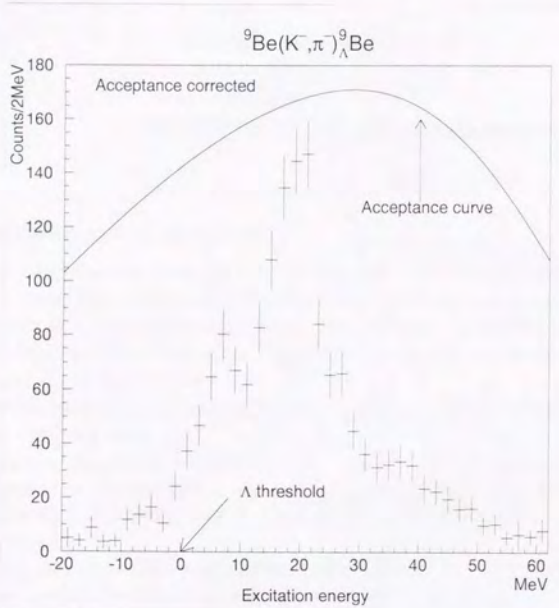

Figure 4.4: Acceptance-corrected spectrum of of ^{9}Be(K^-,π^-)$^{9}_{\Lambda}$Be reaction as a function of excitation energy(EE). The vertical axis is number of counts per 2 MeV. Acceptance curve used is indicated in solid line. EE = 0 MeV is Λ production threshold. EE > 0 MeV represents the Λ unbound region.

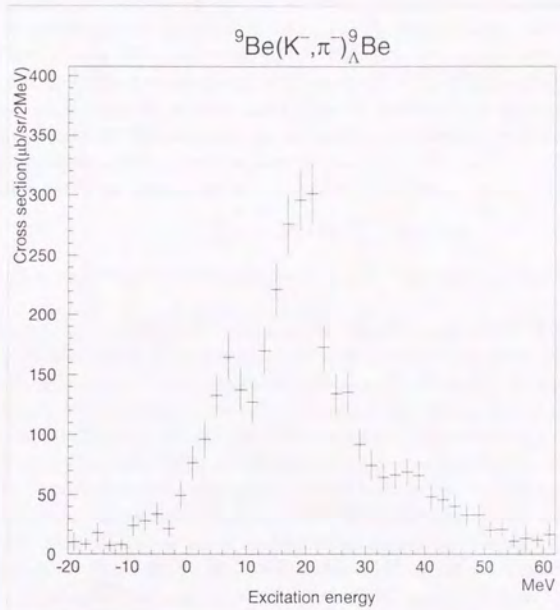

Figure 4.5: Cross section plot of ^{9}Be(K^-,π^-)$^{9}_{\Lambda}$Be reaction as a function of excitation energy(EE). Correction of the spectrometer momentum acceptance was applied. EE = 0 MeV is Λ production threshold. EE > 0 MeV represents the Λ unbound region.

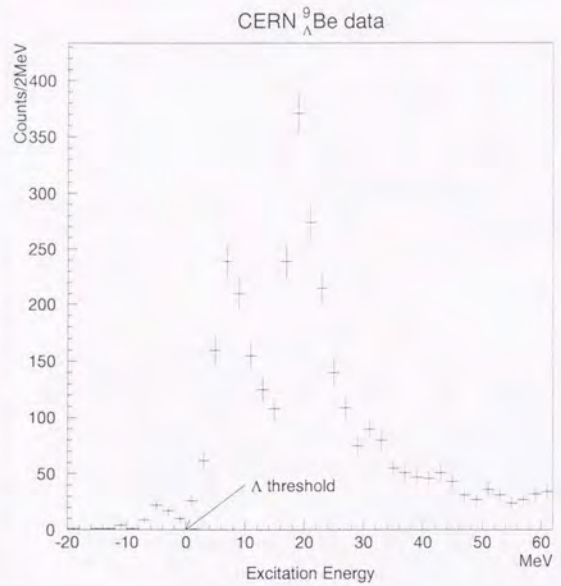

Figure 4.6: $^{9}_{\Lambda}$Be data obtained at CERN[1]. Horizontal axis is the excitation energy with the same scale as our data. Vertical axis is number of counts per 2 MeV. These data were taken at P_K = 720 MeV/c and Pion detection angle at 0 degree.

form a $^{9}_{\Lambda}$Be hypernucleus. The peak at EE = 7 MeV is considered to have a 3 MeV excited core coupled with a Λ in the substitutional $p_{3/2}$ orbit.

3. EE = 19 MeV
   The substitutional $(p^{-1}_{3/2}(n),p_{3/2}(\Lambda))$ state. A Λ is coupled to the $p_{3/2}$ neutron-hole state in core ^{8}Be with 18 MeV excitation energy. In addition, there should be contribution from the substitutional $(s^{-1}_{1/2}(n),s_{1/2}(\Lambda))$ state, taking into accounts the separation energy difference between $p_{3/2}$ and $s_{1/2}$ neutrons.

Because it is impossible to distinguish the resonance peaks from the Λ quasi-free continuum, we cannot discuss each peak qualitatively. Instead, we deduce the total strength of Λ production (bound + continuum) by summing up the contents in the spectrum. The summed region was from EE = −10 MeV to EE = 75 MeV because there must be no Λ production below the ground state (EE = ∼ −7 MeV); beyond EE = 75 MeV where the production of Σ^0 starts, the Λ contribution cannot be separated from the Σ strength, but it should be relatively small. Then we obtained the energy-integrated cross section to be 2739±251(statistical)$^{+973}_{-831}$(systematic) μb/sr considering background from decay products of K^0, K_{e3} and $K_{\mu 3}$ decays and loss due to π^- cut from $K^-\rightarrow\pi^0\pi^-$.

Let us now calculate the effective neutron number (N_{eff}), which is defined as;

$$\frac{d\sigma}{d\Omega}(\theta) = N_{eff}(\theta)\frac{d\sigma^{free}}{d\Omega}(\theta)$$

where $\frac{d\sigma^{free}}{d\Omega}(\theta)$ is the elementary cross section of K^-n→ $\Lambda\pi^-$ reaction in the free-space at the reaction angle of θ.

The elementary cross sections were taken from the data of Hepp et al.[34]. At $P_K^{lab.}$ = 596 MeV/c, the K^-n →$\Lambda\pi^-$ cross section of the forward angle (cosθ = 0.950 in the center of mass [c.m.] system) is 0.587±0.150 mb/sr in c.m. (in the laboratory system, it is 1.291±0.330 mb/sr). Then the effective neutron number is 2.12±0.58$^{+0.75}_{-0.64}$. Bertini et al. evaluated the effective neutron number from their Λ hypernuclear data at CERN[40]. For $^{9}_{\Lambda}$Be, they obtained 1.5±0.4 at P_K = 720 MeV/c and 1.6±0.5 at P_K = 790 MeV/c, where they used 0.95±0.13 mb/sr(c.m.) as the cross section of the elementary process.

In the (K^-,π) reaction, the effective neutron number becomes less than the actual neutron number in the nucleus because of the meson absorption and can be evaluated by the distorted-wave impulse approximation(DWIA). Boussy calculated the effective neutron number for various nuclei with the shell model(see Ref [42] and references therein). Also Motoba et al. calculated the number for $^{9}_{\Lambda}$Be at P_K = 720 MeV/c with the alpha cluster model[43]. We tabulated the experimental(our data and CERN data) and theoretical results below.

	Exp.			Theory	
	Our data	CERN data		shell model	alpha cluster model
P_K(MeV/c)	586MeV/c	720MeV/c	790MeV/c		720MeV/c
	$N_{eff}(4^0)$	$N_{eff}(0^0)$	$N_{eff}(0^0)$	$N_{eff}(0^0)$	$N_{eff}(0^0)$
	2.12±0.58$^{+0.75}_{-0.64}$	1.5±0.4	1.6±0.4	1.86	2.18

4.4 ^{9}Be(K^-,π^+) data in the Σ region

4.4.1 Excitation energy spectra

The excitation energy spectra of the ^{9}Be(K^-,π^+) reactions (P_π = 438 MeV/c and P_π = 460 MeV/c) are shown in Figures 4.7 and 4.8. Figure 4.7 is raw spectra obtained in this experiment. We applied

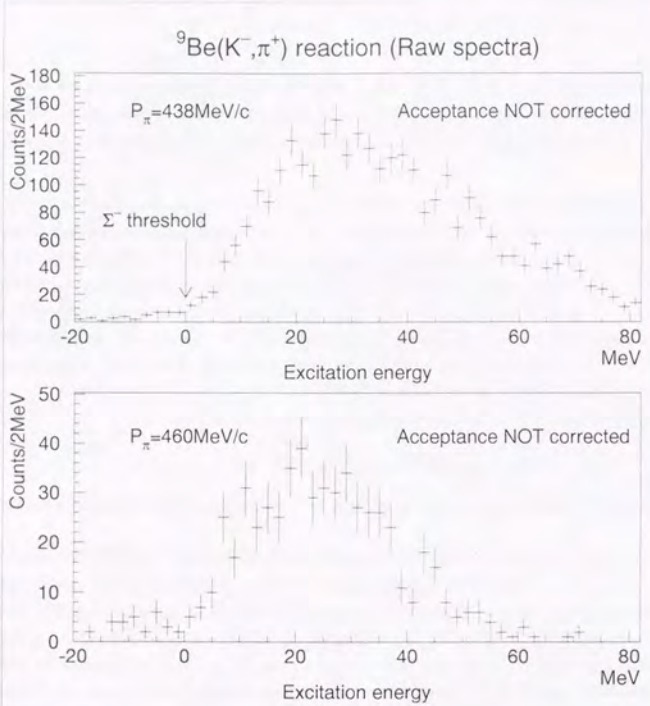

Figure 4.7: Excitation energy (EE) spectra of the ^{9}Be(K^-,π^+) reactions at P_π = 438 MeV/c (upper spectrum) and P_π = 460 MeV/c (lower spectrum). The vertical axis is number of counts per 2 MeV. EE = 0 MeV is the Σ^- production threshold. EE > 0 MeV is the Σ^- unbound region.

correction of the spectrometer momentum acceptance to those spectra and got the spectra shown in Figure 4.8. Also the acceptance curves used are plotted in Figure 4.8. Here, EE (excitation energy) = 0 MeV is taken at the Σ^- production threshold and EE > 0 MeV is the Σ^- unbound region.

4.4.2 Background rejection

As shown in Figure 3.17, the only possible background source is the π^+ from $K^-\to\pi^+\pi^-\pi^-$ for the P_π = 438 MeV/c runs. For the P_π = 460 MeV/c runs, the $K_{\pi 3}$ pions are outside of our acceptance, hence the spectrum should be free of background.

Using the empty target run, we subtracted the decay-pion contamination in the spectrum. The empty target run was analyzed with the same event selection criteria as was applied to the ^{9}Be target run. Then the number of counts in the EE spectrum was converted to the cross section as if there was a target, so that the data is properly normalized to the ^{9}Be target run.

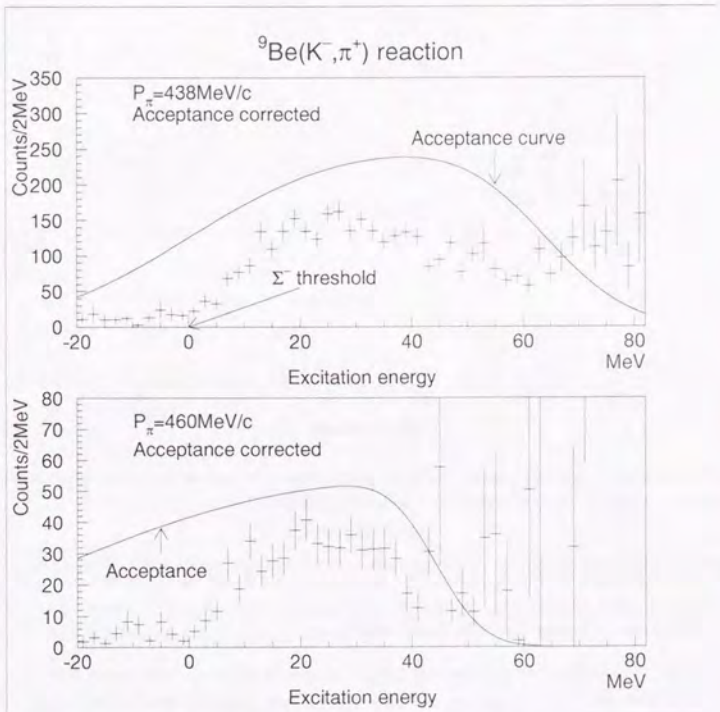

Figure 4.8: Acceptance-corrected spectra of the ^{9}Be(K^-,π^+) reaction as function of excitation energy(EE) at P_π = 438 MeV/c (upper spectrum) and P_π = 460 MeV/c (lower spectrum). The vertical axis is number of counts per 2 MeV. Acceptance curve used is indicated in solid line. EE = 0 MeV is the Σ^- production threshold. EE > 0 MeV is the Σ^- unbound region.

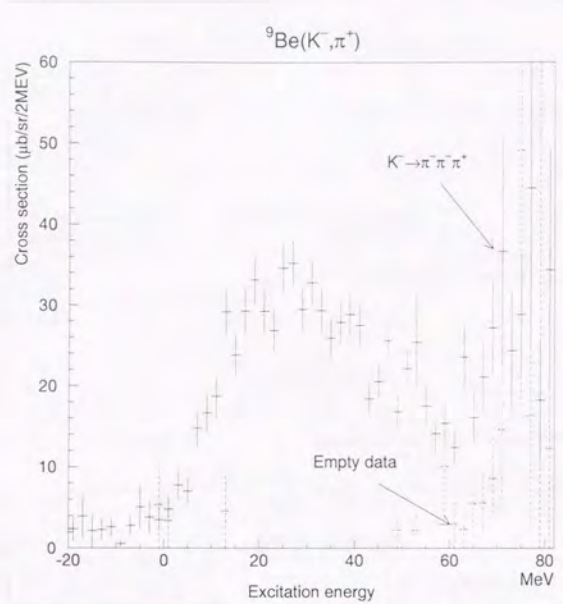

Figure 4.9: ^{9}Be(K^-,π^+) excitation energy (EE) spectrum (solid) overlayed on the empty target spectrum (dotted). EE = 0 MeV is the Σ^- production threshold. P_π = 438 MeV/c

We show in Figure 4.9 the empty-target spectrum superimposed on the ^{9}Be(K^-,π^+) spectrum.

4.4.3 Systematic error for the cross section

As was done for the $^9_\Lambda$Be case, we summarize below the systematic errors of cross section evaluation for the ^{9}Be(K^-,$\pi^\pm$) spectra.

Correction	systematic error
Kaon decay correction	+1%
	−0%
χ^2 cut	+10%
	−0%
Pion decay correction	±5%
Angular acceptance	±10%
Momentum acceptance	±20%
Total	+25%
	−23%

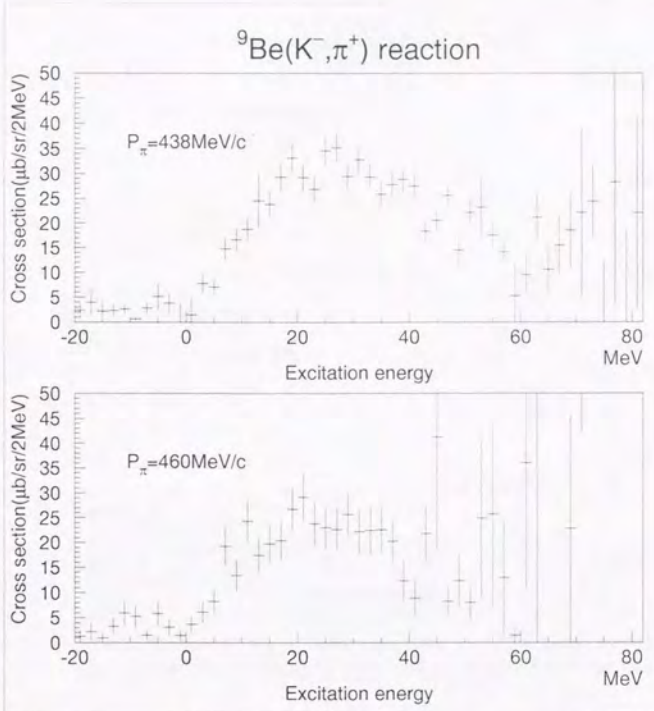

Figure 4.10: Cross section of the ^{9}Be(K^-,π^+) reaction as a function of excitation energy(EE). Upper data was taken at P_π = 438 MeV/c and lower data at P_π = 460 MeV/c. EE = 0 MeV is the Σ^- production threshold. EE > 0 MeV is the Σ^- unbound region.

4.4.4 Cross sections as function of excitation energy

The cross sections as function of excitation energies of both P_π = 438 MeV/c and P_π = 460 MeV/c are shown in Figure 4.10.

The energy-integrated cross section of Σ^- production was derived by summing up the spectra ($P\pi$ = 438 MeV/c) from EE = 0 MeV to EE = 80 MeV. Then we obtained $857\pm39^{+214}_{-197}$ μb/sr. Contribution of background from K^0 decay in this region (0 MeV < EE < 80 MeV) is 116±68 μb/sr. Finally we get $741\pm78^{+214}_{-197}$ μb/sr for the integrated cross section. In order to calculate the effective proton number, we need the elementary cross section of $K^-p\rightarrow\Sigma^-\pi^+$. As for this cross section we used our own result measured with the CH_2 target (see Appendix B). The same analysis procedure was applied to determine the elementary cross section. The effective proton number was deduced as 1.18±0.14, which should be free of systematic errors of cross section evaluation.

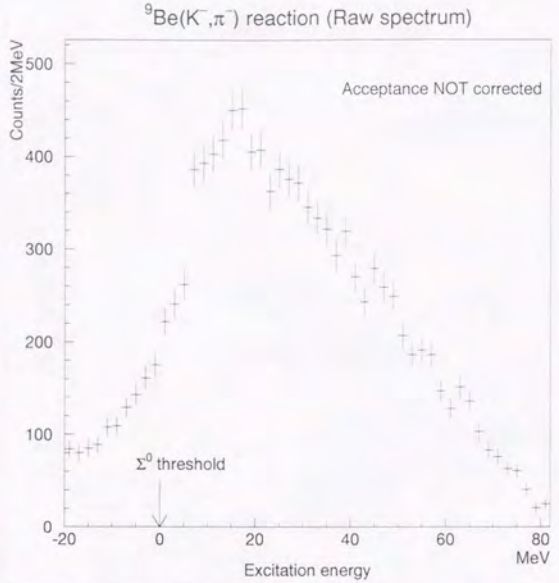

Figure 4.11: Excitation energy (EE) spectrum of the ^{9}Be(K^-,π^-) reaction in the Σ region. The vertical axis is number of counts per 2 MeV. EE = 0 MeV is the Σ^0 production threshold

4.5 ^{9}Be(K^-,π^-) data in the Σ region

4.5.1 Excitation energy spectra

The excitation energy spectra of the ^{9}Be(K^-,π^-) reaction in the Σ region are shown in Figures 4.11 and 4.12. Figure 4.11 is raw spectra obtained in this experiment. We applied correction of the spectrometer momentum acceptance to those spectra and got the spectra shown in Figure 4.12. Also the acceptance curves used are plotted in Figure 4.12. Here, EE (excitation energy) = 0 MeV is taken at the threshold of Σ^0 production, which lies 13.3 MeV below the Σ^+ threshold. EE > 0 MeV corresponds to the Σ^0 unbound region.

4.5.2 Background rejection

Most of the K^- decay background was eliminated by using the analysis procedure described in the previous chapter. However, there still remain some electron and muon backgrounds due to insufficient time of flight resolution and to the muon filter inefficiency. Moreover the decay pions from $K^- \to \pi^-\pi^0\pi^0$ cannot be separated from pions of the hypernuclear events.

Thus we used the empty target run to subtract these remaining backgrounds. As before, the empty

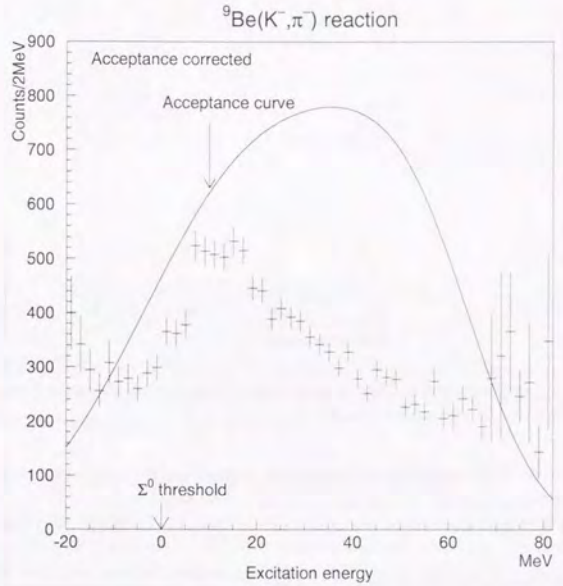

Figure 4.12: Acceptance-corrected spectrum of the ^{9}Be(K^-,π^-) reaction as function of excitation energies(EE). The vertical axis is number of counts per 2 MeV. Acceptance curve used is indicated in solid line. EE = 0 MeV is the Σ^0 production threshold

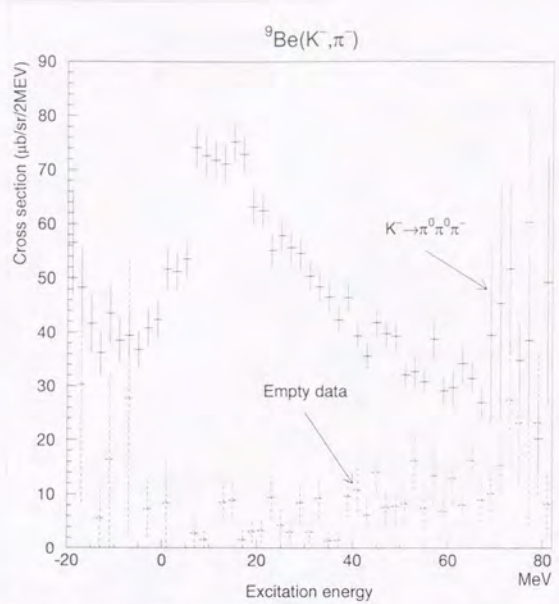

Figure 4.13: ^{9}Be(K^-,π^-) excitation energy (EE) spectrum (solid) overlayed on the empty target spectrum (dotted). EE = 0 MeV is the Σ^0 production threshold

run was analyzed with the same procedure as was applied to the ^{9}Be target run, and the number of counts in the spectrum was converted to the cross section as if there was a target.

We show in Figure 4.13 the empty target spectrum superimposed on the ^{9}Be(K^-,π^-) spectrum.

4.5.3 Systematic error of the cross section

The systematic errors on the cross section are tabulated below.

Correction	systematic error
Kaon decay correction	+1%
	−0%
χ^2 cut	+10%
	−0%
Decay correction	±5%
Angular acceptance	±10%
Momentum acceptance	±20%
Total	+25%
	−23%

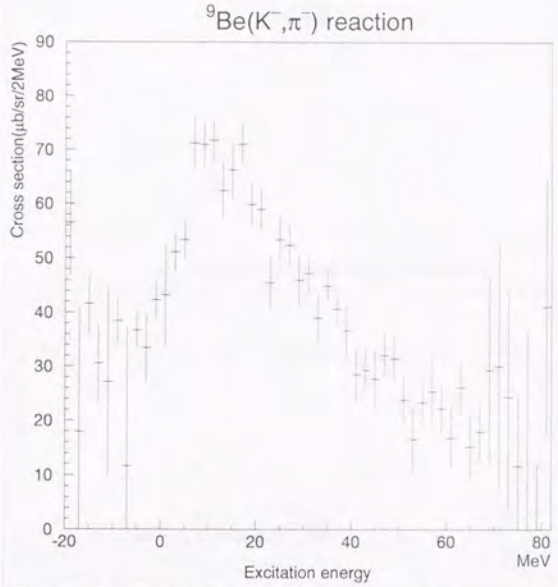

Figure 4.14: Cross section of the ^{9}Be(K^-,π^-) reaction as a function of excitation energy(EE). Data was taken at P_π = 460 MeV/c. EE = 0 MeV is the Σ^0 production threshold. EE >0 MeV is the Σ^0 unbound region. Production threshold of Σ^+ is at EE = 13.3 MeV.

4.5.4 Cross section as function of excitation energy

Figure 4.14 shows the ^{9}Be(K^-,π^-) cross section as a function of excitation energy. The spectrum exhibits a large cross section in the EE < 0 MeV region due mostly to the tail of Λ production continuum. To obtain the energy-integrated cross section of Σ^0 and Σ^+ production, we attempted to subtract this Λ component, by assuming that the Λ tail can be extrapolated into the Σ region as a tail of Gaussian function. The region of the histogram from EE = −35 MeV to EE = −9 MeV was fitted by a Gaussian to evaluate the Λ contribution in the EE > 0 MeV region (see Figure 4.15). We show the Λ-subtracted spectrum in Figure 4.16. Since the subtraction procedure as presented above is purely phenomenological and can involve a large systematic uncertainty, we assign the upper limit of the cross section supposing Λ tail contribution can be described as a linear function (see Figure 4.17).

The energy integrated cross section summing up the spectrum from EE = 0 MeV to EE = 80 MeV was derived as $1273\pm53^{+390}_{-293}$ μb/sr. Contribution of background from K^0 decay in this region (0 MeV < EE < 80 MeV) is 116±68 μb/sr. Thus we get $1157\pm86^{+390}_{-293}$ μb/sr for the integrated cross section.

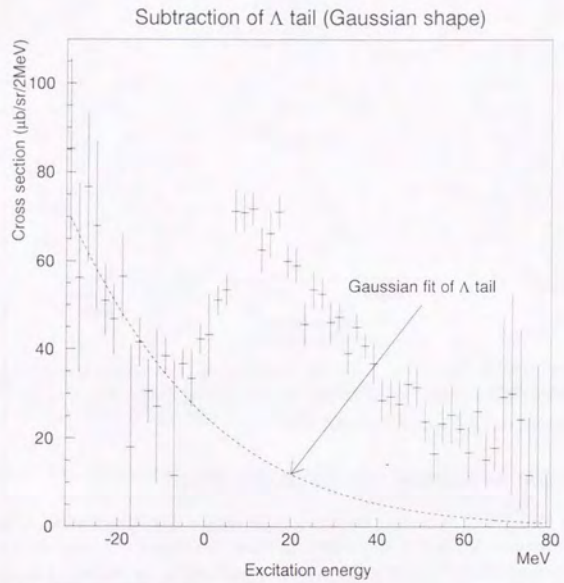

Figure 4.15: ^{9}Be(K^-,π^-) excitation energy (EE) spectrum in the Σ region. Λ continuum tail is assumed to be described as a Gaussian tail. EE = -35 MeV to -9 MeV data was used for fitting. The solid line is the extrapolated line of Λ continuum in the Σ region

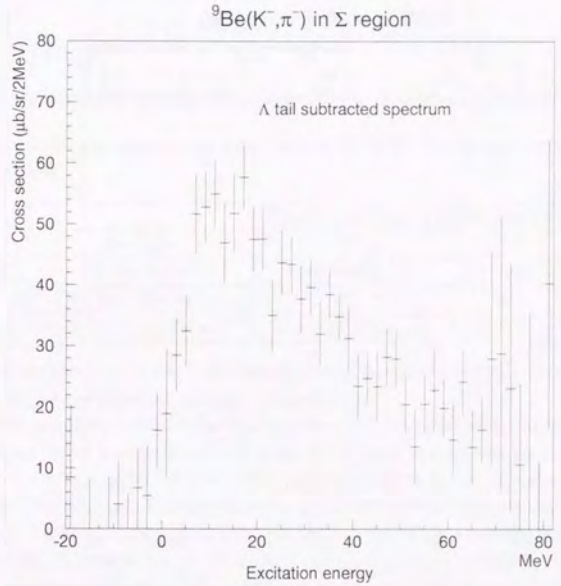

Figure 4.16: ^{9}Be(K^-,π^-) excitation energy (EE) spectrum derived by subtracting the Λ continuum. Λ tail was assumed to be a tail of Gaussian (see Figure 4.15). Vertical and horizontal axis definitions are the same as before.

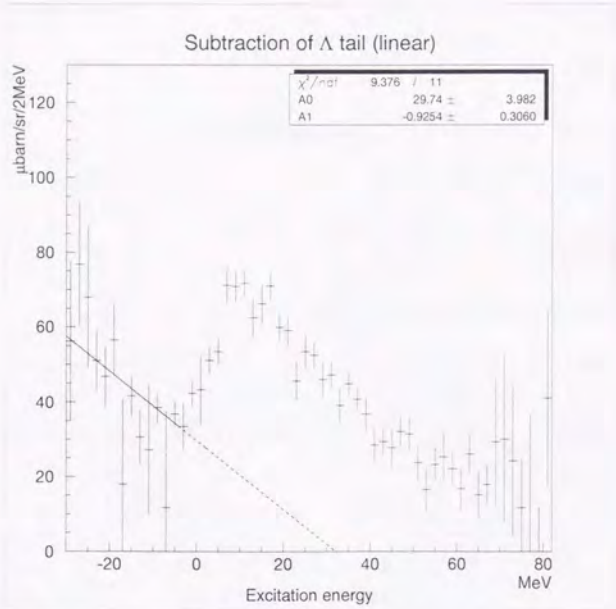

Figure 4.17: ^{9}Be(K^-,π^-) excitation energy (EE) spectrum in the Σ region. Λ continuum tail is assumed to be described as a linear function. EE = -30 MeV to -5 MeV data was used for fitting (solid line). The dashed line is the extrapolated line of Λ continuum in the Σ region

Chapter 5

Discussion

5.1 Comparison with the previous data at CERN

The differences in the experimental conditions between the CERN ^{9}Be experiment[1] and the experiment are tabulated below.

	Present experiment	CERN experiment
Reaction	(K^-,π^-)	(K^-,π^-)
K^- momentum	586 MeV/c	720 MeV/c
π^- detection angle	4°	0°
Momentum transfer to Σ^0	118 MeV/c	129 MeV/c

The momentum transfer is one of the most important factors in order to compare the hypernuclear spectra. We will discuss about the momentum transfer here.

The CERN experiments utilized the spectrometer SPES II to analyze the momenta of pions. This spectrometer can detect pions in the angular acceptance from 0° to 6° and its mean angle is 3 degrees at the forward angle setting[1]. On the other hands, pion scattering angle accepted by our Pion spectrometer placed at 4° is 115 mrad (6.5 °) in mean with 100 mrad (6°) FWHM (see Figure 5.1). Thus the momentum transfers to Σ^0 (at Σ^0 production threshold) for our and the CERN experiments are calculated using those mean angles (6.5° for us and 3° for CERN) and shown in the above table. The difference of the momentum transfer between our and the CERN experiment is 10 MeV/c.

However, the momentum transfer varies as a function of the excitation energy as shown in Figure 5.2 for the present experiment. Thus in order to compare the whole spectrum, we must know this dependence for both our and the CERN experiment. We made simulations assuming gaussian distributions of the incident K^- momentum (see Figure 2.7) and $K\pi$ scattering angle. Parameters used for simulation are tabulated below and results are shown in Figure 5.3 for our experiment and in Figure 5.4 for the CERN experiment. Because we couldn't know the actual scattering angle distribution of the CERN experiment, we assumed it is a gaussian which rises from 0° and takes a maximum at 3°.

	P_K		$\theta_{K\pi}$		
	mean	σ	mean	σ	
Our experiment	586 MeV/c	3 %	6.5°	2.6°	Figure 5.3
CERN	720 MeV/c	3 %	3.0°	1.5°	Figure 5.4

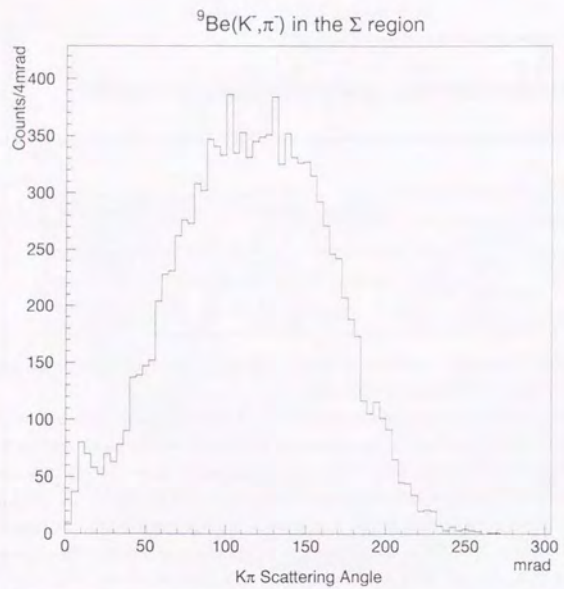

Figure 5.1: $K\pi$ scattering angle distribution of ^{9}Be(K^-,π^-) reaction in the Σ region. Event selections applied are the same as those to derive the spectrum in Figure 4.11.

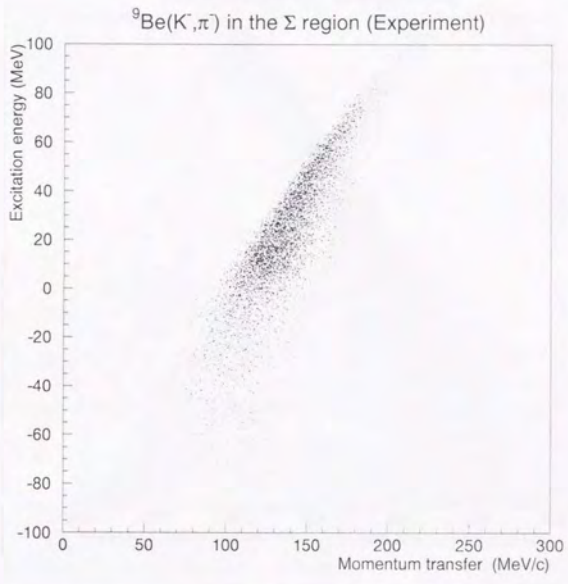

Figure 5.2: Momentum transfer vs. excitation energy of the ^{9}Be(K^-,π^-) reaction (Experimental data). EE = 0 MeV is the Σ^0 production threshold. Spectrometer momentum acceptance is not corrected for.

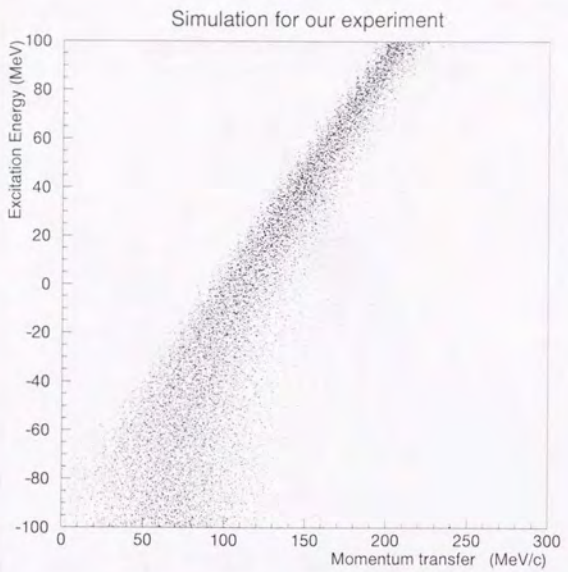

Figure 5.3: Simulated momentum transfer vs. excitation energy of the ^{9}Be(K^-,π^-) reaction for our experiment. EE = 0 MeV is the Σ^0 production threshold. Gaussian distributions for incident K^- momentum (mean = 586 MeV/c, σ = 3%) and $K\pi$ scattering angle (mean = 6.5°, σ = 2.6°) were used. Momentum acceptance of Pion spectrometer was not assumed

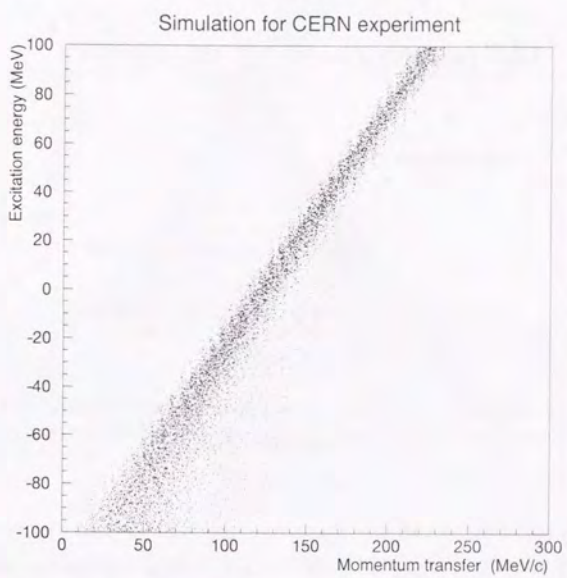

Figure 5.4: Simulated momentum transfer vs. excitation energy of the ^{9}Be(K^-,π^-) reaction for CERN experiment. EE = 0 MeV is the Σ^0 production threshold. Gaussian distributions for incident K^- momentum (mean = 720 MeV/c, σ = 3%) and $K\pi$ scattering angle (mean = 3.0°, σ = 1.5°) were used. Momentum acceptance of Pion spectrometer was not assumed

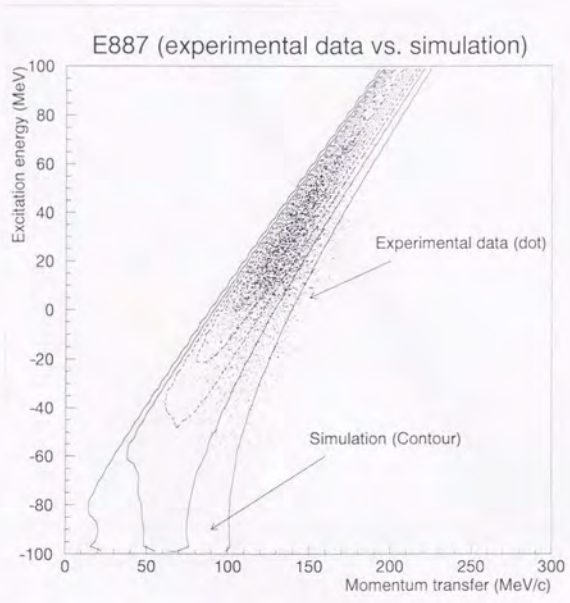

Figure 5.5: Momentum transfer vs. excitation energy plot. Simulated results for our experiment (contour plot) is superimposed on the experimental data (dot). EE = 0 MeV is the Σ^0 production threshold.

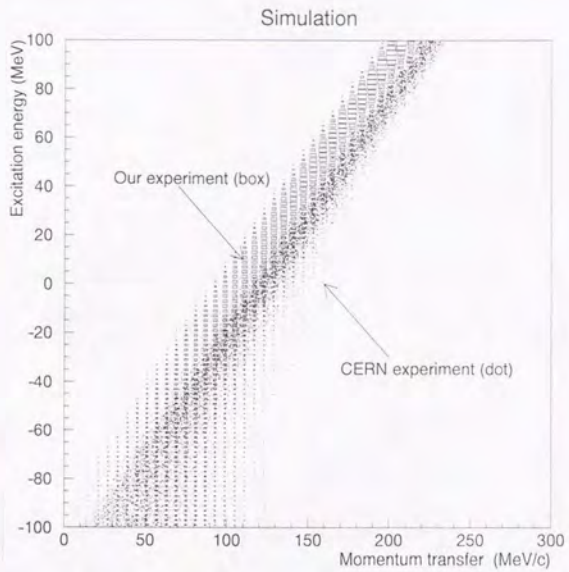

Figure 5.6: Comparison of the simulated momentum transfer vs. excitation energy between ours and CERN's. EE = 0 MeV is the Σ^0 production threshold. Boxed plot is for our experiment and dotted plot for CERN.

Simulation for our experimental setting reproduces the experimental results (see Figure 5.5).

Comparing the simulated results (Figure 5.6), we can see that the momentum transfer for our experimental setting is 10∼15 MeV/c smaller than that of CERN's in the whole range of the excitation energy.

In the region of the excitation energy where we are interested in, i.e. from EE = 0 MeV to EE = 40 MeV, the momentum transfer is thus around 100 MeV/c. If shape of the excitation energy spectrum in this region comes from the quasifree production of Σ, 15 MeV/c difference in the momentum transfers between both experiments is too small to exhibit a significant difference in the shapes because this value is adequately smaller than the nuclear fermi momentum. On the other hands, if narrow structures in the CERN spectrum are substitutional states such as the excited states of ${}^{9}_{\Lambda}$Be, in our experiment those states must be enhanced and never suppressed because of smaller momentum transfer. Thus it is meaningful to compare our spectrum to CERN's directly.

In Figure 5.7, we re-plot the CERN ^{9}Be Σ hypernuclear data, superimposed on our present result with an arbitrary normalization. The horizontal scale of the CERN data was shifted by -254.7 MeV to convert the hypernuclear mass to the excitation energy scale.

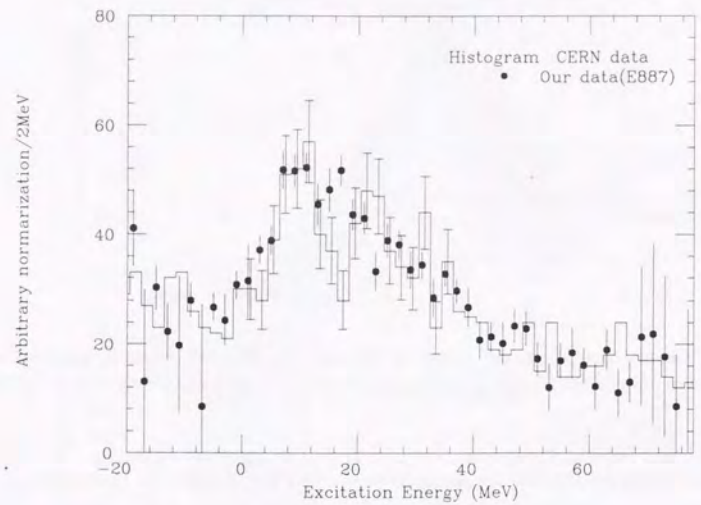

Figure 5.7: Comparison of our (K^-,π^-) data (closed circle) with the CERN data (histogram). Vertical axis is arbitrarily normalized. Horizontal axis is the excitation energy. EE = 0 MeV is the Σ^0 production threshold.

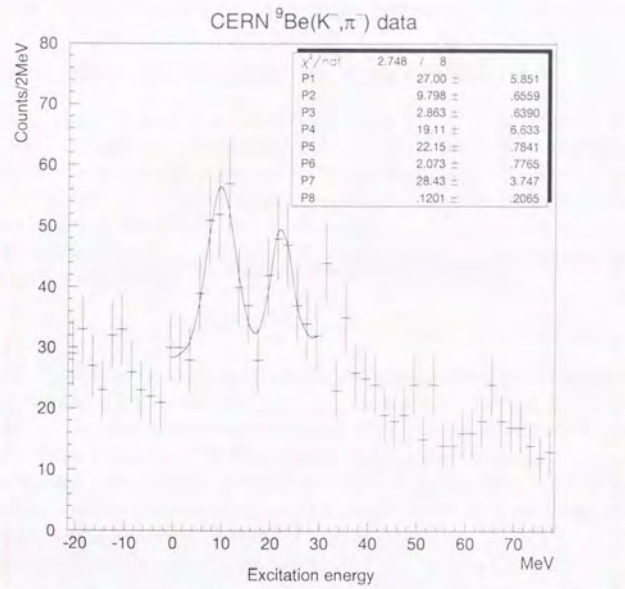

Figure 5.8: 2 Gaussians and linear background fit of CERN narrow peaks in the region of EE = 0 MeV to 10 MeV.

Our data agree with the CERN data remarkably well from EE = −20 MeV to EE = 80 MeV except for the dip around EE = 17 MeV in the CERN data. Note that our data have about ten times higher statistics than that of the CERN data, and that our energy resolution (FWHM = 4.2 MeV) should be adequate to resolve narrow ($\Gamma \sim 8$ MeV) structures if there is any.

To see how the spectra obtained at CERN is changed with our energy resolution if two narrow peaks exist, we fitted the CERN data with 2-Gaussians and linear background in the region of EE = 0 to 30 MeV (Figure 5.8). Then in Figure 5.9, obtained two peaks are convoluted with 4.2 MeV resolution assuming 3 MeV resolution for the CERN data. The two peaks should be clearly seen with our energy resolution if the narrow peaks are real.

Considering discussion of the differences in the experimental setting, we can thus conclude that there are no two narrow peaks, but there exists only a broad bump, in the region of the suggested Σ hypernuclear states.

5.2 ^{9}Be(K^-,π^+) data

The ^{9}Be(K^-,π^+) spectra (both in Figure 4.10) show no obvious structure neither in the bound nor in the unbound region. Since there is not much strength in the bound region, we may qualitatively conclude that

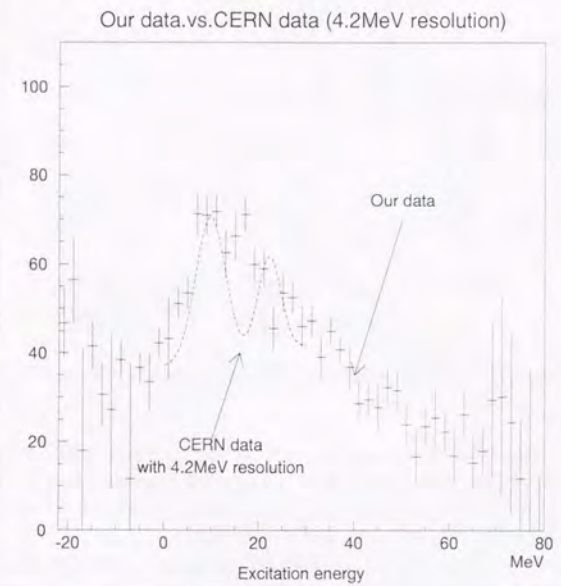

Figure 5.9: Convoluted CERN two peaks with our energy resolution (4.2 MeV) [dotted line] superimposed on our ^{9}Be(K^-,π^-) data. Our data has no indication of narrow peaks.

there is no strongly-attractive Σ−nucleus potential for this system. In order to quantify this conclusion, however, a detailed DWIA calculation of the π^+ spectrum is needed, and is strongly awaited.

5.3 Comparison with a quasi-free picture

As shown above, no apparent structure was found in either of the ^{9}Be(K^-,π^-) and ^{9}Be(K^-,π^+) excitation energy spectra in the Σ region. Let us see if the observed continuous spectra are compatible with a simple quasi-free picture. Chrien et al.[44] emphasized the importance of proper calculation of the quasi-free continuum spectrum and they found that the simple quasi-free picture describes the previously reported Σ hypernuclear spectra on ^{12}C, ^{16}O, ^{6}Li and ^{7}Li remarkably.

Here we adopted the quasi-free model introduced by Gal([23][45]), in which the quasi-free shape can be expressed in the following form,

$$f(T_\Sigma) = \frac{p m_\Sigma}{2\pi^2} \int |\psi(\boldsymbol{q}-\boldsymbol{p})|^2 \frac{d\Omega_p}{4\pi},$$

where T_Σ is the Σ kinetic energy, m_Σ is the Σ mass, $\boldsymbol{p}$ is the Σ momentum, $\boldsymbol{q}$ is the momentum transfer and ψ is the momentum-space wave function of the struck nucleon. The assumptions used to derive this form are, i) K^-, π and Σ are described by plain waves, ii) Momentum dependence of the elementary cross section(KN→$\Sigma\pi$) is small, iii) Momentum transfer to hyperons is constant.

The wave function is normalized as $\int |\psi(p)|^2 d\boldsymbol{p}/(2\pi)^3 = 1$ so that get $\int_0^\infty f(T_\Sigma) dT_\Sigma = 1$. If a harmonic oscillator wave function with an oscillator parameter $\boldsymbol{b}$ is used for ψ, the above distribution can be expressed in an analytical form as follows;

When a Σ is produced on a nucleon in the s shell,

$$f(T_\Sigma) = \frac{m_\Sigma b}{\pi^{1/2} q} [e^{-b^2(p-q)^2} - e^{-b^2(p+q)^2}],$$

While when a Σ is produced on a nucleon in the p shell.

$$f(T_\Sigma) = \frac{2 m_\Sigma b}{3\pi^{1/2} q} [(1+b^2(p-q)^2) e^{-b^2(p-q)^2} - (1+b^2(p+q)^2) e^{-b^2(p+q)^2}].$$

This model has 3 parameters, which are the harmonic oscillator parameter $\boldsymbol{b}$, energy separation and spectroscopic factor of each state in the residual nucleus. The $\boldsymbol{b}$ parameter represents momentum distributions of nucleons in the target nucleus. The energy separation determines the hyperon quasi-free production threshold from each state. The spectroscopic factor is the effective number of nucleons which participate in the quasi-free reaction.

We will use these quasi-free shapes, and compare them with the observed spectra. To demonstrate Gal's quasi-free formalism, we calculated the quasi-free spectra of previously reported Σ hypernuclear data obtained at BNL[11] (Figure 5.10) and CERN[9][10] (Figure 5.11). As seen from Figures 5.10 and 5.11, these quasi-free shapes adequately describe Σ hypernuclear spectra.

These expressions give essentially the same results as done by Chrien et al.[44] (their calculation includes full momentum dependence of N(K^-,π)Σ).

5.3.1 (K^-,π^+) reaction on ^{9}Be

In this reaction, a Σ^- is produced on one of the four protons in ^{9}Be. In the shell-model picture, two of the protons are in the $p_{3/2}$ state and the other two are in the $s_{1/2}$ state. For the b parameter, we took b =

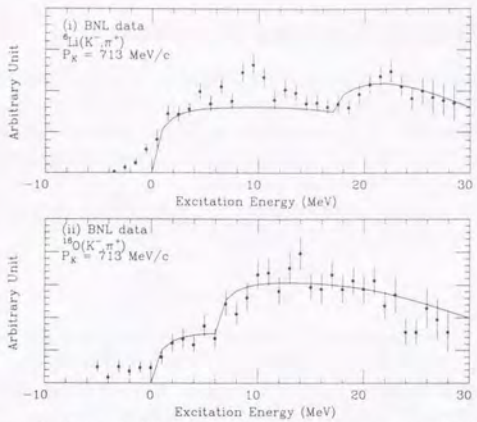

Figure 5.10: Quasi-free calculation (solid line) described in the text, on (i) ^{6}Li(K^-,π^+) and (ii) ^{16}O(K^-,π^+) data obtained at BNL(Ref.[11]). Experimental energy resolution is not included. EE = 0 MeV represents Σ^- production thresholds. Vertical scale is arbitrarily normalized

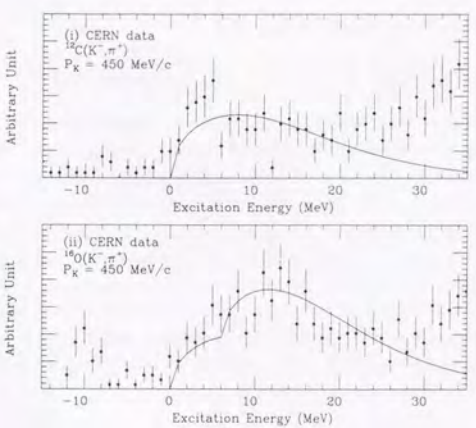

Figure 5.11: Quasi-free calculation (solid line) described in the text, on (i) ^{12}C(K^-,π^+) and (ii) ^{16}O(K^-,π^+) data obtained at CERN(Refs.[9] and [10]). Experimental energy resolution is not included. EE = 0 MeV represents Σ^- production thresholds. Vertical scale is arbitrarily normalized

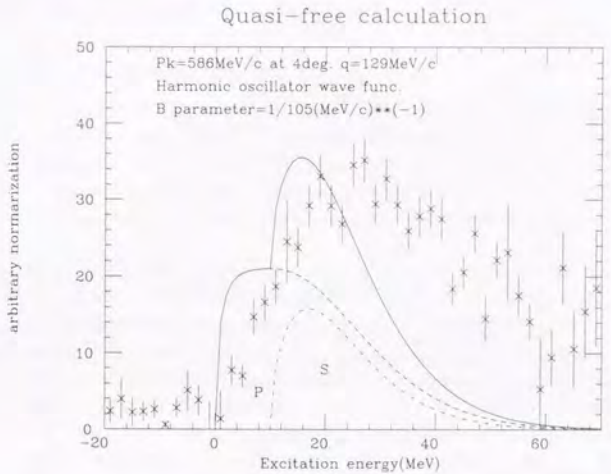

Figure 5.12: Calculated excitation energy spectrum (solid line) of the ^{9}Be(K^-,π^+) reaction with quasi-free assumption (on details, see text) superimposed on our data. $b = 1/105$ (MeV/c)$^{-1}$ and the spectroscopic factor ratio of s- to p-state proton is taken to be 1:2. Vertical normalization is arbitrary.

1/105 (MeV/c)$^{-1}$, derived from the ^{12}C(e, e'p)^{11}B experiment[46] and this value is known to reproduce proton momentum distribution in ^{12}C. As the binding energy difference between s and p states, we used 10MeV. This value was taken from the ^{9}Be(p, 2p)^{8}Li pickup experiment[47][50][51]. The ^{9}Be(e, e'p)^{8}Li experiment[53][54] showed the participant number (spectroscopic factor) of protons in $s_{1/2}$ and $p_{3/2}$ are 0.74±0.04 and 1.40±0.05, respectively. Thus we take the ratio of the reaction participant protons in $s_{1/2}$ and $p_{3/2}$ as 1:2

The calculated result is compared with arbitrary normalization to our data.

As shown in Figure 5.12, the quasi-free model does not reproduce the data at all. The observed spectrum at the Σ threshold is less steep, and there is a significant difference in shape at higher excitation region. Our data is not reproduced even if we change the ratio of s and p contributions, because our spectrum peaks around EE = 20 MeV. The calculated spectrum cannot have a maximum at such a high excitation energy.

A better agreement may be obtained by changing the b parameter. For example, Figure 5.13 shows the case with $b = 1/120$ (MeV/c)$^{-1}$, with the same s to p ratio of 1:2. Although the threshold rise can be made less steep, the model cannot represent the data either.

The agreement would be better if we used smaller b parameter. However, such small b parameter values are unrealistic since the momentum distribution of p-hole state measured in the ^{9}Be(e, e'p)^{8}Li experiment[53] indicates that the b parameter can never be smaller than 1/105 (MeV/c)$^{-1}$.

Therefore, we conclude that the quasi-free model cannot reproduce the observed spectrum. The

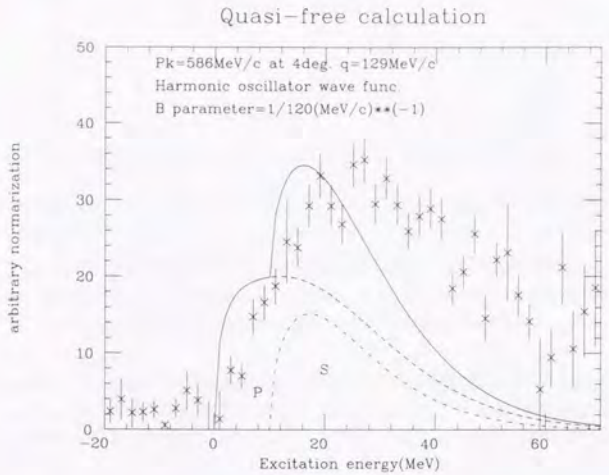

Figure 5.13: Calculated excitation energy spectrum (solid line) of the ^{9}Be(K^-,π^+) reaction with quasi-free assumption (on details, see text) superimposed on our data. $b = 1/120$ (MeV/c)$^{-1}$ and the spectroscopic factor ratio of s- to p-state proton is taken to be 1:2. Vertical normalization is arbitrary.

difference in the threshold behavior, i.e., the slow rise of the cross section as a function of the excitation energy, may be an indication that the Σ^-−nucleus potential is repulsive for this system.

5.3.2 (K^-,π^-) reaction on ^{9}Be

Since the Fermi-averaged Σ^+ production cross section is about 7 times smaller as compared to the Σ^0 cross section at P_K = 600 MeV/c (see Figure 2.2), we assume that the continuum is composed of quasi-free Σ^0 production on one of the five neutrons in ^{9}Be. In the shell-model language, there are three neutrons in the $p_{3/2}$ state, and two in the $s_{1/2}$ state. Alternatively in the cluster-model picture, ^{9}Be consists of 2 α clusters plus a neutron, hence there are four neutrons in the two α clusters, and one p−state neutron outside.

The spectroscopic factors were measured in the ^{9}Be(p, d)^{8}Be experiment[48][49], which found two dominant peaks, separated by about 16 MeV, with an intensity ratio of I(most loosely bound) : I(18 MeV excitation) $\sim$ 1 : 2. It is also known that there are $s_{1/2}$ hole strength at 27 MeV above the most loosely bound neutron[50][51]. In our quasi-free model, we included the $s_{1/2}$ neutron hole strength with the same intensity as the loosely bound neutron, assuming the spectroscopic factor ratio in α cluster is the same as that of protons in the cluster (as described before, the spectroscopic factor ratio of $s_{1/2}$ and $p_{3/2}$ is 1 : 2). Thus we took the spectroscopic factor rate of the neutron hole states as s(27 MeV excitation) : p(18 MeV excitation) : p(loosely bound) = 1 : 2 : 1. The b parameter was taken to be 1/105 (MeV/c)$^{-1}$. The result is shown in Figure 5.14, compared with our data (with Λ tail subtraction). As shown, the model cannot reproduce the observed spectrum; in particular, there is a large deficit around EE = 10 MeV.

If the spectroscopic factors of the most loosely bound neutron could be arbitrarily made large, the calculated shape would be similar to the observed spectrum. However, as noted above, the (p,d) neutron pickup experiment shows that the neutron hole intensity ratio of p(loosely bound) : p(18MeV excitation) is $\sim$ 1 : 2.

In addition, we know that the two dominant peaks of $^9_\Lambda$Be at EE = 6 MeV and EE = 17 MeV are the substitutional state on the loosely bound $p_{3/2}$ neutron and neutron in the alpha cluster respectively, and the strength is larger by about a factor 2 for the 17 MeV peak. This also suggests that the contribution of the most loosely bound neutron cannot be made arbitrarily large.

Thus, clearly, the quasi-free picture cannot be a good representation of our data, and more theoretical studies are needed to understand the ^{9}Be(K^-,$\pi^\pm$) spectra in the Σ region.

5.3.3 Conclusion from quasi-free picture

It is interesting that the (K^-,π^-) and the (K^-,π^+) reaction on ^{9}Be seem to imply the opposite tendency in Σ-nucleus interaction. In the (K^-,π^-) case, it is rather attractive, while in the (K^-,π^+) case, it may be repulsive. The similar tendency can be seen in the ^{4}He Σ hypernucleus[16][19]. The bound state of $^4_\Sigma$He was found in the (K^-,π^-) reaction, while no structure in the (K^-,π^+) case. This is interpreted as the effect of isospin term (Lane term) in the Σ-nuclues potential[17]. In the ^{4}He(K^-,π^+) case, only T=3/2 state can be populated, though the ^{4}He(K^-,π^-) reaction can populate both T=1/2 and T=3/2 states. The microscopic four-body calculation made by Harada et al. showed Σ-nuclues potential is attractive in T=1/2 and repulsive in T=3/2 due to the strong isospin dependence. A light system such as ^{4}He is not isospin-saturated and those tendencies are obviously seen. The same thing may be true for the ^{9}Be(K^-,$\pi^\pm$) reaction due to the α-clustering nature of ^{9}Be. More theoretical study should be needed

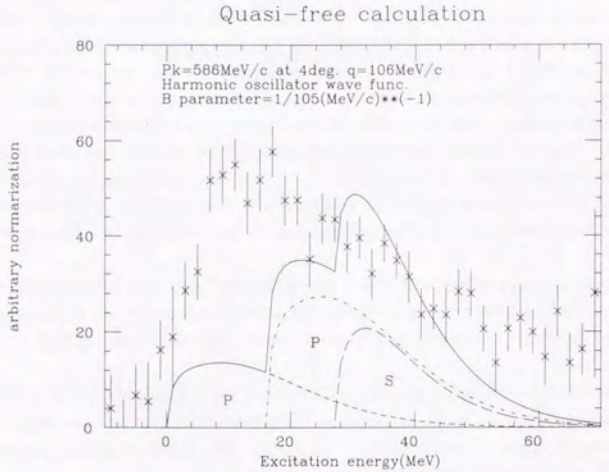

Figure 5.14: Calculated excitation energy spectrum (solid line) of the ^{9}Be(K^-,π^-) reaction with quasi-free assumption (on details, see text) superimposed on our data. $b = 1/105$ (MeV/c)$^{-1}$ and the spectroscopic factor ratio s:p(18 MeV excitation):p(loosely bound)=1:2:1. Vertical normalization is arbitrary.

for this issue.

Chapter 6

Summary

We performed ^{9}Be(K^-,$\pi^\pm$) experiments to study Σ hypernuclei using the two focusing type spectrometers at AGS of BNL. 5×10^9 kaons for the (K^-,π^-) reaction and 4×10^9 kaons for the (K^-,π^+) reaction were incident on ^{9}Be target. Especially in the ^{9}Be(K^-,π^-) reaction, we collected 10 times higher statistics than the previous CERN experiment. We also obtained the decay background-free unbiased spectrum for the first time in the Σ hypernuclear experiment with in-flight (K^-,π^-) reaction.

In particular, the present (K^-,π^-) spectrum shows a clear evidence that there are no narrow $^9_\Sigma$Be peaks as reported previously by an experiment performed at CERN[1]. Instead, the spectrum is a rather structureless continuum. Differences of our experimental setting and CERN's were examined in detail and we conclude that there are no narrow Σ hypernuclei on ^{9}Be.

The shape of the continuum, however, cannot be explained by a simple quasi-free model, and more theoretical works are needed to better understand the observed data.

The ^{9}Be(K^-,π^+) spectrum showed no structure either. Comparison of the observed spectrum with the quasi-free model indicates that $\Sigma-$nucleus interaction in this case may be repulsive. Here again, more theoretical studies are needed in order to quantify this conclusion.

In this experiment, the most promising narrow Σ hypernuclear structures disappeared.

Summarizing, we believe that the present high-statistics data should provide a sound basis for further theoretical studies of Σ hypernuclei.

Acknowledgements

This thesis results from cooperation of many people who contributed in various way.

Especially Professor R.S. Hayano has been an inexhaustible source of knowledge and ideas for me. It is my greatest fortune to meet him in my life of studying physics.

I would like to express my greatest gratitude to Dr. T. Nagae for his frequent and valuable advise throughout the analysis of the data. I am thankful to Dr. R. Sawafta, of BNL, and Dr. K. Hicks, of Ohio, for giving me a chance to participate the good experiment, as well as the many fruitful discussions. I would also be grateful to Dr. R.E. Chrien, of BNL, for helpful advise. I would thank Professor T. Fukuda, Dr. H. Tamura and Mr. H. Outa for showing me the interest of hypernuclear physics. It is my pleasure to have the experiment with Dr. K. Omata and Mr. W. Naing. Also without the other BNL E887 collaborators' great efforts, this experiment would not succeed. In particular, I would like to express my best regards to Dr. S. Bart for preparing the excellent data reduction and analysis programs. It is also through the excellent jobs by all of the crew at BNL AGS that I have good experimental results.

It is my great pleasure to express my thanks to Professor M. Ishihara, Professor H. Sakai, Dr. T. Ishikawa, Dr. M. Iwasaki, Dr. H. Okamura and Dr. H. Sakurai for guiding and encouraging me to study physics. I am also grateful to everyone in the nuclear experiment group of University of Tokyo.

Appendix A

Transport Matrices

The transport matrix was calculated by TRANSPORT program[55] with the measured magnetic fields and aperture dimensions of all the magnets. The resultant matrix elements are shown in Table A.1 and Table A.2.

Coefficients	Kaon spectrometer	Pion spectrometer
X'/X	-1.28800	-1.00000
X'/θ	-0.02188	0.00000
X'/(δP/P)	1.42000	-2.61400
X'/X*X	-4.529E-02	6.830E-02
X'/X*θ	-6.868E-03	1.801E-02
X'/θ*θ	-2.583E-04	1.202E-03
X'/Y*Y	-9.735E-02	-3.505E-02
X'/Y*ϕ	1.201E-02	1.047E-03
X'/ϕ*ϕ	-3.730E-04	9.539E-06
X'/X*(δP/P)	9.684E-02	1.556E-01
X'/θ*(δP/P)	8.163E-03	2.049E-02
X'/(δP/P)*(δP/P)	-1.780E-02	2.379E-02
θ'/X	-25.42000	-14.98000
θ'/θ	-1.20800	-1.00000
θ'/(δP/P)	17.36000	-19.59000
θ'/X*X	-4.409E-01	4.995E-01
θ'/X*θ	-6.552E-02	1.333E-01
θ'/θ*θ	-2.432E-03	9.007E-03
θ'/Y*Y	-1.008E+00	-3.638E-01
θ'/Y*ϕ	1.241E-01	5.984E-03
θ'/ϕ*ϕ	-3.866E-03	7.148E-05
θ'/X*(δP/P)	1.165E+00	1.19600
θ'/θ*(δP/P)	9.004E-02	1.514E-01
θ'/(δP/P)*(δP/P)	-2.779E-01	2.381E-01
θ' Offset		1.7

Table A.1: 2nd order transport matrices for kaon and pion spectrometer. X', Y', θ' and ϕ' are measured values at front focus. X, Y, θ and ϕ are at rear focus. L is path length. X, Y, Z, L are measured in cm, θ=dX/dZ and ϕ=dY/dZ in mrad and δP/P in %

Coefficients	Kaon spectrometer	Pion spectrometer
Y'/Y	0.14090	1.00000
Y'/ϕ	-0.05710	0.00000
Y'/X*Y	1.138E-01	-9.652E-03
Y'/θ*Y	9.254E-03	-1.040E-03
Y'/X*ϕ	-7.045E-03	-1.429E-04
Y'/θ*ϕ	-5.709E-04	-1.908E-05
Y'/Y*(δP/P)	-1.258E-01	-1.329E-01
Y'/ϕ*(δP/P)	7.193E-03	-2.394E-3
Y' Offset		0.19
ϕ'/Y	22.28000	109.00000
ϕ'/ϕ	-1.93400	1.00000
ϕ'/X*Y	1.304E+00	-1.38000
ϕ'/θ*Y	1.067E-01	-1.842E-01
ϕ'/X*ϕ	-8.092E-02	-5.925E-03
ϕ'/θ*ϕ	-6.509E-03	-1.039E-03
ϕ'/Y*(δP/P)	-1.611E+00	-2.17500
ϕ'/ϕ*(δP/P)	6.408E-02	-1.280E-01
ϕ' Offset		-3.9
L'/X		1.95900
L'/θ		0.26140
L'/L		1.00000
L'/(δP/P)		-0.06356
L'/X*X		-3.509E-02
L'/X*θ		-8.003E-03
L'/θ*θ		-1.024E-03
L'/Y*Y		-6.261E-01
L'/Y*ϕ		-1.209E-02
L'/ϕ*ϕ		-1.196E-04
L'/X*(δP/P)		-3.147E-02
L'/θ*(δP/P)		-1.586E-03
L'/(δP/P)*(δP/P)		-1.700E-02

Table A.2: 2nd order transport matrices for kaon and pion spectrometer. (continues)

Appendix B

CH_2 data analysis and spectrometer energy resolution

Energy resolution and absolute momentum calibration of the Pion spectrometer were examined with a monochromatic pion from the reaction p(K^-,π^-)Σ^+ on a CH_2 target. The excitation energy spectrum is shown in Figure B.1, where the energy scale is defined so that the Σ^+ peak is at EE = 0 MeV. A small background around the Σ peak is due to quasi-free Σ^- production of ^{12}C in CH_2. The overall spectrometer energy resolution was derived to be 4.2 MeV FWHM, and the momentum uncertainty was less than 1 MeV. As described in Appendix D, K^-'s or π's momentum loss in CH_2 target and ^{9}Be target are the same. Consequently, energy resolution of the spectrometer with ^{9}Be target should be 4.2 MeV FWHM.

The differential cross section of Σ^- production was calculated to be 627±37 μb/sr. The uncertainty due to the background subtraction of the quasifree Σ^- from carbon is about 10%. The forward angle Σ^- production cross section measured in a bubble chamber experiment[28] is 0.28±0.05 mb/sr in the center of mass system at P_K = 597 MeV/c. In the laboratory frame, it is 0.62±0.11 mb/sr. The agreement with our experiment is quite satisfactory.

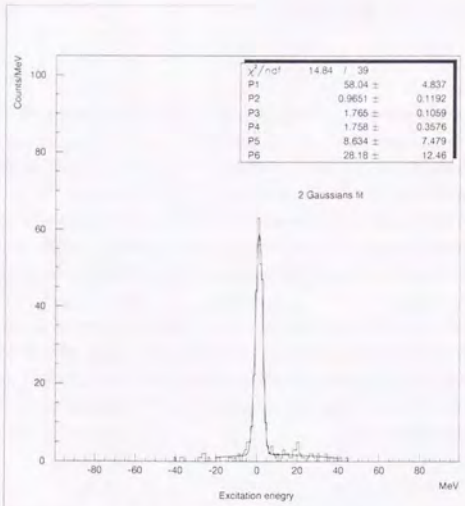

Figure B.1: Energy resolution of the whole spectrometer system derived by monochromatic peak from the p(K^-,π^+)Σ^- reaction. EE = 0 MeV corresponds to the Σ^- production. Target is CH_2

Appendix C

Angular and momentum acceptance of the Pion spectrometer

C.1 Angular acceptance

Because of the widely spread kaon beam in the X direction, dX/dZ of the accepted events show dependence on X. Hence, before evaluating the the angular acceptance of the Pion spectrometer, we corrected the dX/dZ distribution for the X dependence. The corrected histograms are shown in Figure C.1.

From the dX/dZ vs. dY/dZ distributions, we evaluated the angular acceptance as follows. If we approximate the observed profile by a square (sharp cut off) distribution (this would give an upper limit), the angular acceptance = 60 mrad (dX/dZ) × 340 mrad (dY/dZ) = 20 msr.

If we approximate the observed profile by an ellipse (this would give a lower limit), the angular acceptance = 30 mrad (dX/dZ) × 170 mrad (dY/dZ) $\times\pi$ = 16 msr.

Taking the average of the two estimates, we obtained 18 msr for the angular acceptance of the Pion spectrometer.

C.2 Momentum acceptance

The momentum acceptance of the Pion spectrometer, shown in Figure C.2, was determined by using the measured momentum distribution of K_{e3} decay events in the ^{9}Be(K^-,π^-) P_π = 460 MeV/c run. To do so, we imposed a severe cut on the ST−SR TOF spectrum. This method should be reliable, since the momentum distribution of the K_{e3} electrons is known to be flat in this momentum range. The measured electron spectrum was then parameterized with the normal frequency function **freq**[56]. **freq** is composed by the error functions (**erf** and **erfc**[57]) as follows,

$$\mathbf{freq}(x) = \begin{cases} \frac{1}{2} + \frac{1}{2}\mathbf{erf}(x/\sqrt{2}) & (x \geq 0), \\ \frac{1}{2}\mathbf{erfc}(|x|/\sqrt{2}) & (x < 0). \end{cases}$$

The parameterized acceptance as a function of $\delta P/P(\%)$ is

$$\mathbf{freq}\left(\frac{\delta P/P + 7.5}{1.5}\right) \times \left(1 - \mathbf{freq}\left(\frac{\delta P/P - 7.0}{3.3}\right)\right).$$

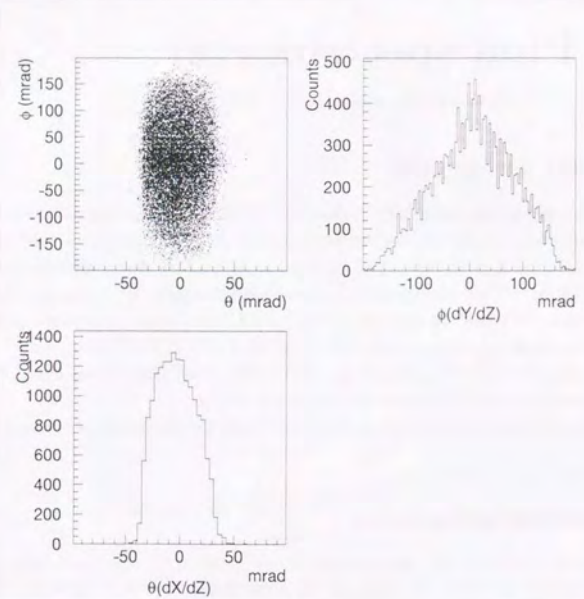

Figure C.1: Angular distributions of emitted particles accepted by the Pion spectrometer. θ = dX/dZ (mrad). ϕ = dY/dZ (mrad)

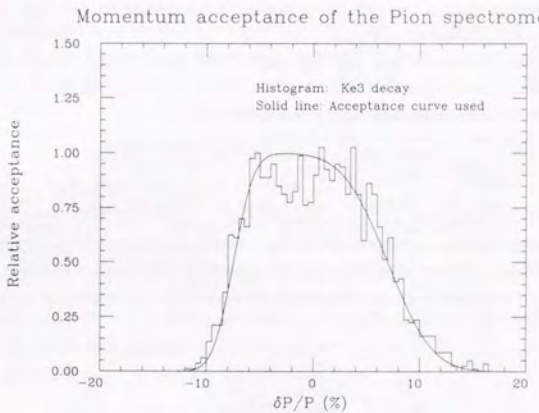

Figure C.2: Momentum acceptance($\delta P/P(\%)$) of the Pion spectrometer. Determined by the accepted K_{e3} decay events (histogram). Solid line is the parameterized acceptance by the normal frequency functions.

Appendix D

Momentum loss correction

The momentum difference in kaon and pion spectrometer on the empty, ^{9}Be and CH_2 targets derived from straight through runs are shown in Figure D.1 ~ D.3.

The momentum loss histograms have the tails around the narrow components. These tails and the central components are well fitted with 2-Gaussians and we used the mean values of the central components as for the mean momentum losses as tabulated below;

	Empty(MeV/c)	^{9}Be(MeV/c)	CH_2(MeV/c)
PIPI	6.19±0.05	10.88±0.16	10.86±0.07
KK	10.92±0.08	19.28±0.05	19.39±0.06

From the mean momentum losses derived above, we can get the target-related momentum losses of kaons or pions in the target by subtracting the empty target data. The result is shown in Table D.1.

To estimate the non target-related momentum loss and the systematic momentum error, the following model is adopted.

$$\begin{aligned} d\pi + S &= C\pi \\ dK + S &= CK \\ dK &= R \times d\pi \end{aligned}$$

where $d\pi$ or dK is non target related pion or kaon momentum loss , S is the systematic momentum error, $C\pi$ or CK the apparent momentum loss of pion or kaon without target and R is the ratio of kaon to pion momentum loss.

R can be calculated from ^{9}Be or CH_2 data in Table D.1 and the results are R = 1.81±0.07 for ^{9}Be, 1.79±0.04 for CH_2. Taking its average, R = 1.80±0.04 was chosen.

	π(MeV/c)	K(MeV/c)
^{9}Be	4.69±0.16	8.48±0.10
CH_2	4.67±0.09	8.37±0.09

Table D.1: Momentum losses of kaons and pions in the ^{9}Be and CH_2 target derived by subtracting the empty target data.

The solution of the previous equation with respect to $d\pi$, dK and S is the following,

$$\begin{aligned} d\pi &= \frac{CK - C\pi}{(R-1)} \\ dK &= \frac{R}{R-1} \times (CK - C\pi) \\ S &= \frac{R \times C\pi - CK}{R-1} \end{aligned}$$

Inserting the values from the empty data R=1.80, CK=10.91 and $C\pi$=6.19, we get

$$\begin{aligned} d\pi &= 5.90 \pm 0.30 \text{ MeV}/c \\ dK &= 10.62 \pm 0.59 \text{ MeV}/c \\ S &= 0.29 \pm 0.60 \text{ MeV}/c \end{aligned}$$

S is assumed to be due to calibration error in Kaon spectrometer dipole magnet. Non target related $d\pi$ and dK can be split up according to the fraction of material's mass before and after the target.

Materials between Q8 and the target are the drift chambers, HP monitor, ST, CP , air and vacuum window of Q8. Between the target and Q9, there are the drift chamber, air and vacuum window of Q9.

	Before target (g/cm^2)		After target (g/cm^2)
Vacuum window of Q8	0.04	Vacuum window of Q9	0.04
~ 1/2 m air	0.06	1/4 m air	0.03
6 Drift Chamber	0.14	5 Drift Chamber	0.12
ST, CP, HP monitor	2.56		
Total	2.80		0.19

ST = 1/4" scintillator, CP = 1/2" lucite, HP monitor = 1/16" scintillator, 3×1/32" vinyl tape around the scintillators are added with assumed density of 1 g/cm^3.

The fraction of the mass before and after the target is then:

$$\begin{aligned} \text{before: } 2.80/(2.80+0.19) &= 0.94 \\ \text{after: } 0.19/(2.80+0.19) &= 0.06 \end{aligned}$$

Then we get the non target-related kaon momentum loss as 10.62×0.94 = 9.98 MeV/c and pion momentum loss as 5.90×0.06 = 0.35 MeV/c.

Assuming the reaction was occurred at the center of the target, momentum losses in the target are divided into two for each kaon and pion. Also considering our target is rotated in 4 degree from kaon beam, kaon momentum loss is divided by cos(4^o).

The momentum losses of each incoming kaon and outgoing pion at 4 degree is determined as follows,

For incident K's

$$(\text{Be}^9)\ \text{K loss} = 0.5 \times 8.48/cos(4 \text{ deg.})[\text{Target}] + 0.94 \times 10.62[\text{Non target}] = 14.23 \pm 0.56 \text{ MeV}/c$$

$$(CH_2)\ \text{K loss} = 0.5 \times 8.37/cos(4 \text{ deg.})[\text{Target}] + 0.94 \times 10.62[\text{Non target}] = 14.18 \pm 0.56 \text{ MeV}/c$$

For emitted π's

$$(\text{Be}^9)\ \pi \text{ loss} = 0.5 \times 4.69[\text{Target}] + 0.06 \times 5.90[\text{Non target}] = 2.70 \pm 0.08 \text{ MeV}/c$$

$$(CH_2)\ \pi \text{ loss} = 0.5 \times 4.67[\text{Target}] + 0.06 \times 5.90[\text{Non target}] = 2.69 \pm 0.05 \text{ MeV}/c$$

The corrected pion spectrometer central momentum is 600.0 − S = 600.0 − 0.3 = 599.7 MeV/c and the momentum of kaons at the target position for ^{9}Be is about 600 − 14(Kaon momentum loss) = 586 MeV/c.

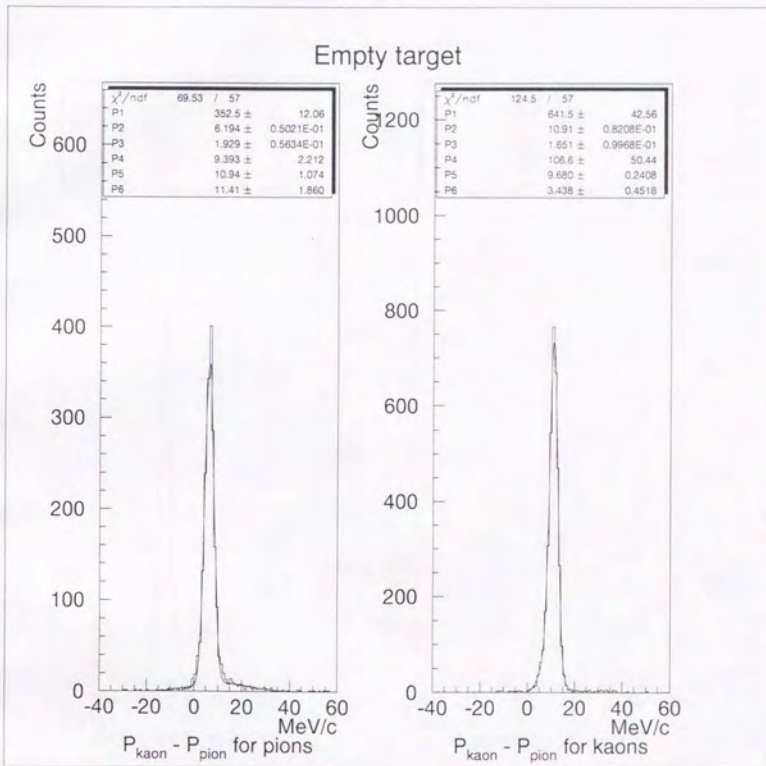

Figure D.1: Momentum loss distributions of pions(left) and kaons(right) in the target area for Empty target run. P_{kaon}(MeV/c) is momentum determined at the Kaon spectrometer. P_{pion}(MeV/c) is at the Pion spectrometer. Result of 2 Gaussians fit is shown in solid line

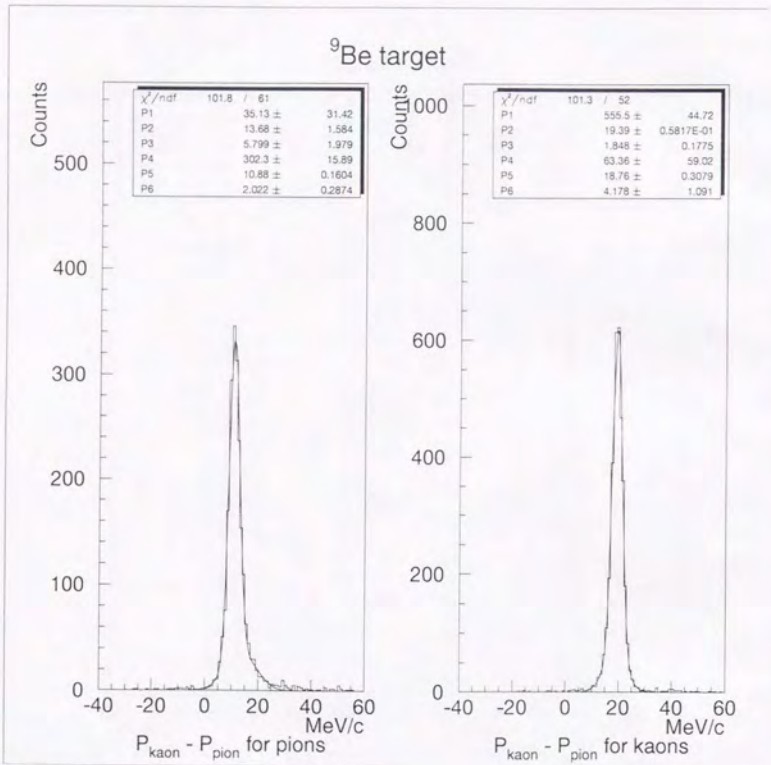

Figure D.2: Momentum loss distributions of pions(left) and kaons(right) in the target area with ^{9}Be target. P_{kaon}(MeV/c) is momentum determined at the Kaon spectrometer. P_{pion}(MeV/c) is at the Pion spectrometer. Result of 2 Gaussians fit is shown in solid line

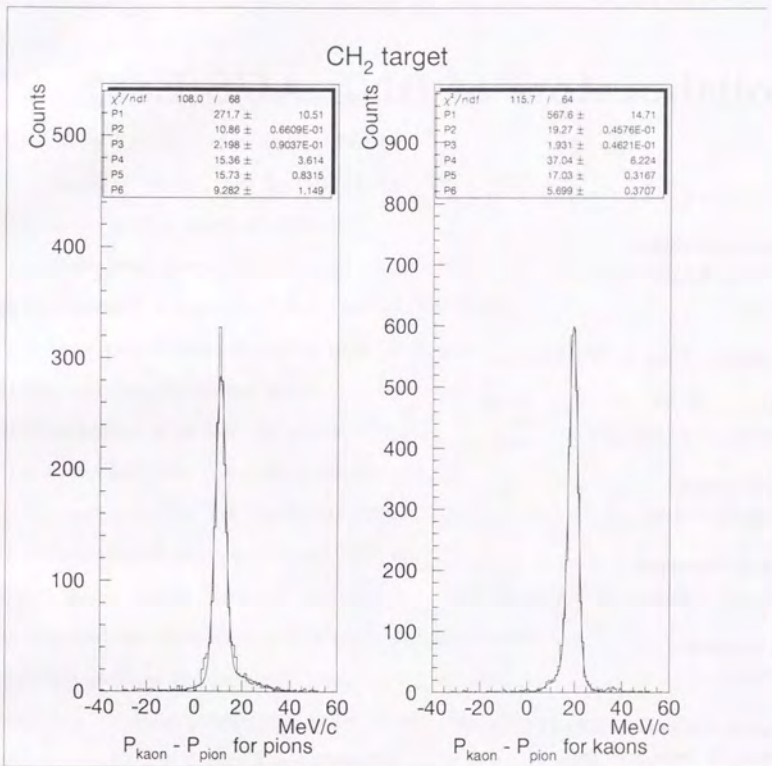

Figure D.3: Momentum loss distributions of pions(left) and kaons(right) in the target area with CH_2 target. P_{kaon}(MeV/c) is momentum determined at the Kaon spectrometer. P_{pion}(MeV/c) is at the Pion spectrometer. Result of 2 Gaussians fit is shown in solid line

Appendix E

Collaborators of BNL AGS E887

University of Tokyo
Y. Shimizu, R.S Hayano

INS
T. Fukuda, T. Nagae, K. Omata

BNL
R. Sawafta, S. Bart, R.E. Chrien

Ohio University
K. Hicks, R. Michael

Houston University
K. Gross, E.V. Hungerford, B. Mayes, I.J. Zhu

Yale University
M. Barakat

Hampton University(CEBAF)
K. Baker, W. Naing, L.G. Tang

Indiana University
W. Franklin, S. Wissink

Bibliography

[1] R. Bertini et al., *Phys. Lett.* **90B** (1980) 375.

[2] C.J. Batty et al., *Nucl. Phys.* **A 402** (1983) 349.

[3] A. Gal and C.B. Dover, *Phys. Rev. Lett.* **44** (1980) 379 and 962(E).

[4] D. Halderson, *Phys. Rev.* **C 40** (1989) 2173.

[5] O. Richter et al., *Few-Body Systems Suppl.* **5** (1992) 379.

[6] K. Ikeda and T. Yamada, *Int. J. Mod. Phys.* **A3** (1988) 2339.

[7] T. Yamada and K. Ikeda, *Nuovo Cim.* **102A** (1989) 481c.

[8] T. Harada, Private Communication.

[9] R. Bertini et al., *Phys. Lett.* **136B** (1984) 29.

[10] R. Bertini et al., *Phys. Lett.* **158B** (1985) 19.

[11] H. Piekarz et al., *Phys. Lett.* **110B** (1982) 428.

[12] T. Yamazaki et al., *Phys. Rev. Lett.* **54** (1985) 428.

[13] L.G. Tang et al., *Phys. Rev.* **C 38** (1988) 846.

[14] M. Iwasaki, *doctoral dissertation*, Univ. of Tokyo (1987), unpublished

[15] O. Morimatsu and K. Yazaki, *Nucl. Phys.* **A 483** (1988) 493.

[16] H. Outa, *doctoral dissertation*, Univ. of Tokyo (1995), unpublished.

[17] T. Harada et al., *Nucl. Phys.* **A 507** (1990) 715.

[18] R.S. Hayano et al., *Phys. Lett.* **231B** (1989) 355.

[19] Y. Shimizu, *master thesis*, Univ. of Tokyo (1992), unpublished.

[20] W. Naing, *doctoral dissertation*, Hampton University (1995), unpublished.

[21] J.R. Sanford and C.L. Wang, *BNL* **11279** (1967) and *BNL* **11479** (1967).

[22] A. Yamamoto, *KEK* **81-13** (1981).

[23] C. Dover, D.J. Millener and A. Gal, *Phys. Rep.* **184** (1989) 1.

[24] Developed by S. Kowalski of MIT (1981).

[25] GEANT, CERN program library Long Writeup **W5013**.

[26] G. Audi and A.H. Wapstra, *Nucl. Phys.* **A 565** (1993) 1 and 66.

[27] Review of Particle Properties, ed. M. Aguilar-Benitez et al., *Phys. Rev.* **D 50** (1994) 1173.

[28] R. Armenteros et al., *Nucl. Phys.* **B 21** (1970) 15.

[29] W. Brückner et al., *Proc. Kaon Factory Workshop* (Vancouver Canada), ed. M.K. Craddock (1979) 127.

[30] R.H. Dalitz and A. Gal, *Phys. Rev. Lett.* **36** (1976) 362.

[31] R.H. Dalitz and A. Gal, *Ann. of Phys.* **131** (1981) 314.

[32] C.J. Batty, *Phys. Lett.* **87B** (1979) 324.

[33] J.K. Lee et al., *Nucl. Phys.* **A 106** (1968) 357.

[34] V. Hepp et al., *Nucl. Phys.* **B 115** (1976) 82.

[35] B. Povh, *Ann. Rev. Nucl. Part. Sci.* **28** (1978) 1.

[36] C.J. Batty, *Nucl. Phys.* **A 372** (1981) 418.

[37] C.J. Batty, *Nucl. Phys.* **A 372** (1981) 433.

[38] A. Gal, G. Toker and Y. Alexander, *Ann. of Phys.* **137** (1981) 341.

[39] R. Bertini et al., *Nucl. Phys.* **A 368** (1981) 365.

[40] R. Bertini et al., *Nucl. Phys.* **A 360** (1981) 315.

[41] E.H. Auerbach et al., *Ann. of Phys.* **148** (1983) 381.

[42] A. Bouyssy, *Phys. Lett.* **99B** (1981) 373.

[43] T. Motaba et al., *Prog. of Theor. Phys. Suppl.* **81** (1985) 42.

[44] R.E. Chrien, E.V. Hungerford and T. Kishimoto, *Phys. Rev.* **C 35** (1987) 1589.

[45] A. Gal, *Proc. of 1986 INS Inter. Sympo. on Hypernuclear Physics* (Tokyo Japan) 31.

[46] M. Bernheim et al., *Nucl. Phys.* **A 375** (1982) 381.

[47] H. Tyren et al., *Nucl. Phys.* **79** (1966) 321.

[48] D. Bachelier et al., *Nucl. Phys.* **A 126** (1969) 61.

[49] I.S. Towner, *Nucl. Phys.* **A 126** (1969) 97.

[50] S.L. Belostotskii et al., *Sov. J. Nucl. Phys.* **41** (1985) 903.

[51] Yu.V. Dotsenko and V.E. Starodubskii, *Sov. J. Nucl. Phys.* **42** (1985) 66.

[52] F. Ajzenberg-Selove, *Nucl. Phys.* **A 490** (1988) 1.

[53] K. Nakamura et al., *Nucl. Phys.* **A 296** (1978) 431.

[54] S. Fullani and J. Mougey, Single Particle Properties of Nuclei through (e,e'p) reactions, *Advances in Nuclear Physics* **Vol.14** 1.

[55] Manual of TRANSPORT, *CERN* **73-16**.

[56] CERN program library CERNLIB short writeups, **C301**.

[57] CERN program library CERNLIB short writeups, **C300**.